Master of Science Thesis

Experimental Investigation of Boattail Radius Effects for Hammerhead Launcher Flows

Mathesh Babu Jaguva Krishnamoorthy

August 29, 2025

Faculty of Aerospace Engineering

Delft University of Technology

Experimental Investigation of Boattail Radius Effects for Hammerhead Launcher Flows

Master of Science Thesis

For obtaining the degree of Master of Science in Aerospace Engineering
at Delft University of Technology

Mathesh Babu Jaguva Krishnamoorthy

August 29, 2025

Faculty of Aerospace Engineering · Delft University of Technology

Delft University of Technology

DELFT UNIVERSITY OF TECHNOLOGY
DEPARTMENT OF AERODYNAMICS

The undersigned hereby certify that they have read and recommend to the Faculty of Aerospace Engineering for acceptance the thesis entitled **“Experimental Investigation of Boattail Radius Effects for Hammerhead Launcher Flows”** by **Mathesh Babu Jaguva Krishnamoorthy** in fulfillment of the requirements for the degree of **Master of Science**.

Dated: August 29, 2025

Chair:

Dr.ir. B.W. van Oudheusden

Supervisor:

Dr.ir. F.F.J. Schrijer

External Examiner:

Dr. S.J. Hulshoff

யாதும் ஊரே; யாவரும் கேளிர்!

“Every city is our city. Everyone is our kin.”

— Kaniyan Pungundranar —

6th century BCE

Acknowledgement

Before you lies the outcome of my nine-month research journey at the High-Speed Laboratory at TU Delft, titled *Experimental Investigation of Boattail Radius Effects for Hammerhead Launcher Flows.* This work would not have been possible without the support, guidance, and collaboration of many people.

First and foremost, I am deeply grateful to my supervisors, Ferry and Bas, for their continuous guidance throughout this journey. Their support and feedback—whether during weekly meetings or through unplanned run-ins—were invaluable, correcting me with patience and pointing me in the right direction whenever I lost track.

I would also like to sincerely thank the technicians at the HSL. In particular, I am indebted to Frits Donker Duyvis for his help with model fabrication, assistance in wind-tunnel operation, and setup during all experimental campaigns; Peter Duyndam for always being available to operate the tunnel; Gert-Jan Berends for help with the acquisition PC and hard-disk troubleshooting; and Dennis Bruikman for setting up the seeding system during the PIV campaign. It is unfortunate that the TST-27 could not be fixed within the timeframe of this thesis, despite their best efforts. My appreciation also goes to Kaushal Dave for his timely help with the PIV setup and for familiarising me with the Davis software. I am equally thankful to my labmates at the High-Speed Laboratory, whose discussions, advice, and camaraderie made the long hours in the lab both productive and enjoyable.

Beyond the lab, I am extremely grateful to my friends in both India and the Netherlands for helping me unwind during the hectic periods of the experimental campaigns, especially amid the uncertainty surrounding the TST-27. All the late-night Google Meet calls, casual conversations, and spontaneous small talk that grew into deeper discussions provided balance and encouragement when it was needed most.

Finally, and most importantly, I owe the deepest gratitude to my parents and my sister, who trusted a 21-year-old who had never left home to move to a new country. I am truly privileged to have their unwavering belief in me and my passions. I also extend heartfelt thanks to my extended family for their constant support.

நன்றி!

Mathesh Babu Jaguva Krishnamoorthy
Delft, August 2025

Abstract

This thesis presents the first systematic experimental investigation into the influence of boattail radius on the aerodynamics of Hammerhead Fairings (HHFs) in the transonic regime. The Coe and Nute Model 11, a well-documented academic HHF configuration, was selected as the test platform due to its ability to replicate key flow features of full-scale designs. The turbulent boundary layer thickness at separation was estimated using the reference temperature method and a flat-plate approximation, enabling selection of boattail radii spanning ratios from near unity to an order of magnitude greater. Two experimental campaigns were conducted: (i) high-speed schlieren imaging for all radius configurations, complemented by oil-flow visualisation at selected cases to document mean flow patterns, and (ii) particle image velocimetry (PIV) at selected configurations, optimised for high spatial resolution. Post-processing incorporated proper orthogonal decomposition (POD) and spectral POD (SPOD) to identify dominant flow structures and their spectral characteristics.

The results showed that introducing a boattail radius generates a third expansion region, often terminated by a third shock. Configurations were classified as exhibiting either weak radius effects (minimal third shock) or strong radius effects (prominent third shock and λ-shock structure). Strong radius cases promoted shock-induced separation, producing small separation bubbles at the λ-shock foot. Boattail curvature reduced separation length by 10–25% relative to the baseline; however, it also lifted the shear layer and increased reattachment-point oscillations.

Modal analysis revealed two dominant unsteady modes similar to backward-facing step flows: a *flapping mode*, controlling reattachment-point motion and strongly influenced by boattail geometry and shock structures, and an *undulation mode*, linked to periodic momentum exchange within the separation bubble. Spectral characteristics showed good agreement with BFS literature at lower Mach numbers but exhibited shifts at higher Mach numbers due to tunnel-induced frequency locking. SPOD confirmed that flapping behaviour in radius cases at $M = 0.8$ was closely associated with the third shock.

Overall, increasing boattail radius can beneficially shorten the separation region but introduces additional shock systems that intensify unsteady separation dynamics, with potential implications for launch vehicle stability and structural loading. The findings contribute novel, open-access experimental data on HHF boattail curvature effects and provide a foundation for future high-speed PIV measurements, computational studies, and load quantification to support design optimisation.

Contents

List of Figures

List of Tables

Nomenclature

Abbreviations

AoA	Angle of attack
ASLV	Augmented Satellite Launch Vehicle
BFS	Backward-facing step
CAE	Computational aeroelasticity
CFD	Computational fluid dynamics
CIRA	Centro Italiano Ricerche Aerospaziali
DDES	Delayed detached eddy simulation
DES	Detached eddy simulation
DMD	Dynamic mode decomposition
FFT	Fast Fourier Transform
FoV	Field of View
HHF	Hammerhead fairing
LDV	Laser Doppler velocimetry
LV	Launch vehicle
PIV	Particle image velocimetry
PLF	Payload fairing
POD	Proper orthogonal decomposition
PSLV	Polar Satellite Launch Vehicle
RANS	Reynolds-averaged Navier–Stokes
RMS	Root mean square
SPOD	Spectral proper orthogonal decomposition
SWBLI	Shock wave–boundary layer interaction
TBL	Turbulent boundary layer
uPSP	Unsteady pressure-sensitive paint
URANS	Unsteady Reynolds-averaged Navier–Stokes
VSSC	Vikram Sarabhai Space Centre

Symbols

α	Angle of attack [deg]
$\bar{a}$	Effective unblocked beam width
$\beta_j(f)$	SPOD temporal amplitude at frequency f
δ	Boundary layer thickness [mm]
Δf	Frequency resolution [Hz]
$\Delta I/I$	Relative schlieren intensity change
Δt	Pulse separation time [s]
δz	Depth of field [mm]
ϵ_y	Deflection angle in schlieren system
γ	Ratio of specific heats
μ_∞	Dynamic viscosity [Pa · s]
$\phi_j(\vec{x})$	Spatial POD mode j
$\psi_j(\vec{x}, f)$	SPOD spatial mode at frequency f

ρ_∞	Static density [kg/m^3]
σ_j	Singular value (energy content) of POD mode j
τ_p	Particle response time [s]
$\vec{U}_{slip}$	Particle slip velocity
a	Pinhole diameter [mm]
$a_j(t)$	Temporal coefficient of POD mode j
B_r	Blockage ratio
D	Fairing (payload) diameter [mm]
d	Vehicle body diameter [mm]
d_i	Image distance [mm]
d_o	Object distance [mm]
E_j	Energy of POD mode j
f	Focal length of schlieren mirror [mm]
f	Frequency [Hz]
$f_\#$	f-number (lens aperture ratio)
f_s	Sampling frequency [Hz]
f_{acq}	Acquisition frequency [Hz]
h	Boattail step height [mm]
h_i	Image size [mm]
h_o	Object size [mm]
H_T	Height of test section [mm]
k	Gladstone–Dale constant
M	Mach number
M	Magnification factor (optics)
M_∞	Freestream Mach number
M_{cr}	Critical Mach number
n	Refractive index
N_b	Number of samples per block
n_{perseg}	Samples per segment in Welch's method
$P(f)$	Welch-averaged PSD
p_0	Total (stagnation) pressure [Pa]
p_∞	Static pressure [Pa]
$PSD(f)$	Power spectral density
R	Specific gas constant for air (287.057 J/kg $\cdot$ K)
$r(k)$	Autocorrelation function
R/δ	Boattail radius to BL thickness ratio
Re	Reynolds number
Re_D	Reynolds number based on diameter D
T_0	Total (stagnation) temperature [K]
T_∞	Static temperature [K]
u'	Velocity fluctuation field
$u(\vec{x}, t)$	Velocity field as function of space and time
U_∞	Freestream velocity [m/s]
u_{avg}	Time-averaged velocity field
W_T	Width of test section [mm]
$X(f)$	Fourier transform of time signal
X_R	Mean reattachment location from boattail bottom corner [mm]
X_{SW1}	Streamwise position of first shock from nose [mm]

1

Introduction

In recent years, the global space industry has experienced an exponential rise in rocket launches, driven by the growing demand for satellite deployment, lunar and planetary exploration, and the increasing involvement of private sector ventures in space exploration. This surge has been fueled by advancements in miniaturised satellite technologies, such as cubesats and smallsats, which have significantly lowered the barriers to space access, making it more affordable and accessible. Furthermore, the advent of reusable rockets and cost-efficient launch vehicle innovations by commercial entities like SpaceX, Rocket Lab, and others has further accelerated the pace of space missions. As the frequency of launches continues to grow, the importance of sustainability within the space launch industry has become increasingly prominent. One approach to promoting sustainability in spaceflight involves the use of ”Hammerhead” or ”Bulbous” fairings. These fairings are characterised by a payload compartment with a diameter larger than the rest of the launch vehicle (LV). This design provides greater flexibility in accommodating payloads with higher volumes without a corresponding increase in payload weight. By eliminating the need for developing entirely new LVs to handle larger payload volumes, Hammerhead fairings contribute to cost efficiency and resource conservation in the launch industry.

A generic geometry of a Hammerhead Fairing (HHF) is illustrated in Figure 1.3. The design consists of three primary components: a nose cone, a cylindrical payload compartment with a larger diameter than the rest of the LV, and a tapered boattail section that integrates the payload compartment with the main body of the LV. The nose cone, positioned at the forefront, is designed to streamline the oncoming airflow around the LV, minimising turbulence and drag. Conical or ogive-shaped nose cones are commonly used due to their superior aerodynamic performance in reducing resistance during ascent. Following the nose cone is the payload compartment, which features a constant diameter and houses the main cargo. This section is specifically designed to protect the payload from aerodynamic forces and environmental conditions during the vehicle’s ascent through the atmosphere. The boattail, located at the rear of the payload compartment, provides a smooth transition between the larger diameter of the payload section and the narrower main body of the LV. Hammerhead Fairings have been widely adopted in contemporary launch vehicle designs, including the Falcon series by SpaceX (Figure 1.1(a)), the LVM Mk-III (Figure 1.1(b)), and the Vega family (Figure 1.2). Their innovative geometry allows for the accommodation of larger payload volumes while maintaining aerodynamic performance, making them a preferred choice for modern space missions.

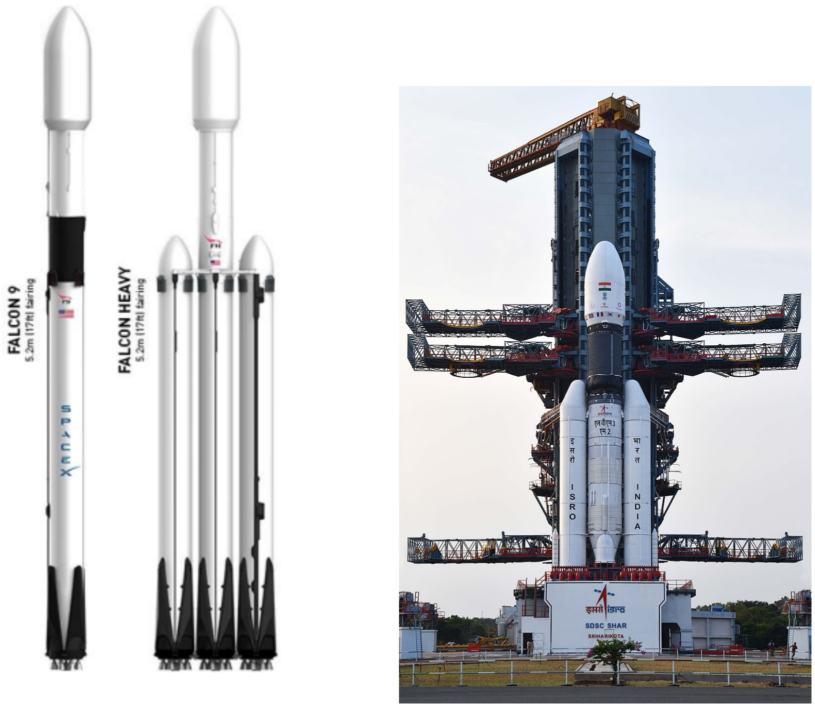

(a) Falcon series launchers - SpaceX

(b) LVM Mk-III - ISRO

Figure 1.1: Commercial launchers with HHF

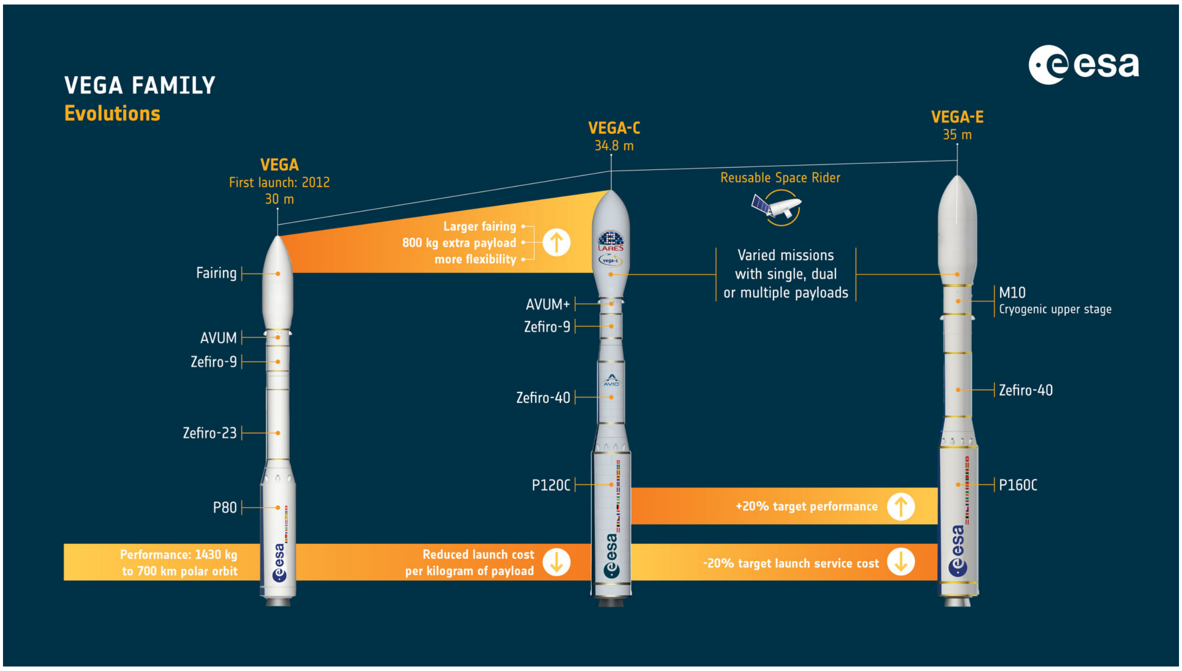

Figure 1.2: VEGA family of launchers - ESA

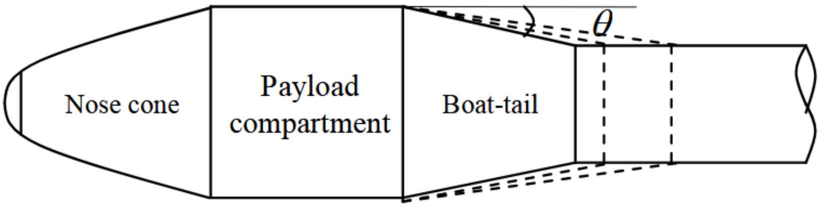

Figure 1.3: A generic HHF geometry [4]

Though HHF designs increase the LV's flexibility and aid in its sustainability, this design has inherent aerodynamic problems. This design exposes the vehicle to unsteady aerodynamic loads caused by flow separation at the boattail and Shock-Wave Boundary Layer Interactions (SWBLI) at transonic speeds. Such phenomena pose significant concerns for the stability of the LV, as managing unsteady aerodynamic effects is often more critical in their design than minimising drag. It has been under investigation since the 1960s, with most of the effort focused on developing a buffet-free design guideline for the HHF.

1.1 Scope of the Thesis

This thesis investigates the aerodynamic effects of varying the boattail geometry in HHF configurations, with a particular emphasis on the influence of boattail radius. The work builds upon the study by Romero [49], who examined the impact of geometric variations in nose and boattail angles under transonic flow conditions. While Romero's findings provided valuable insights into the role of boattail angle, the effect of boattail curvature has remained largely unexplored. A review of the literature conducted at the outset of this research revealed that, to the best of the author's knowledge, no open-access study has systematically evaluated the aerodynamic consequences of modifying boattail radius for HHF configurations. Furthermore, there is a notable absence of detailed characterisation of the unsteady flow field around HHF geometries, particularly in the context of shock–shear layer interactions and wake dynamics.

To address these gaps, this work combines multiple experimental techniques—schlieren imaging, surface oil-flow visualisation, and particle image velocimetry (PIV)—to capture both the steady and unsteady features of the flow. Schlieren imaging enables the visualisation of shock wave patterns and their temporal evolution, oil-flow visualisation provides surface streamline patterns and separation topology, and PIV offers quantitative velocity field data for assessing shear layer development and wake structures. By applying these complementary methods to a range of boattail radii, the study aims to establish a comprehensive understanding of how curvature influences flow topology, shock interactions, and wake dynamics.

The motivation for focusing on boattail radius stems from its prevalence in real-world LV designs. Many contemporary LVs incorporating an HHF adopt a rounded boattail configuration

(Figures 1.1 and 1.2). Despite its widespread use, this design choice is significantly underrepresented in open-access aerodynamic databases, which tend to focus on sharp transitions in boattail geometries. Consequently, this research is both timely and relevant, offering novel experimental data that can inform the design process for future LV configurations. The findings are expected to benefit both industry and academia by providing new insights into the influence of boattail curvature on unsteady flow behaviour.

1.2 Report outline

This report is organised into five chapters, including the present one. Following the Introduction, Chapter 2 summarises the key findings from the literature review conducted at the outset of this research, establishing the current state of knowledge and identifying research gaps. Chapter 3 describes the experimental methodology in detail, including the motivation for the model design, the variations investigated, the experimental setup, measurement techniques, test matrix, and post-processing procedures. Chapter 4 presents and analyses the experimental results, providing a comprehensive discussion of the observed flow phenomena and their implications. Finally, Chapter 5 concludes the report by summarising the principal outcomes of the study and offering recommendations for future research in this field.

2

Literature Study

This chapter presents the findings of the literature review conducted at the outset of this research. It begins with an overview of the general flow features associated with HHF, followed by an examination of the influence of geometric variations and flow conditions. The discussion then extends to broader aerodynamic phenomena relevant to the present study. Finally, the identified research gaps are outlined, from which the research questions are formulated.

2.1 Flow pattern over Hammerhead Fairings

High-speed aerodynamic flows are classified using a dimensionless quantity known as the *Mach number* (M). It is defined as the ratio of the local flow velocity to the speed of sound in the given medium. The classification of flow regimes based on Mach number is shown in Equation 2.1 [2]. Among these regimes, the transonic flow is regarded as the most complex due to the simultaneous presence of both supersonic and subsonic regions in the flow field, particularly when the flow interacts with a solid object. The distinction of transonic flow from subsonic and supersonic flow is due to the occurrence of supersonic pockets when $M < 1$, and subsonic pockets when $M > 1$, in the freestream as shown in Figure 2.1. For Mach numbers slightly below unity, flow acceleration over any object can make the flow supersonic, which is typically ended by a weak shock wave to recover to freestream conditions. For Mach numbers slightly above unity, a bow shock is formed in front of the object, with a subsonic region behind it, which eventually accelerates to supersonic conditions over the object. The flow is terminated by a tailing edge shock[2].

$$
\begin{aligned}
&M < 0.8 && \text{Subsonic,} \\
&0.8 \leq M \leq 1.2 && \text{Transonic,} \\
&1.2 \leq M \leq 5 && \text{Supersonic,} \\
&M > 5 && \text{Hypersonic.}
\end{aligned}
\tag{2.1}
$$

2.1.1 Transonic flow

An LV transitions through subsonic, transonic, and supersonic flow regimes during its ascent through the atmosphere, making aerodynamics a critical consideration in the design process. It does reach the hypersonic flow regime, but the dynamic pressure at that altitude is minimal; hence, aerodynamics has little impact.

The steady and unsteady aerodynamic loads encountered during flight have a significant influence on vehicle control, stability, and structural integrity. The transonic regime is particularly challenging as it generates the highest levels of unsteadiness. This is further compounded by the fact that transonic flow coincides with the phase of maximum dynamic pressure on the vehicle, as illustrated in Figure 2.2. Unsteady aerodynamic loads in this regime can arise from a variety of factors, including turbulence in the flow, wakes from surface protrusions, shock wave movements, shock-boundary layer interactions, geometric flow separation and reattachment, as well as wake flow at the vehicle's base[5]. Hammerhead Fairings (HHF) are particularly susceptible to many of these unsteady aerodynamic phenomena during transonic flight. Therefore, studying the behaviour of HHF in this regime is critical for improving their aerodynamic performance and overall design efficiency.

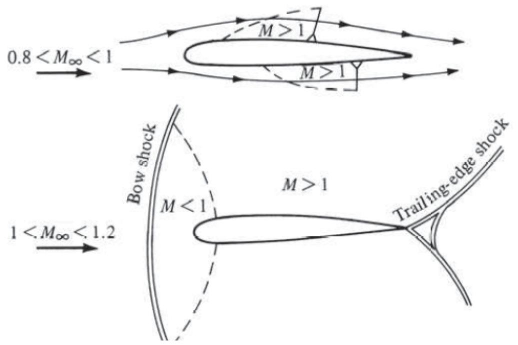

Figure 2.1: Transonic flow over slender bodies [2]

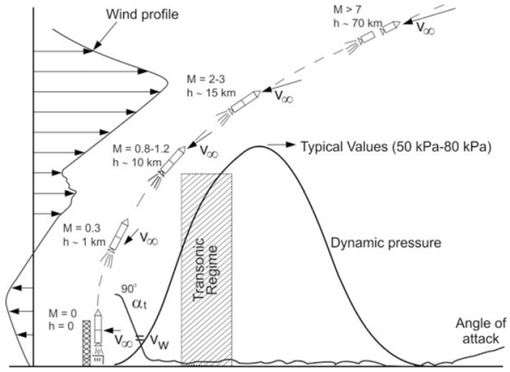

Figure 2.2: Flight profile of a launch vehicle [5]

Mehta [39] presented a more detailed schematic, shown in Figure 2.3, illustrating the typical flow phenomena occurring over an HHF at transonic speeds. At the nose cone tip, a stagnation point is formed due to the impingement of the freestream flow. Moving downstream, expansion fans develop over the cone-cylinder junction, accelerating the flow to supersonic speeds. These expansion waves lead to the formation of a supersonic pocket, which extends along the cylindrical section until it is terminated by a shock wave. The terminal shock interacts with the boundary layer, leading to SWBLI. This interaction thickens the boundary layer, reducing its momentum and ultimately causing flow separation at the boattail corner. The separated flow forms a recirculation region, where low-energy fluid is trapped, leading to increased aerodynamic drag and unsteady pressure fluctuations. This separated shear layer continues downstream until it reattaches at the reattachment point, forming a closed wake structure. The length of this separated region is influenced by the geometry of the boattail and the flow conditions, as will be discussed in section 2.2.2

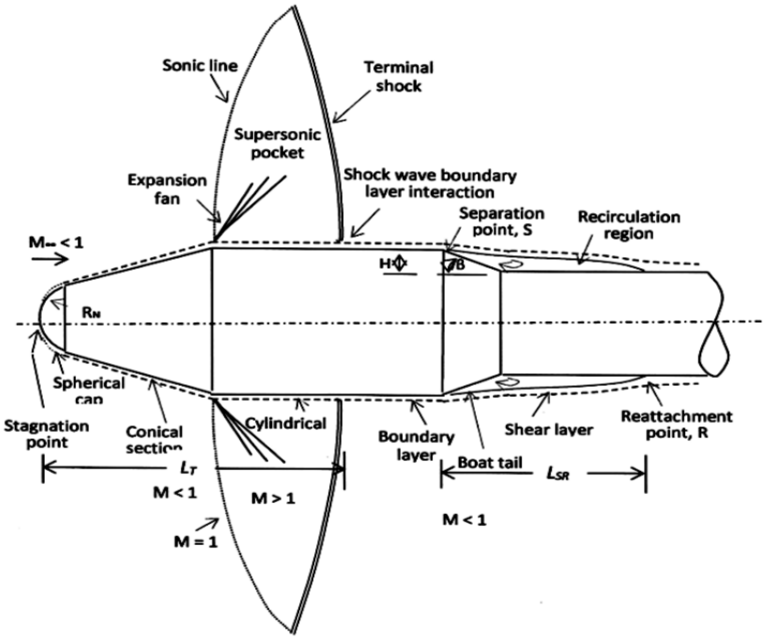

Figure 2.3: Schematic of transonic flow field over HHF [39]

Around a freestream Mach number of 0.8, Suresh and Sivan [5] found that sonic conditions are first reached over the HHF; thus, approximately 0.8 is the critical Mach number, M_{cr}. As the free stream Mach number increases, local supersonic pockets are formed due to the expansion of the flow at the cone-cylinder junction. This supersonic pocket is terminated by a weak shock wave. Due to SWBLI, the already developed turbulent boundary layer(TBL) can thicken, which can lead to shear layer separation at the foot of the shock wave, as shown in Figure 2.4b. When the Mach number reaches 1.2, there will be clear expansion waves at the cone-cylinder junction and boattail edge, and a bow shock in front of the vehicle. At this free stream velocity, the flow over HHF is fully supersonic, except for the stagnation zone at the nose of the HHF(Figure 2.4d).

2.1.2 Flow separation in HHF

Flow separation on a wall typically occurs due to an adverse pressure gradient, which refers to an increase in pressure along the flow direction. Under such conditions, fluid particles in the relatively slow-moving boundary layer must work against the rising pressure, causing a further reduction in velocity. If the adverse pressure gradient is strong enough, these particles can come to a complete stop, leading to boundary layer separation [2]. While this mechanism is representative of separation over simple geometries such as flat plates, in more complex configurations like HHF, the dominant cause of separation is the abrupt geometric transition at the boattail (Figure 2.6.

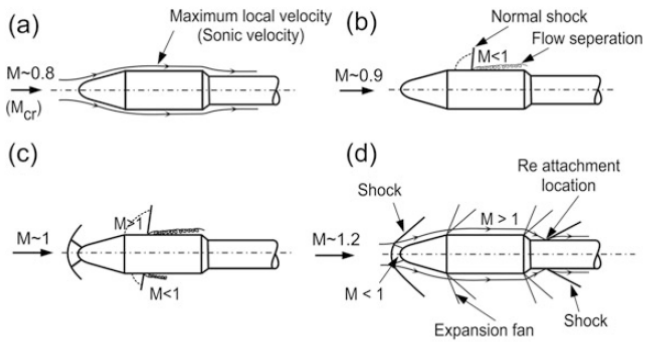

Figure 2.4: Transonic flow over HHF [5]

Flow separation in general can result from various factors, including geometric discontinuities, SWBLI, and the wake formed behind a body [5]. In the case of HHF, separation primarily arises from the boattail transition combined with shock–boundary layer effects. This separated region downstream of HHF induces higher bending moments in the transonic regime, as observed experimentally by Chou [12] and illustrated in Figure 2.5. A more detailed discussion of the separation characteristics at the boattail under different Mach number conditions is provided in Section 2.2.2.

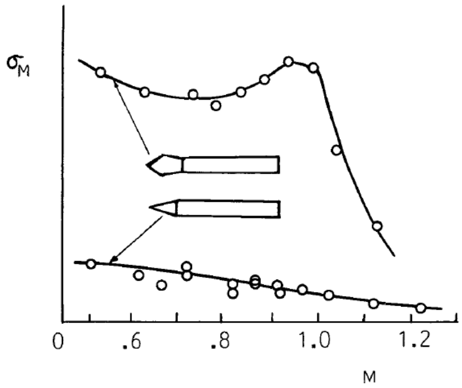

Figure 2.5: Effect of nose shape on buffet response.

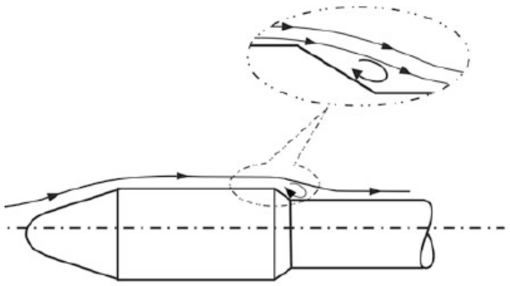

Figure 2.6: Flow separation in HHF [5].

2.1.3 Unsteady loads

During transonic flight, shocks formed around the vehicle generate significant differential pressure, leading to increased structural loading. The shock positions vary over time, resulting in pressure fluctuations across the vehicle's surface. Additionally, SWBLI can induce flow separation, contributing to unsteady aerodynamic loads. Sources of unsteady loads on an HHF are shown in Figure **??**. These unsteady loads encompass pressure fluctuations over a wide range of frequencies, from low to very high. Low-frequency fluctuations, commonly referred to as buffet loads, can excite the lateral flexible modes of the vehicle, potentially affecting its stability. On the other hand, high-frequency fluctuations, known as aeroacoustic loads, can result in severe acoustic interference [5].

The nature of transonic buffet loads varies depending on the aerodynamic configuration of the vehicle. Suresh and Sivan [5] classified buffet phenomena into three distinct types: transonic buffet, wake buffet, and shock-boundary layer separation buffet. Transonic buffet arises from unsteady shock movements, wake buffet is caused by the unsteady wakes generated by functional protrusions on the vehicle, and shock-boundary layer separation buffet results from flow separation and subsequent reattachment. Each of these buffet types contributes to time-varying pressure fluctuations, imposing unsteady aerodynamic loads on the vehicle. These loads pose a significant risk to structural stability, potentially compromising performance during flight. Notably, buffeting is not exclusive to HHF configurations; even simple cone-cylinder sounding rockets, such as the Brazilian VS-40, experience similar unsteady aerodynamic phenomena [3].

Failure to quantify these unsteady loads can have catastrophic consequences, as demonstrated by past launch vehicle failures. Although no direct failure data are available for HHF, historical examples such as the Pegasus XL and Delta II Heavy highlight the risks of inadequate aerodynamic characterisation [26]. In the case of Pegasus XL, engineers had underpredicted the effectiveness of its fins, leading the control system to overcorrect and ultimately inducing a divergent roll oscillation. Similarly, the Delta II Heavy, despite undergoing rigorous industry-standard testing, failed to adequately characterize the unsteady aerodynamic loads at the base of its solid rocket boosters [26]. However, unlike Pegasus XL, the Delta II Heavy was not lost during flight, as the control system successfully managed the unsteady loads, allowing the mission to be completed.

Given the risks posed by transonic buffet loads, accurately defining them is critical to ensuring the structural stability of an LV. The classical approach involves conducting experimental campaigns on scaled-down rigid models in wind tunnels, acquiring unsteady data using pressure transducers, and utilizing this data to derive buffet forcing functions. These functions serve as inputs for structural analysis programs, enabling engineers to assess and mitigate potential structural instabilities in launch vehicles [44].

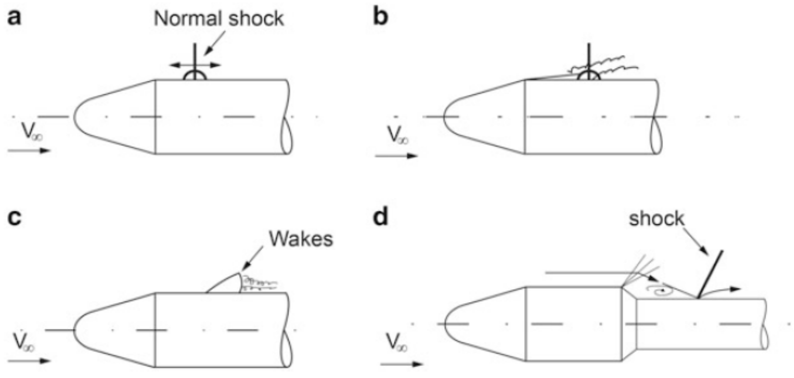

Figure 2.7: Causes of unsteady loads [5]

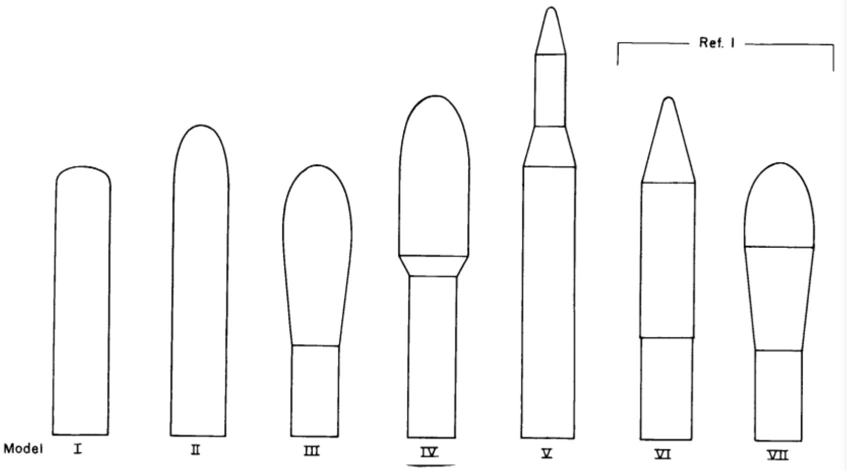

Figure 2.8: PLF shapes investigated by Coe [14, 15]

2.1.4 Benchmark configuration

A series of experimental studies conducted by the NASA Ames Research Center in the 1960s investigated various PLF shapes to characterise their transonic performance [13, 14, 15]. This campaign began with tests on the PLF shapes of the Centaur and Able-V vehicles, shown labelled VI and VII in Figure 2.8, which feature straight and bulbous PLFs, respectively. The studies revealed that the maximum pressure fluctuations at any Mach number and angle of attack occurred in the region of the shockwave. Additionally, it was observed that the fluctuations caused by shockwave oscillations were greater in the Able-V model than in the Centaur model. Large regions of unsteady pressure were also identified on the converging afterbody of the Able-V model, particularly at nonzero angles of attack, indicating flow separation behind the shockwave [14].

In a subsequent study, Coe [15] tested five additional PLF shapes in the transonic regime to investigate the influence of nose shape on pressure fluctuations. These shapes are shown in Figure 2.8, labelled I to V. The results showed that the sharpness of the area reduction in converging sections affects the Mach number range over which pressure fluctuations occur. It was also noted that the boattailing in Model labelled as IV results in a separation region with pressure fluctuations over extensive areas on the vehicle. However, due to the significant differences in the models used, direct comparisons between them could not be made.

Having observed interesting flow structures associated with boattailing, Coe and Nute [13] investigated three HHF geometries, shown in Figure 2.9, to examine pressure fluctuations in the transonic regime. Among the configurations, Model 11—which features the largest fairing-to-vehicle diameter ratio—exhibited the most significant pressure fluctuations within the separation region. Owing to this behaviour, Model 11 has attracted substantial attention in recent studies, serving as a reference case for understanding the unsteady aerodynamic characteristics of HHF. This configuration, now commonly referred to as the Coe and Nute Model 11, has been the subject of multiple investigations aimed at characterising the dominant flow structures and associated pressure dynamics.

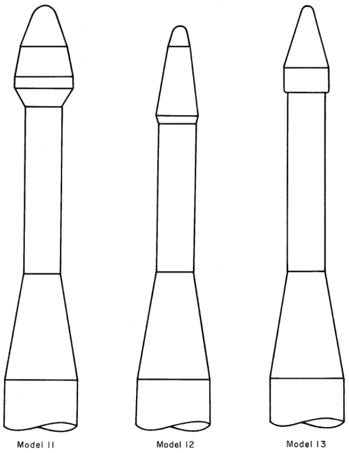

Figure 2.9: HHF investigated by Coe and Nute [13]

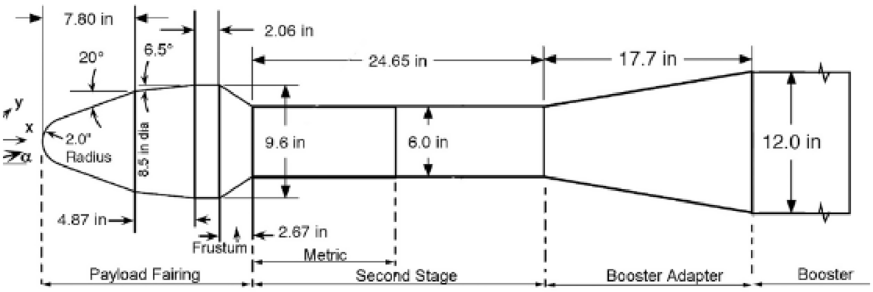

Figure 2.10: Dimensions of the Model 11 used by Panda et al. [43]

The specific geometry of Model 11, as employed by Panda et al. [42, 43], is shown in Figure 2.10. The fairing portion is referred to as the payload fairing (PLF). The cylindrical section that follows the PLF is designated as the second stage, while the larger-diameter cylinder at the end is referred to as the booster, which is connected to the second stage via an adapter. A representative distribution of root mean square (RMS) pressure fluctuations, as documented by Coe and Nute, is presented in Figure 2.11. In this distribution, fluctuations caused by shock waves appear as localised peaks, whereas those associated with flow separation span a broader region, with maxima typically occurring near the reattachment location.

Figure 2.12 illustrates the flow structures at different Mach numbers as reported by Panda et al. [42], where normal shocks are observed at $M = 0.8$, and only oblique shocks at $M = 1.2$. Two shocks, each at the junction of geometric changes, were later verified by Romero [49] in her study at $M = 0.8$. From the RMS pressure fluctuations shown in Figure 2.13, Panda et al. [42] concluded that significant pressure fluctuations on the fairing occurred only in the presence of transonic shocks, with increased unsteadiness in the separated region under these conditions. Cross-correlating pressure transducer data revealed that fluctuations propagated downstream along the second stage and upstream along the PLF, indicating that there might be a coupling of the separation region and shockwave oscillations. However, this correlation

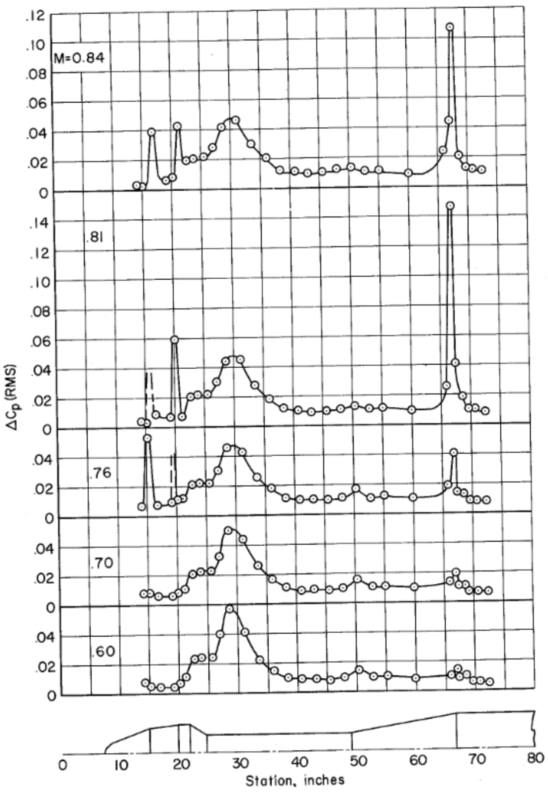

Figure 2.11: RMS pressure fluctuations on the Model 11 at 0° angle or attack [13]

diminished at supersonic speeds, indicating that the fluctuations were predominantly confined to the transonic range and possibly acoustic in nature. Another key observation was that at transonic speeds, the shear layer was lifted due to SWBLI, potentially increasing both the separation length and overall unsteadiness. This study presented RMS fluctuations inclusive of higher frequencies than Coe and Nute [13], who measured only in the range of 5 Hz to 1 kHz, resulting in a slight increase in the values.

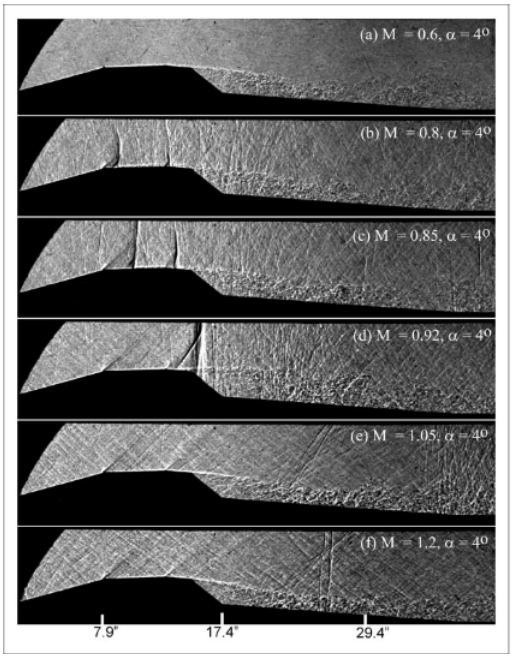

Figure 2.12: Shadowgraph images from Panda et al. [42]

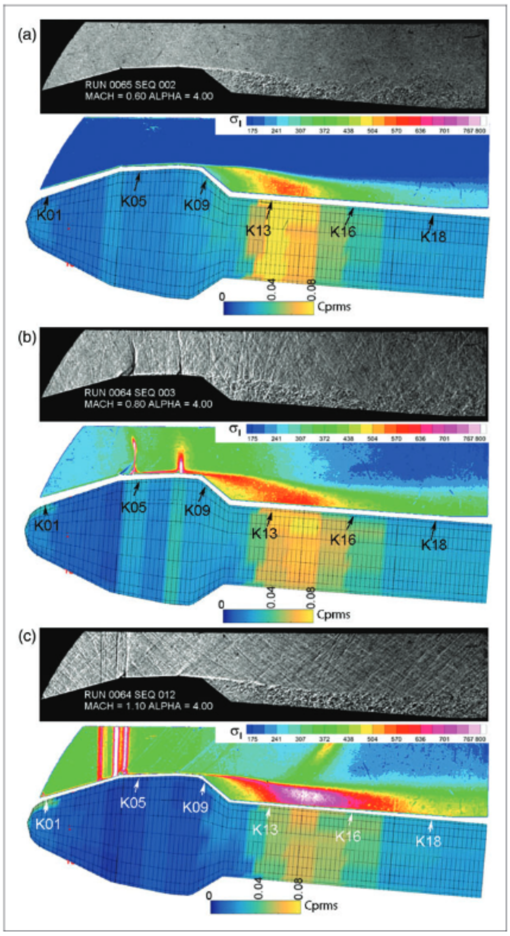

Figure 2.13: RMS pressure fluctuations on the surface and flow around HHF[42]

In recent years, Model 11 has gained attention in numerical studies as well. Rho et al. [48] applied a CFD-CAE (Computational Fluid Dynamics - Computational Aeroelasticity) coupled method and compared their results with the experimental data of Coe and Nute [13]. While both URANS and DDES successfully predicted the mean C_p, the DDES model demonstrated superior accuracy in capturing C_{prms}. Murman et al. [40] conducted Detached DES simulations using NASA's OVERFLOW solver with a hybrid RANS model. The identified POD and DMD modes were found to closely correspond with those obtained from uPSP measurements. However, only the mode shapes were provided without much description about them. These shapes are shown in Figure 2.14. The maximum resolved frequency component was 1570 Hz, which may also be constrained by the uPSP acquisition frequency of 5 kHz. Jamshed et al.

[30] and Liu et al. [37] also carried out a DDES simulation on Model 11 and found good agreement with the experiments, with the latter doing it for the whole model with the first stage booster.

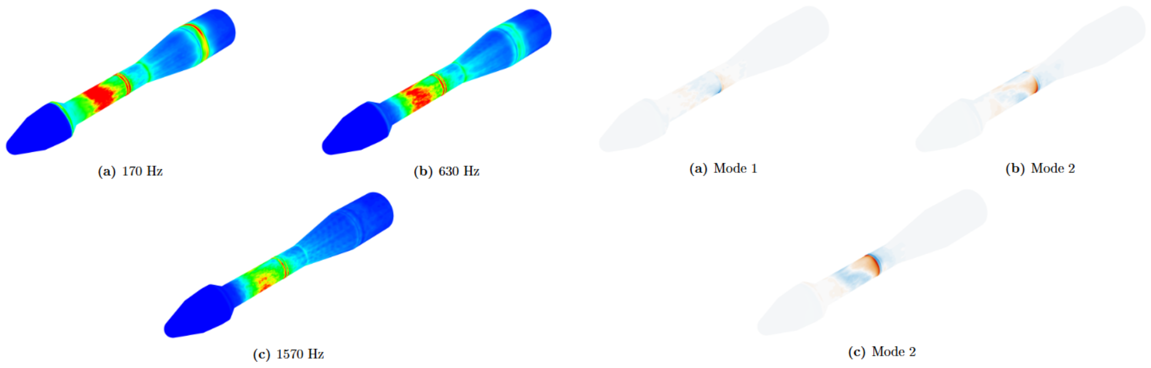

(a) DMD modes (b) POD modes

Figure 2.14: Mode shapes obtained by Murman et al [40] from CFD simulations

Industrial configurations similar to Model 11, such as the VEGA launcher, have also been subjected to numerical studies as part of their development. CIRA conducted extensive simulations using its Zonal Euler Navier-Stokes (ZEN) simulation system and validated the data against experimental results for the VEGA launcher [9]. Despite utilising only the RANS turbulence model, the study achieved a strong correlation between simulations and experiments across a wide range of Mach and Reynolds numbers.

2.2 Geometric effects

2.2.1 Payload Fairing Design

The shape of the PLF is typically either conical or ogive, as illustrated in Figure 2.15. The ogive shape offers several advantages, including a larger payload volume for a given base diameter and improved aerodynamic performance due to reduced drag and minimised unsteady loads. However, it is challenging to manufacture because it requires high precision, and any deviation from the intended shape can result in significant unsteady loads. In contrast, the conical PLF, while aerodynamically less efficient than the ogive shape, provides greater flexibility in manufacturing. The conical design is easier to produce and accommodates larger tolerance levels without a sudden decline in performance, making it a more practical choice in scenarios where manufacturing complexity is a concern [5].

The main design parameters for a conical HHF, as defined by Suresh and Sivan [5], are illustrated in Figure 2.16:

- Vehicle diameter (d) decided by the propulsion unit
- Payload fairing diameter (D) decided by the satellite requirements
- Nose bluntness (R)
- Nose cone angle (δ_1)
- Nose cone length (l_1)
- Cylindrical length (l_2)
- Boattail angle (δ_2)
- Boattail length (l_3) – fixed once δ_2, D, d are known

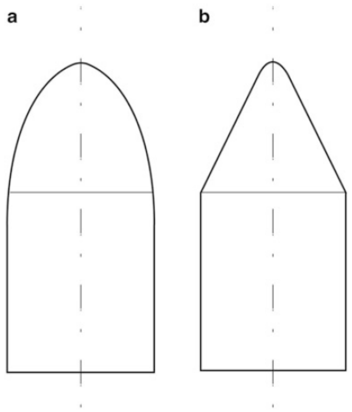

Figure 2.15: (a)Ogive and (b)Conical PLF shapes [5]

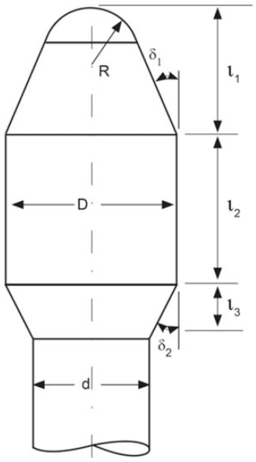

Figure 2.16: HHF design parameters by Suresh and Sivan[5]

Buffet-free design guidelines

Due to the growing interest in the use of HHF in launch vehicles in the 1960s, NASA developed a handbook that provides guidelines for a buffet-free design [41]. These guidelines, summarised in Table 2.1, are based on the results of a series of experimental campaigns. However, strict adherence to these guidelines is not always feasible due to payload constraints. Consequently, a stable buffet condition is also provided, under which buffeting loads must be analysed and accounted for in the structural design of the vehicle. The Model 11, with a D/d of 1.6, falls in the upper extreme of stable buffet design space.

2.2.2 Boattail aerodynamics

In many launch vehicles, the PLF, which has a larger diameter than the rest of the vehicle, is connected via a boattail. Due to the sharp reduction in cross-sectional area, this region

Table 2.1: Guidelines for geometrical parameters of PLF and buffet criteria [41]

Geometrical parameters of launch vehicle forebody (payload fairing)	**Criteria**		
	Buffet free	**Buffet prone & stable** (stable buffet)	**Unstable buffet**
l_1/D	≥ 0.8		
l_2/D	≥ 1.5		
δ_1	$\leq 15°$		
D/d	< 1.1	< 1.6	> 1.6
δ_2	Not critical		

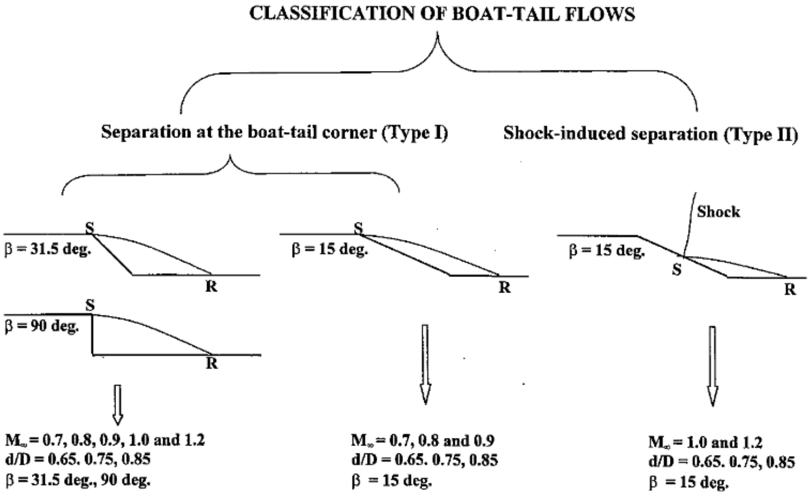

Figure 2.17: Types of separation at boattail [33]

plays a dominant role in the unsteady aerodynamic characteristics of vehicles employing such configurations. Initial computational studies conducted by the Vikram Sarabhai Space Centre (VSSC) in 1988 indicated that for boattail geometries based on the PSLV and ASLV, flow remained separated up to a Mach number of 2.47. A dual-shock system was observed and subsequently validated through experimental studies. However, these investigations were primarily axisymmetric due to computational limitations at the time [45].

Kumar et al. categorised the separation at the boattail into two types: **separation at the boattail corner** and **shock-induced separation**. The former occurs in most cases with relatively high boattail angles and has also been observed on the Coe and Nute Model 11, which features a boattail angle of 34° [49, 42, 43].

Reducing the boattail angle allows the flow to stay attached to the surface of the boattail and enables it to expand into another supersonic pocket, which is terminated by a shock and may lead to separation, depending on the angle and flow conditions. This third shockwave oscillates and momentarily merges with the second shockwave as well[49]. Instantaneous schlieren images and the standard deviation of pixel intensities depicting shockwave oscillations for different boattail angles are shown in Figure 2.19 and Figure 2.20. The baseline Model 11 shows two shocks, whereas the other two at 15° and 5° show three shockwaves. At 15°, the flow accelerates to sonic conditions past the boattail corner and is terminated by a third shockwave, which is strong enough to cause shear layer separation at its foot. The third shock is also observed for 5° boattail angle, but the flow remains attached in this case. Reducing the boattail angle has also been shown to mitigate the pressure fluctuations in the low-frequency range in the separation bubble [35]. Figure 2.18 illustrates this effect of reducing the boattail angle on the circumferentially averaged distribution of pressure fluctuations, where a drop in fluctuations is noted near the reattachment location.

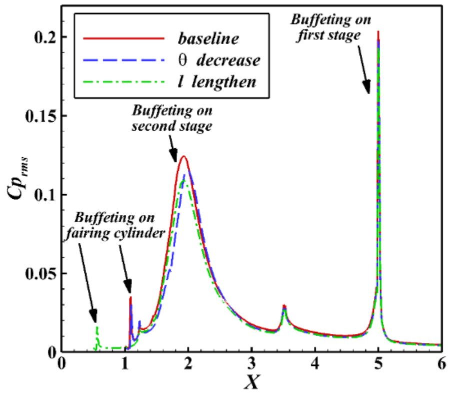

Figure 2.18: Circumferential average of pressure fluctuations on the surface of three variations tested by Li et al.[35]

Although studied on different models, Kumar et al. [33] and D'Aguanno et al. [19] both observed that the separation length increased with higher boattail angles. For boattails with larger angles, the flow was not sufficiently deflected downward before separation, causing the shear layer to follow a longer path before reattaching to the surface. For Model 11, Panda et al. [42], Romero [49], and Costa [17] consistently reported separation occurring at the boattail corner. Among the cases tested by Kumar et al. [33], a boattail angle of 31.5° exhibited flow separation characteristics similar to those observed in a backward facing step (BFS). Consequently, further discussion on BFS-related literature is presented in Section 2.6.

Costa [17] investigated the flow around the HHF of the European VEGA-E launcher. This model featured a 30° boattail angle, yet shockwave-induced separation was observed. This was attributed to the smooth rounding of the boattail in VEGA-E, which also exhibited weaker shockwaves, smaller separation regions, and fewer oscillations compared to the Coe and Nute Model 11. D'Aguanno et al. [19] tested different boattail angles on this model and found that the flow remained attached for a 15° boattail angle, while at a 55° boattail angle, no second shock was observed, indicating separation at the boattail edge. The fluctuations in the separated region were found to increase with both an increase in boattail angle [19] and an increase in d/D radio [33].

An optimisation study by Sunil et al. [59] investigated the boattail geometry of a generic launch vehicle with the objective of minimising drag coefficient, boattail length, and separation length. Using RANS simulations with a k–ω turbulence model, the authors identified the ramp-stepped boattail as the optimal configuration (see Figure 2.21). In addition to satisfying all optimisation objectives, this configuration was also found to reduce the turbulent kinetic

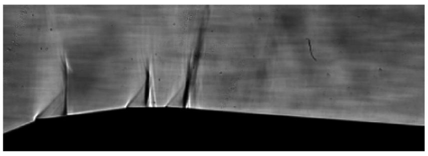

(a) Boat-tail of 5 degrees (BC5 run 7 at the Schlieren test matrix in the appendices)

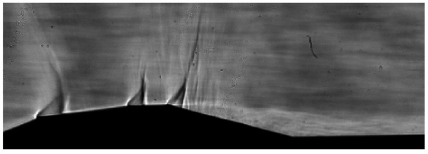

(b) Boat-tail of 15 degrees (BC15 run 9 at the Schlieren test matrix in the appendices)

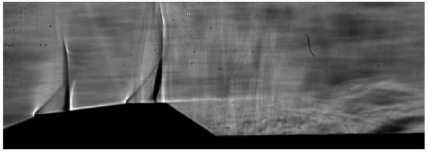

(c) Boat-tail of 34 degrees (BC34 run 5 at the Schlieren test matrix in the appendices)

Figure 2.19: Instantaneous images of Schlieren visualisation by Romero [49] for 5°, 15°, 34° boattail angle at M = 0.8

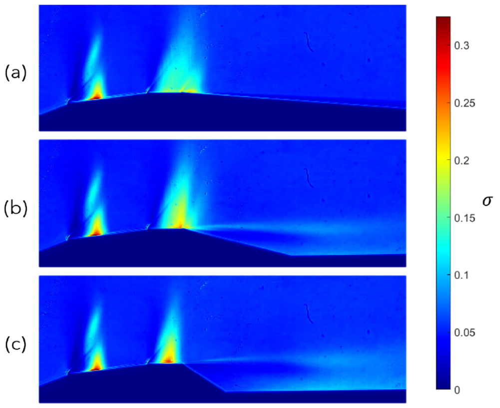

Figure 2.20: Pixel intensity standard deviation of schlieren images for 5°, 15°, 34° boattail angle at M = 0.8[49]

energy in the wake.

2.2.3 Fairing Length

Cole and Henning [16] investigated the buffet response of an aeroelastically scaled Atlas-Centaur I launch vehicle, which has a length-to-diameter (L/D) ratio of 1.0, at the NASA Langley Transonic Dynamics Tunnel. A parametric study was conducted to examine the effect of model configuration on buffet response, using L/D ratios of 0.3, 0.6, 0.8, 1.0, and 1.2, as shown in Figure 2.22. By analysing the buffet response coefficient, the study provides evidence that lower L/D configurations tend to induce higher amplitudes in buffet responses. While this trend was not clearly observed for the first bending moment, the L/D = 0.3 configuration exhibited significantly higher values for the second bending moment at transonic speeds. Another key finding from this study is that the dynamic response of the model was more sensitive to variations in Mach number than to changes in angle of attack, shown in Figure 2.23. This suggests that transonic buffet behaviour is primarily influenced by compressibility effects rather than by changes in flow incidence.

While conducting second-moment closure Detached Eddy Simulations (DES), Liu et al. [35] found that increasing the fairing length resulted in a reduction of pressure fluctuations across the entire frequency range. This effect was attributed to a decrease in shear strength within the boundary layer for higher L/D configurations, which in turn reduced the fluctuation energy in the separation region. It was also noted that the perturbation backscatter was lower in higher fairing length cases, which could reduce the coupling between the separated region and shock wave oscillation.

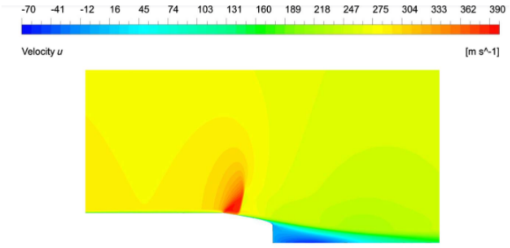

a) Shorter boat tail ($(x_4 - x_0)/y_0 = 0.5$)

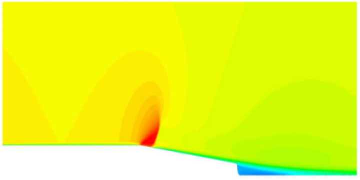

b) Moderate boat tail ($(x_4 - x_0)/y_0 = 1.0$)

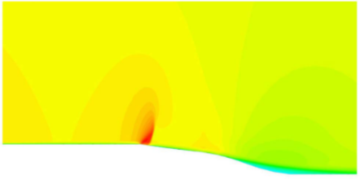

c) Longer boat tail ($(x_4 - x_0)/y_0 = 1.5$)

Figure 2.21: Ramp-stepped boattail [59]

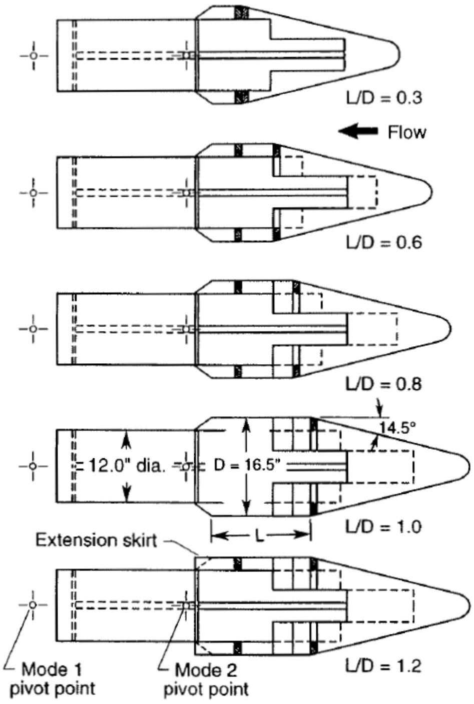

Figure 2.22: L/D variations of Atlas – Centaur I vehicle [16]

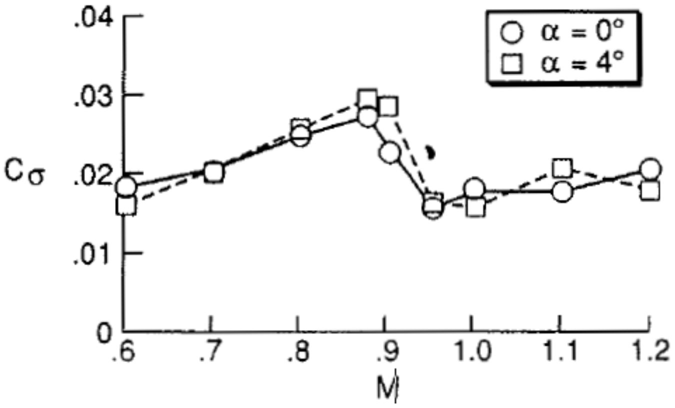

Figure 2.23: Effect of Mach number and angle of attack on bending moment for L/D = 1.0 [16]

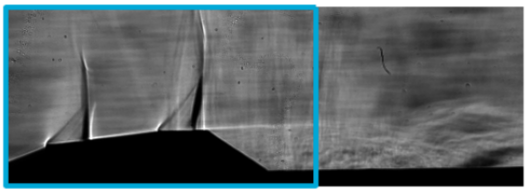

(a) Bi-conic nose (BC34 run 5 at the Schlieren test matrix in the appendices)

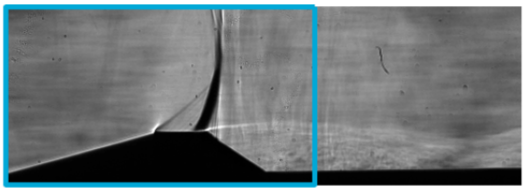

(b) Conic nose (C34 run 11 at the Schlieren test matrix in the appendices)

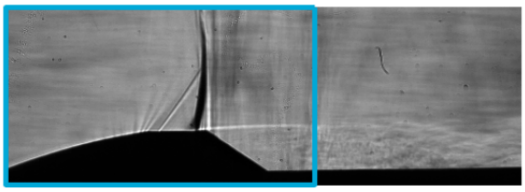

(c) Ogive nose (SH34 run 13 at the Schlieren test matrix in the appendices)

Figure 2.24: Nose shapes tested by Romero [49]

2.2.4 Nose shape

Romero [49] investigated the effect of nose shapes on the flow structure around Model 11, testing three configurations: conic, bi-conic (Model 11), and ogive noses. Expansion wave and shockwave structures were observed at locations of geometric change, resulting in two shockwaves for the bi-conic nose and a single shockwave for both the conic and ogive noses. The expansion fan on the conic nose exhibited a similar structure to that of the bi-conic case, whereas the ogive nose produced a more dispersed expansion fan, as shown in Figure 2.24. The conic nose exhibited the highest oscillations in the shockwave, followed by the ogive and then the bi-conic nose. However, since the bi-conic configuration generates two shockwaves, it may actually induce higher buffet loads than the ogive nose.

2.3 Angle of attack effect

The introduction of an angle of attack disturbs the flow symmetry. While comparing a straight and bulbous PLF, Coe [14] found that the pressure fluctuations were generally larger on the leeward side than on the windward side. In their unsteady pressure-sensitive paint (uPSP) measurements at a 4° angle of attack, Panda et al. [43] identified two axial vortices on either side of the vehicle, which altered the shear layer reattachment point on the second stage.

D'Aguanno et al. [19] observed that the fluctuation of the first shock on the leeward side of

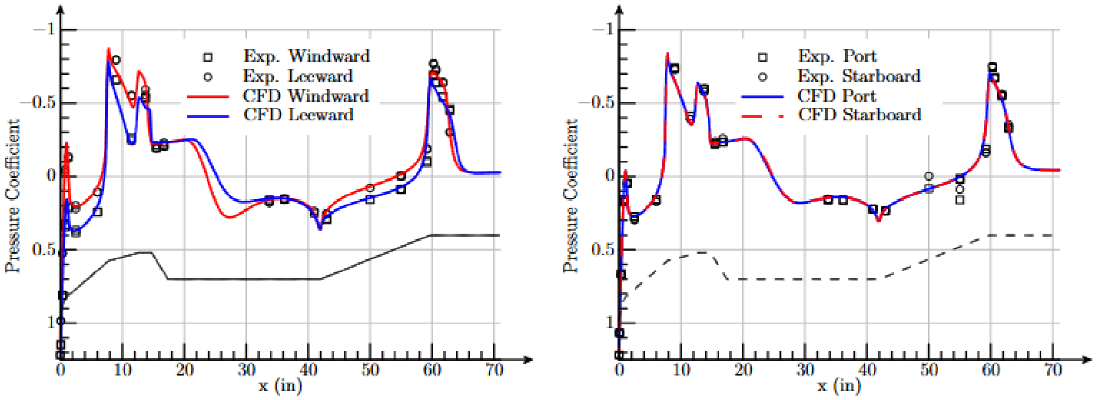

(a) Lateral (b) Pitch

Figure 2.25: Effect of AoA on mean C_p [40]

the VEGA-E model at an angle of attack of 4° was more energetic and had shifted slightly upstream. They also found that the fluctuations of schlieren image pixel intensities in the separation region decreased on the leeward side while increasing on the windward side. In contrast, Romero [49] reported that the shock waves on the leeward side of Model 11 appeared stabilised; however, she also noted that experimental errors could have influenced this observation.

Murman et al. [40] similarly found that the mean pressure coefficient (C_p) corresponding to the shock locations was lower on the windward side than on the leeward side. Conversely, the reattachment location exhibited the opposite trend. This indicates that the flow velocity within the supersonic pockets on the windward side is higher than that on the leeward side. No significant difference was observed between the port and starboard sides, as noted from the Figure 2.25

2.4 Mach number effect

Mach number is a critical parameter in launch vehicle aerodynamics. Multiple studies have reported that shock waves begin to appear over Model 11 at a Mach number of approximately 0.7 [13, 14, 15, 42, 19], although Suresh and Sivan [5] considered $M = 0.8$ as the critical Mach number for HHF. Pressure fluctuations increase progressively as the flow transitions from low to high transonic speeds. At supersonic speeds, these fluctuations become negligible, indicating the presence of fully developed shock waves and expansion fans.

The unsteady pressure-sensitive paint (uPSP) map in Figure 2.26 identifies the reattachment location as a broad band of elevated $C_{p,\text{rms}}$. The measured separation length increases up to $M = 0.92$ and then decreases as the flow becomes supersonic, a trend attributed to lifting of the shear layer at the shock foot due to SWBLI [43]. Consistent with this behaviour, Ericsson [24] reported a shorter separation length at $M = 1.0$ than at $M = 0.81$.

Romero [49] observed that with increasing Mach number on Model 11, shock waves shifted downstream and exhibited increased intensity and unsteadiness. The reported separation length ranged from $4.8h$ to $5.33h$ from the boattail corner. However, discrepancies arose between measurements obtained from oil flow visualisation and PIV, primarily due to the smeared reattachment region evident in the oil flow data. The width of this smeared region was found to grow from 0.1 D at $M = 0.7$ to 0.14 D at $M = 0.8$, indicating an increase in the range of oscillation. Liu et al. [35] observed that the reattachment location moved downstream until M = 1, and then shifted back upstream at M = 1.08. This effect was attributed to higher levels of shear layer lifting at the foot of the shock at M = 1.

Similarly, D'Aguanno et al. [20] reported a slight reduction in separation length at $M = 0.7$ compared to $M = 0.8$ on the VEGA-E model. The absence of pressure fluctuations at the lower Mach number was noted, indicating more stable flow behaviour. The study further documented a 4% increase in the separation area when the Mach number rose from $M = 0.7$ to $M = 0.8$, underscoring the increasing influence of SWBLI at higher transonic speeds.

Thus, overall, increasing the Mach number up to $M = 1$ tends to amplify the unsteadiness of shock waves and shifts the reattachment point progressively downstream, driven by enhanced shear layer lifting and stronger SWBLI. Beyond $M = 1$, the flow exhibits increased stability, characterised by well-formed expansion fans and shock structures, resulting in a noticeable reduction in unsteady behaviour across both the PLF and the reattachment region.

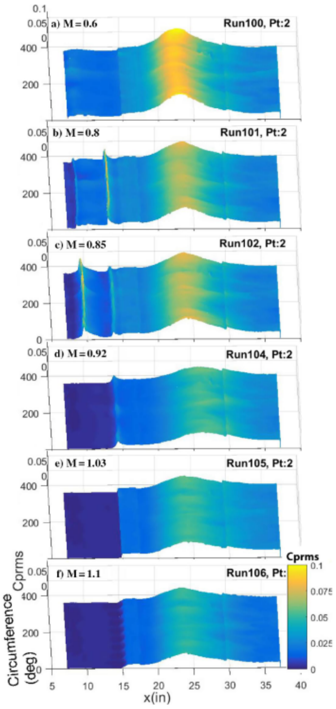

Figure 2.26: Distribution of C_{prms} on Model 11 [43]

2.5 Shockwave Boundary-Layer Interaction

It has been noted that at Mach numbers slightly below unity, stronger SWBLI leads to shear layer lifting, affecting the location and range of the reattachment point. Thus, an effort to describe the physics behind SWBLI is made in this section. In an inviscid fluid, the pressure rise across a shock wave is discontinuous. However, when a shock impinges on a viscous boundary layer, this pressure increase becomes significantly smeared. The subsonic channel within the boundary layer permits upstream propagation of pressure information; as a result, the incoming flow is notified of the downstream pressure rise before reaching the shock. The boundary layer responds to this information by thickening, or under sufficiently strong adverse pressure gradients, by separating [50].

Different forms of SWBLI are classified based on their interaction with geometry, such as a compression ramp, an oblique impinging shock, or a normal shock wave. Since normal shock waves are observed in the schlieren images of Model 11, only that case is discussed here.

As described by Babinsky and Harvey [6], two SWBLI topologies can be distinguished based on shock strength: weak and strong interactions. These are sometimes referred to as attached and separated shock interactions as well [50]. For sufficiently low adverse pressure gradients, the boundary layer impinged by a normal shock over a flat plate is able to remain attached. This is referred to as a weak interaction and is shown in Figure 2.27(a). The subsonic channel transmits pressure signals upstream, leading to thickening of the boundary layer before the shock. The associated curvature in the streamlines generates a series of compression waves, which eventually coalesce into the normal shock. These waves produce a smeared shock foot, and the pressure rise begins at the first compression wave itself. This smearing reduces the adverse pressure gradient at the shock foot and helps the boundary layer remain attached.

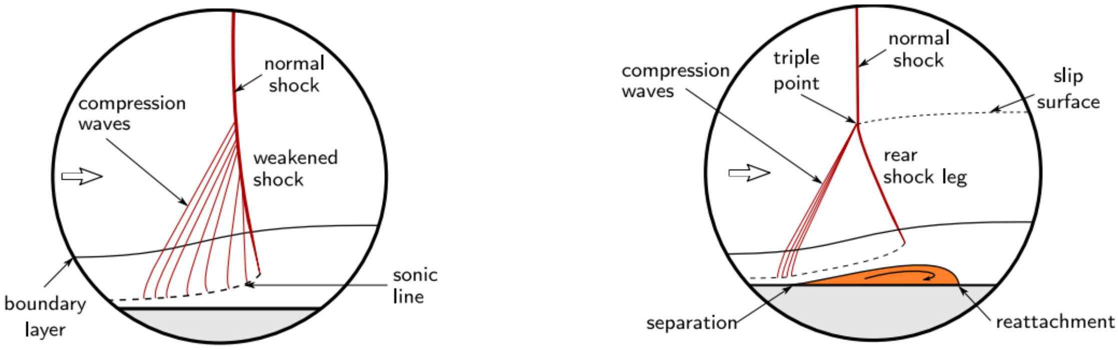

(a) Weak interaction

(b) Strong interaction

Figure 2.27: Strong and Weak SWBLI [50]

When the adverse pressure gradient is high enough, a thin separation bubble is observed. As shown in Figure 2.27(b), the presence of a separation bubble curves the streamlines upward and produces a series of compression waves. These waves coalesce into an oblique shock wave.

To realign the flow streamlines with the wall after the reattachment of the separation bubble, a second shock wave is formed downstream. These two oblique shock waves connect with the normal shock outside the boundary layer at a triple point. Due to this unique configuration, the resulting structure is referred to as a λ (lambda) shock wave. Since the decrease in total pressure across the normal shock is larger than that across the two oblique shocks—while the static pressure remains the same—a slip line emanates from the triple point.

In summary, both weak and strong SWBLI mechanisms result in energy loss and boundary layer thickening, thereby increasing their vulnerability to downstream separation. However, strong interactions—characterised by shock-induced separation bubbles and λ shock structures—exert a more profound influence on flow unsteadiness and reattachment behaviour. This explains the observed lifting of the shear layer and the variation in reattachment length seen in experimental studies at $M < 1$.

2.6 Backward Facing Step

Since boattail angles exceeding 30° exhibit flow behaviour similar to a backward-facing step (BFS), relevant literature on BFS flows was reviewed. BFS flow is a fundamental separation model in fluid dynamics with substantial theoretical and engineering relevance. It appears in various applications such as airfoils at high angles of attack, spoiler-induced flow separation, wake regions behind vehicles, and flow around buildings. BFS flows capture essential characteristics of separated flows, including shear layer detachment, vortex evolution, and reattachment [11]. In the context of launch vehicles, BFS models are frequently employed to approximate base flow conditions [7, 8, 52, 58, 62, 55].

One of the early BFS studies, conducted at NASA Ames Research Centre in the late 1980s [22], quantified unsteadiness in the reattachment region using laser doppler velocimetry (LDV), thermal-tuft visualisation, and pressure transducers at $M = 0.128$. A schematic illustrating the separation zone, shear layer, and reattachment region is shown in Figure 2.28. The reattachment location was found to fluctuate between $5.3H$ and $6.8H$, exhibiting a low-frequency flapping motion with a Strouhal number (St_H) of 0.06 based on step height. A second dominant frequency at $St_H = 0.2$, attributed to vortex shedding, was also identified.

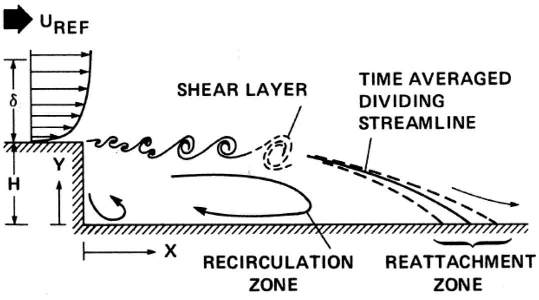

Figure 2.28: Schematic of BFS flow [22]

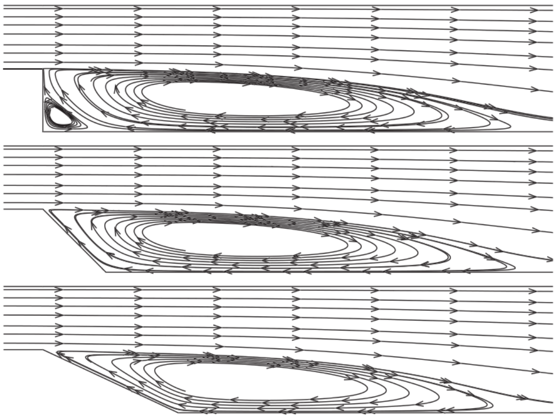

Figure 2.29: Streamlines for BFS with inclination angles $90°$, $45°$, and $25°$ [38]

A significant portion of the BFS literature focuses on low Reynolds number flows. Gentile [**gentile_symmetry_nodate**] experimentally investigated the influence of varying afterbody diameters and observed that increasing the diameter reduced the separation region and promoted the formation of a secondary recirculation zone. Reattachment lengths ranged from $2.5h$ to $4.2h$ at $Re_D = 67{,}000$. Similarly, Hudy et al. [28] reported that the reattachment location shifted downstream with an increase in Reynolds number. A comparison between 2D and 3D cases revealed a shorter reattachment length in the 3D configuration, attributed to a thinner boundary layer and increased Reynolds stress levels.

To clarify how step inclination shapes the separation and reattachment topology in BFS flow, Louda et al. [38] performed a numerical study of incompressible turbulent channel flow at $Re = 15{,}000$ with systematically varied step angles. They found the primary reattachment point to be largely insensitive to inclination, whereas the secondary recirculation region disappeared when the inclination was reduced to $45°$. Figure 2.29 presents computed streamlines for $90°$, $45°$, and $25°$.

Scharnowski and Kähler [51] reported that at $M = 0.7$, the reattachment location was approximately $1D$ downstream, corresponding to $3.52h$. In the high transonic regime, Vikramaditya et al. [62] observed reattachment distances ranging from 4.4 to 6 step heights. In the supersonic regime, the reattachment location was significantly shorter, typically around 3 to 4 step heights [8, 34, 10, 27, 36].

Modal analysis of BFS flows in the transonic regime reveals the presence of two dominant structures, as previously noted by David et al. [22]. The most significant is commonly referred to as the flapping mode, which contributes to the oscillation of the shear layer. The second mode is associated with the shedding of vortical structures. Schrijer et al. [55] attributed these modes to Strouhal numbers of $St_D = 0.14$ for flapping and $St_D = 0.4$ for vortex shedding, based on the model diameter. These modes are shown in Figure 2.30. In BFS literature, the flapping mode is also referred to as the step mode [7], and the vortex shedding is often referred to as the undulation mode.

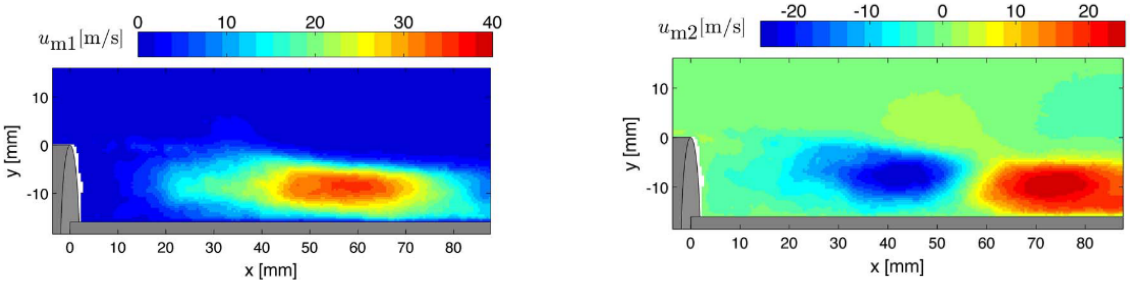

(a) Flapping mode

(b) Undulation mode

Figure 2.30: POD modes identified by Schrijer et al. [55]

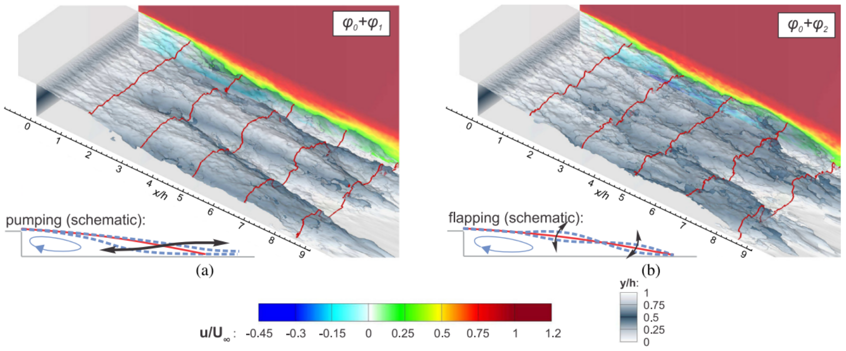

Figure 2.31: DMD modes in the launcher base flow [58]

Scharnowski et al. [58] carried out experimental and numerical investigations of the turbulent wake behind a generic launcher model at M = 0.7. They identified two dominant DMD modes, characterised by Strouhal numbers $St_h = 0.01$ and $St_h = 0.07$, corresponding to wake flapping and vortex shedding, respectively. These modes, superimposed on the mean flow, are illustrated in Figure 2.31. The modes were referred to as the pumping and flapping modes instead.

Gentile [**gentile_symmetry_nodate**] also identified similar structures at lower speeds. She observed that increasing the afterbody diameter decreased the intensity of the flapping mode. As expected, the size of the vortical structures also reduced and moved upstream with larger afterbody diameters. The Strouhal number associated with flapping ranged between 0.001 and 0.01, while that for vortex shedding was approximately 0.2.

2.6.1 Control strategies

Since it is commonly observed in various scenarios, extensive research has been conducted on controlling the flow around a BFS. In their review of BFS flows, Chen et al. [11] discussed

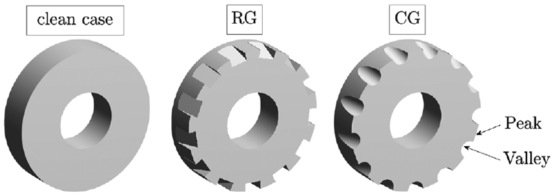

Figure 2.32: Trailing edges used by Scharnowski et al.[52]

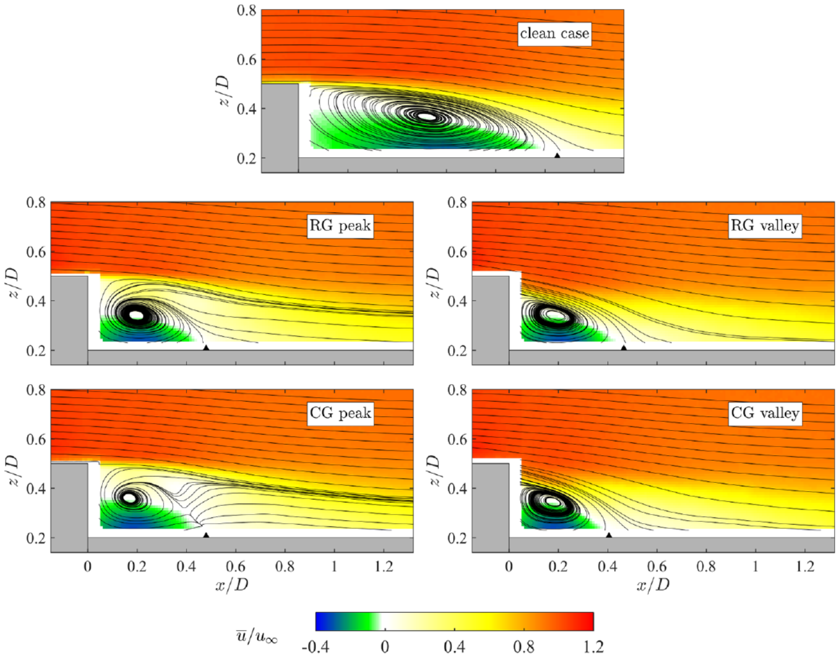

Figure 2.33: Mean streamwise flow for different trailing edges on a launcher base[52]

various passive and active flow control techniques; however, most were only related to low subsonic speeds. Prominent passive control strategies for transonic BFS flows include streamwise grooves [52], staggered steps [7], and porous surfaces [32]. These passive flow control strategies have been shown to effectively reduce both pressure fluctuations and separation length in transonic BFS configurations.

While advancing research on launcher base flows, Scharnowski et al. [52] investigated the effects of circular and rectangular grooves in reducing wake unsteadiness and separation length. Their study found that the separation length decreased from $1.05D$ in the clean case to approximately $0.48D$ behind the peak and $0.41D$ behind the valleys for the circular groove configuration, where D represents the diameter of the launcher model. Figure 2.32 illustrates the different trailing edge configurations used in this study, while Figure 2.33 presents the mean streamwise velocity distribution. The study also observed an increase in flow fluctuations within the separation layer near the BFS. However, the reduced fluctuations at a longer momentum arm contributed to lower overall loads on the reattaching surface.

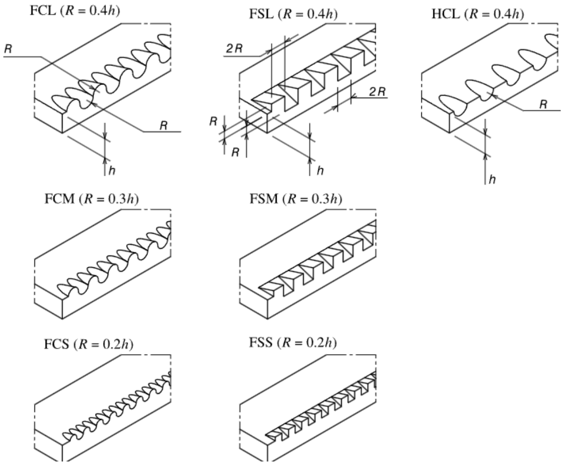

Figure 2.34: Flow control devices used by Bolgar et al.[7]

A study by Bolger et al. [7] investigated passive flow control techniques, specifically circular and rectangular convoluted trailing edges on a BFS, and found them to be significantly more effective than active flow control methods. Three configurations of convoluted trailing edges were examined: Fully Circular (FC), Fully Square (FS), and Half Circular (HC) steps, as illustrated in Figure 2.34. Among these, the Fully Square - Large (FSL) configuration demonstrated the highest efficiency, achieving an 80% reduction in mean separation length and approximately 50% reduction in fluctuations within the separation region under transonic conditions. The study further found that, with proper sizing, certain configurations could completely eliminate the step mode associated with BFS. Figure 2.35 presents the frequency spectrum for the baseline configuration, while Figure 2.36 displays the frequency spectrum for cases with flow control devices, clearly highlighting the significant reduction in dominant frequencies. The researchers also suggested that the ability to suppress step mode may be linked to whether the protrusion of the flow control devices is greater or smaller than the boundary layer thickness, though this hypothesis remains unvalidated.

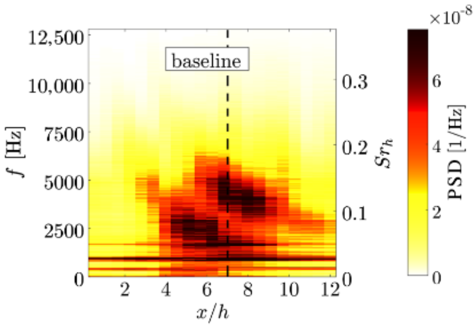

Figure 2.35: PSD of baseline configuration tested by Bolgar et al. [7]

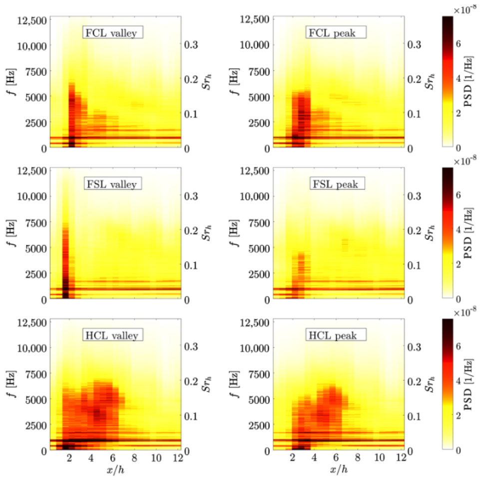

Figure 2.36: PSD of flow control devices used by Bolgar et al. [7]

2.7 Research Gap

The Coe and Nute Model 11 has become a benchmark configuration in recent efforts to characterise the buffet phenomenon over HHF, particularly in the transonic regime. While much work has focused on analysing the flow field under different operational conditions—such as changes in Mach number and angle of attack—significant attention has also been given to modifying design parameters including nose cone shape, fairing length, and boattail angle (see Section 2.2). These studies provide valuable insights into the flow separation mechanisms and unsteady pressure loads acting on launch vehicle fairings.

For example, the works of Romero [49], Kumar et al. [33], and Li et al. [35] explored how reducing the boattail angle or altering fairing length can attenuate pressure fluctuations and modify the shock structure. Analogously, research into BFS flows [7, 52] has shown that edge geometry—such as grooves or ramps—can dramatically reduce unsteadiness by altering the reattachment characteristics of the shear layer.

However, a critical geometric parameter remains conspicuously underexplored in both HHF and BFS literature: **the boattail edge radius**. Most studies consider sharp corner at the boattail transition, but none systematically investigate how varying the curvature at this location affects the onset of flow separation, SWBLI, or the development of the unsteady wake. In BFS configurations, studies such as those by Scharnowski et al. [52] demonstrated that altering trailing edge geometry strongly influences the modal structure of the wake. This raises the question of whether similar improvements can be realised in HHF configurations by tuning the boattail edge curvature.

In addition to geometric factors, another notable shortcoming in existing literature is the limited use of advanced flow decomposition tools. While flow visualisation and surface pressure measurements have been widely used, very limited studies have applied data-driven techniques such as *Proper Orthogonal Decomposition (POD)* or *Spectral POD (SPOD)* or *Dynamic Mode Decomposition (DMD)* to analyse HHF unsteadiness. These modal techniques, successfully used in BFS studies [**gentile_symmetry_nodate**, 58, 55], offer powerful insights into coherent structures, dominant frequencies, and energy content of the flow. Their application to HHF cases, particularly in high-fidelity experimental setups, could provide an unprecedented understanding of unsteady aerodynamic behaviour.

In summary, this thesis identifies two primary research gaps:

1. The lack of systematic investigation into the effect of the **boattail edge radius** on flow separation and unsteady loading in HHF and BFS-type flows.
2. The absence of **modal analysis techniques** in current HHF studies to characterise and isolate dominant unsteady flow structures.

The work presented in this thesis is aimed at addressing both these gaps through a combination of targeted geometry variations and advanced post-processing of flow dataset.

2.8 Research Question

Guided by the foregoing review, this study addresses two unresolved issues: (i) the aerodynamic role of the **boattail edge radius** in HHF, and (ii) the use of **data-driven modal analysis** to characterise the associated unsteadiness. These aims motivate the following research questions:

- **RQ1: How does the boattail edge radius affect the flow in a hammerhead fairing configuration?**
  - What happens to the overall flow field?
  - Does the edge radius promote shock-induced separation?
  - How does it affect the separation length and reattachment location?
- **RQ2: Characterization of the unsteady flow field**
  - What spatial modes govern the unsteadiness in the separation region?
  - Can these modes be linked to specific features, such as boattail curvature or shock motion?
  - Can these modes be linked to specific frequencies?

Together, these research questions aim to both quantify the aerodynamic implications of boattail edge radius and enhance our understanding of flow physics through state-of-the-art analysis techniques. The answers will contribute to designing more robust and stable launch vehicle fairing geometries for transonic regimes.

3

Experimental Methodology

This chapter details the experimental methodology adopted in this thesis. First, the research facility and test conditions are outlined. Second, the experimental setups used in each campaign are described together with the underlying theory of the measurement techniques. Third, an uncertainty analysis is presented. Finally, the chapter concludes with the post-processing workflow applied to the acquired datasets.

3.1 Wind Tunnel Facility

All experiments presented in this thesis were conducted in the TST-27 wind tunnel, shown in Figure 3.1, at TU Delft. The TST-27 is a transonic-supersonic blowdown wind tunnel, capable of operating across a broad range of Mach numbers from 0.5 to 4.2. This is made possible through the use of two distinct variable-geometry mechanisms that enable either transonic or supersonic operation.

The wind tunnel is composed of five major sections(refer to Figure 3.2):

1. Pressure vessel
2. Settling chamber
3. Adjustable convergent-divergent nozzle for supersonic conditions
4. Test section
5. Variable-area throat with rods and central wing for transonic conditions

Transonic conditions ($M = 0.5$–0.85) are achieved using a variable-area throat located downstream of the test section. This mechanism consists of eight biconvex rods extruding from the top and bottom tunnel walls, along with a central wing that provides fine control (Figure 3.3. The central wing, with a thickness of 6 mm, is rotatable between 0° and 60°. For each run, the rod extrusion height (denoted as H in Figure 3.3) is pre-set based on the target Mach number. The final Mach number adjustment is accomplished via feedback-controlled rotation of the central wing using a LabVIEW program, enabling precision control to the

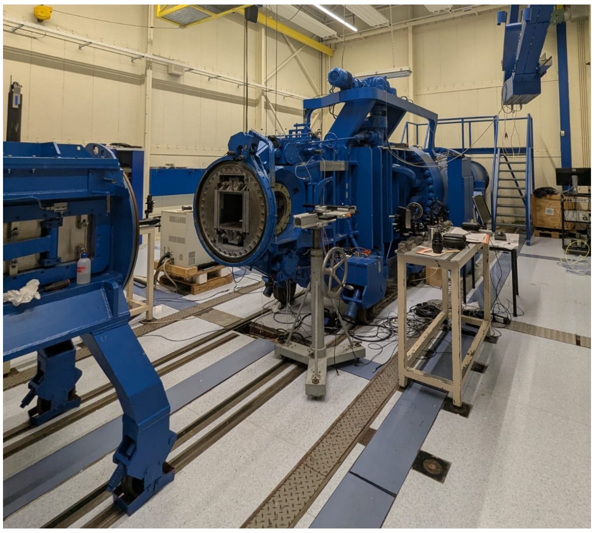

Figure 3.1: TST-27 wind tunnel at TU Delft

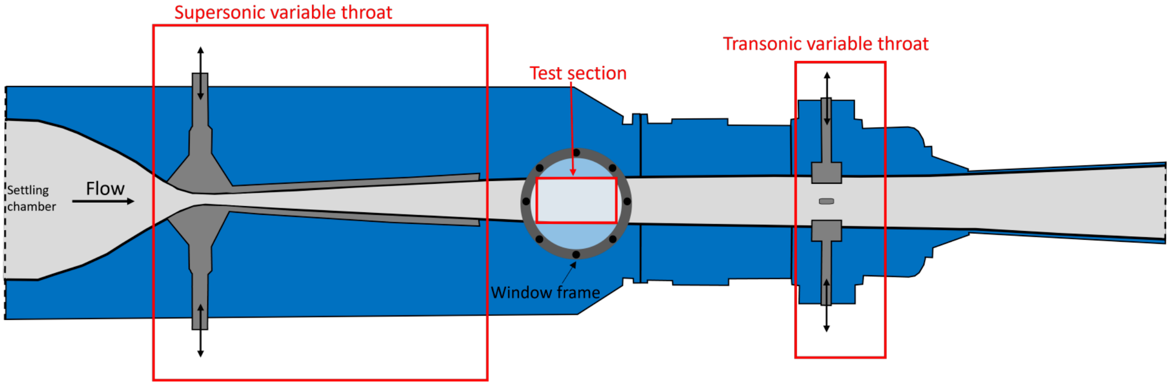

Figure 3.2: Schematic of TST-27

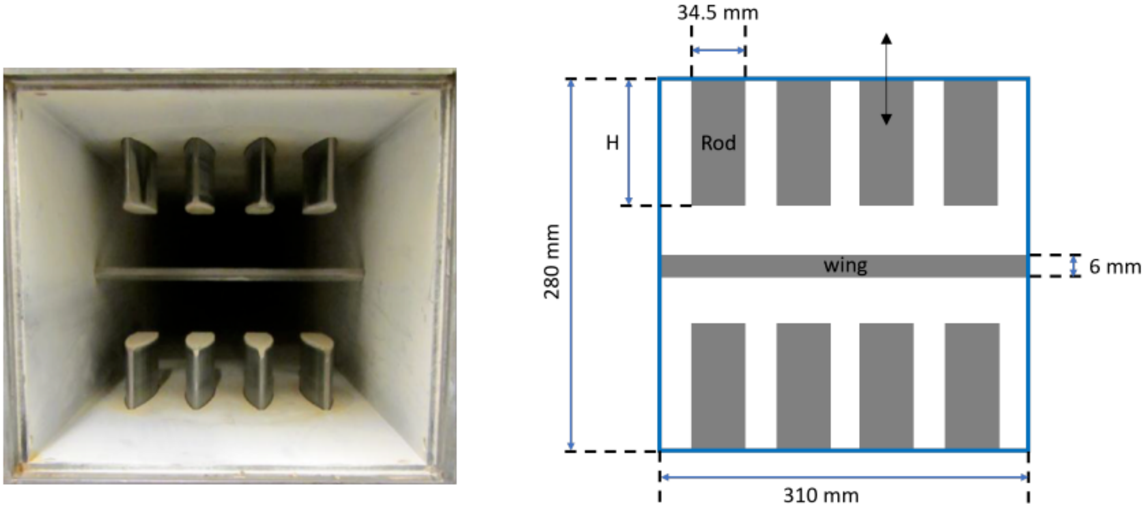

Figure 3.3: Transonic throat visualisation(left) and schematic(right)

Figure 3.4: WT Model viewed through the optical window

third decimal place. Supersonic conditions ($M = 1.15$–4.2) are attained using a variable convergent-divergent nozzle located upstream of the test section. By modifying the throat area of this nozzle, the tunnel can generate a range of supersonic Mach numbers.

Air is supplied to the tunnel from a high-capacity pressurised vessel with a volume of $300\,\mathrm{m}^3$, which can be charged up to a maximum pressure of ≈ 41 bar. The vessel is filled using a multi-stage compressor, which typically operates overnight prior to testing. Due to system limitations, the total run time is restricted to approximately 300 seconds per day, maintaining vessel pressure above 20 bar to ensure adequate flow quality.

The settling chamber pressure is adjustable independently from the vessel pressure and can be varied between 1.5 and 4 bar. This allows for testing at different Reynolds numbers. Under transonic operation, the tunnel can reach Reynolds numbers up to 38 million per meter, while under supersonic conditions, this can increase up to 130 million per meter.

The TST-27 features a modular test section design and offers three configurations: closed wall, slotted wall, and perforated wall. Each test section is mounted on wheels for ease of interchangeability and is connected to the rest of the tunnel using quick-lock couplings. These couplings incorporate safety trip switches, which prevent the tunnel from operating unless all connections are secure. All experiments in this thesis were carried out using the closed-wall test section, which includes 300 mm diameter quartz glass windows for optical access, shown in Figure 3.4. The test section itself measures 255 mm in height and 280 mm in width.

3.2 Flow conditions

The wind tunnel's flow conditions are determined primarily by the Mach number in the test section and the total pressure and total temperature inside the pressure vessel. The total temperature (T_0) is measured prior to the experiment, and the tunnel operator has control over the total pressure(p_0). The flow conditions at the test sections can be derived using the isentropic relations if the conditions in the pressure vessel are known. Specifically, the static conditions at the test section can be calculated using the total pressure and total temperature values and the set Mach number:

$$T_\infty = T_0 \left(1 + \frac{\gamma - 1}{2} M_\infty^2\right)^{-1} \tag{3.1}$$

$$p_\infty = p_0 \left(1 + \frac{\gamma - 1}{2} M_\infty^2\right)^{\frac{-\gamma}{\gamma-1}} \tag{3.2}$$

with $\gamma = 1.4$, T_0 and T_∞ the total and static temperatures, p_0 and p_∞ the total and static pressures. From these static conditions, the density at the test section can be derived assuming a calorically perfect and ideal gas using Equation 3.3 with $R = 287.057 J/kg.K$. The flow velocity is calculated from the set Mach number and static temperature at the test section using the Equation 3.4

$$\rho_\infty = \frac{p_\infty}{R T_\infty} \tag{3.3}$$

$$U_\infty = M_\infty \sqrt{\gamma R T_\infty} \tag{3.4}$$

The dynamic viscosity is calculated using Sutherland's law given in Equation 3.5, where $\mu_{ref} = 1.7616 \times 10^{-5} kg/ms$, $T_{ref} = 273K$ and $S = 111K$. With the dynamic viscosity, density and flow velocity, the Reynolds number at the test section can be calculated using the fairing diameter, $D = 50mm$, as the reference length.

$$\mu_\infty = \mu_{ref} \left(\frac{T_\infty}{T_{ref}}\right)^{\frac{3}{2}} \left(\frac{T_{ref} + S}{T_\infty + S}\right) \tag{3.5}$$

$$Re_\infty = \frac{U_\infty \rho_\infty}{\mu_\infty} \tag{3.6}$$

Within this thesis, tests were conducted at three different Mach numbers: 0.6, 0.7, and 0.8. The total pressure was set at 2 bar to maintain a lower mass flow rate, thus aiding in longer runtimes. The total temperature is 288 K. Table 3.1 shows the flow conditions for all the tested Mach numbers.

Parameter	Symbol	Mach 0.6	Mach 0.7	Mach 0.8	Unit
Total Temperature	T_0	288.00	288.00	288.00	K
Total Pressure	p_0	2.00	2.00	2.00	bar
Static Temperature	T_∞	268.66	262.29	255.32	K
Static Pressure	p_∞	1.57	1.44	1.31	bar
Flow Velocity	U_∞	197.15	227.69	256.26	m/s
Density	ρ_∞	2.03	1.91	1.79	kg/m^3
Dynamic Viscosity	μ_∞	1.74×10^{-5}	1.71×10^{-5}	1.67×10^{-5}	kg/m.s
Reynolds Number	Re	1.15×10^6	1.28×10^6	1.37×10^6	–

Table 3.1: Flow properties at different Mach numbers

3.3 Test models

The wind tunnel model used in this study is based on the upper section of Model 11, originally investigated by Coe and Nute [13]. Model 11 has a bi-conic nose and a 34° boattail at the end of the fairing and is widely referenced in the literature for validating the transonic buffet phenomenon in HHF. The model was initially developed for Romero's thesis [49], who explored the aerodynamic effects of varying nose shapes and boattail angles. Accordingly, the model features a modular design that allows testing with three different nose shapes—bi-conic, conic, and ogive—as well as three boattail angles—5°, 15°, and 34°. All nose variants are spherically blunted. The bi-conic nose with a 34° boattail angle corresponds to the original Model 11 configuration tested by Coe and Nute, and it serves as the baseline for this thesis.

The model was scaled such that the PLF diameter is 50 mm, matching the FESTIP configuration previously tested at TU Delft [55]. A schematic of the wind tunnel model is provided in Figure 3.5, highlighting the interchangeable nose and boattail sections. To promote a fully turbulent boundary layer, a trip strip was placed at approximately 5% of the model length, as shown in Figure 3.6. This placement is consistent with the recommendation by Pope and Goin [**noauthor_high-speed_nodate**], who identified it as the most favourable transition location. This is further supported by Garbeff et al. [25], who observed laminar-to-turbulent transition wedges near the sphere-cone junction—coinciding with the 5% location.

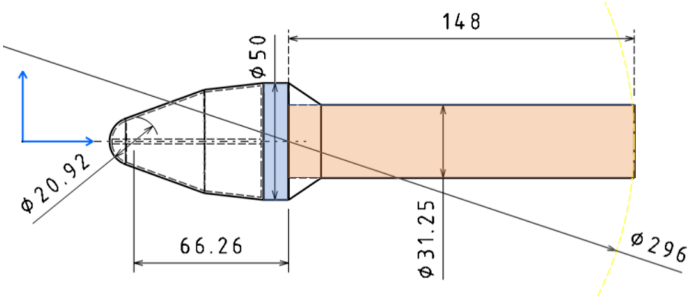

Figure 3.5: Schematic of the wind tunnel model assembly

Figure 3.6: WT model with trip strip on the nose

To investigate the first research question, a series of boattail segments with varying radii was designed. A systematic approach was employed to determine appropriate radius values. Approximating the model as a flat plate, the turbulent boundary layer thickness at the separation point (located 85 mm downstream along the model surface) was estimated using the Reference Temperature Method[2] for the highest Mach number of interest, $M = 0.8$. The resulting turbulent boundary layer thickness was approximately 1.719 mm. Based on this, a range of boattail radii was selected, starting near the boundary layer thickness and extending to an order of magnitude larger. The selected radius values and their corresponding R/δ ratios are provided in Table 3.9. It should be noted that these are approximate values, and no effort was made to compute the actual boundary layer thickness for each condition.

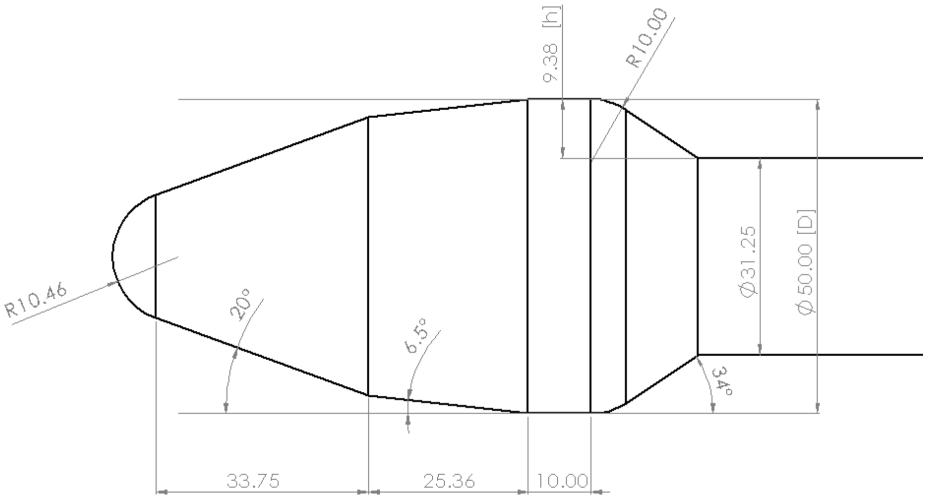

Figure 3.7: Model dimensions in mm

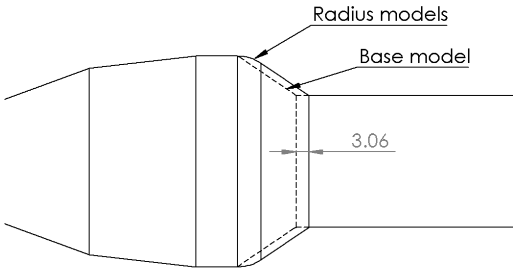

Figure 3.8: Design of the radius model in comparison with the base model

Radius [mm]	R/δ [-]
3	1.745
6	3.490
10	5.817
15	8.725
20	11.633

Figure 3.9: Boattail radii and corresponding R/δ values based on estimated boundary layer thickness $\delta = 1.7190\,\text{mm}$

The dimensions of the R10 model are presented in Figure 3.7. The radius models were manufactured as extensions of the base model rather than as edge fillets, in order to allow straightforward integration with the existing base model produced for Romero's thesis [49]. Figure 3.8 illustrates the comparison between the radius models and the base configuration; shown specifically is the R10 model.

3.3.1 Blockage

The presence of a model in a wind tunnel introduces blockage effects that alter the effective freestream velocity experienced by the model compared to the set tunnel velocity. These blockage effects arise from two main sources: solid blockage and wake blockage. Solid blockage occurs because the physical volume of the model reduces the available flow area. To satisfy the continuity equation, the flow must accelerate around the model, increasing the local velocity. Wake blockage, on the other hand, arises from the low-velocity region that forms behind the model. Since the wake reduces the average velocity downstream, the overall tunnel flow must accelerate to maintain mass conservation. Together, these effects result in a higher effective freestream velocity at the model than initially intended, necessitating appropriate corrections during data analysis. In this thesis, only an estimate of the solid blockage is given, and the wake blockage is neglected.

At $\alpha = 0°$, the maximum solid blockage ratio (B_r) relative to test section area is given by:

$$B_r = \frac{\pi \cdot D^2}{4 \cdot H_T \cdot W_T} = 0.02750 \tag{3.7}$$

where D is the fairing cylinder diameter of the windtunnel model, and H_T and W_T are the height and width of the test section, respectively. The blockage is further increased for $\alpha = 4°$.

The cross-section of a cylinder under an angle becomes an ellipse, with minor axis of length $D/2$ and a major axis length $D/2 \cdot \sec(\alpha)$. This results in a solid blockage ratio of

$$B_r = \frac{\pi \cdot D^2 \cdot \sec(4^\circ)}{4 \cdot H_T \cdot W_T} = 0.02757 \tag{3.8}$$

which is about 0.2% increase. However, the introduction of the angle of attack leads to the model being situated off the centre of the test section, producing different levels of blockage on the windward and leeward side of the model. On the leeward side, a diverging section is created, whereas on the windward side, a converging section is created. Due to the angle, the wake blockage increases, and since the force distribution is asymmetric, other blockage effects, such as buoyancy due to lift, may also come into play. Note that the model probe downstream of the test section will also induce blockage effects.

Earlier studies conducted in the same facility using Model 11 [49] and VEGA-E [20] have shown that measurements at $M = 0.8$ correspond more closely with literature data at $M = 0.85$. A simple verification of the +0.05 blockage effect reported by Romero and D'Aguanno was performed using a one-dimensional flow assumption, yielding an estimated ΔM between +0.04 and +0.07, as presented in Appendix **??**. Since a systematic evaluation of blockage effects has not been conducted, all data presented in this thesis remain uncorrected for blockage.

3.4 Experimental setup

3.4.1 Schlieren

The term *Schlieren* refers to optical inhomogeneities in transparent media, and the *Schlieren method* is an optical technique used to visualise these variations. Such inhomogeneities are primarily caused by spatial changes in the refractive index of the medium, which arise from local variations in density and temperature. As light rays traverse regions of differing refractive index, they bend (refract), and the Schlieren system captures these deflections to provide insight into the flow field. Since refractive index gradients are typically associated with changes in pressure, density, or temperature, the technique is particularly well-suited for studying compressible flows.

Although not the original inventor, August Toepler significantly advanced the schlieren technique into its modern form by introducing essential components such as mirrors or lenses, slit light sources, and knife edges. Early systems employed objective lenses to collimate and focus the light beam; however, these were later replaced by mirrors due to their lower cost and ability to offer a wider, aberration-free field of view. Mirror-based schlieren systems must operate off-axis to prevent the reflected beam from retracing its path, a configuration that introduces optical aberrations such as coma and astigmatism.

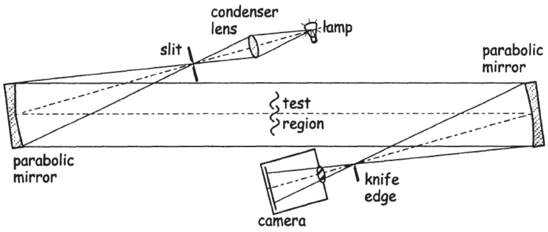

Figure 3.10: Schematic of Z-type Schlieren

The most widely used configuration today is the *Z-type Schlieren system*, illustrated schematically in Figure 3.10. The name derives from the characteristic Z-shaped path followed by the light rays. This setup employs two identical parabolic mirrors, each slightly tilted off-axis in opposite directions and placed on either side of the test section. By tilting the mirrors symmetrically, optical aberrations introduced by one mirror are effectively cancelled by the other. On the source side, a light source (typically a lamp), a condenser lens, and a slit or pinhole are used to create a point source of light. The collimated beam reflects off the first parabolic mirror and passes through the test section. On the opposite side, the second mirror focuses the beam onto a knife edge located at its focal point. A camera positioned behind the knife edge records the schlieren image.

The knife edge partially obstructs the focused light. When refractive index gradients are present in the test section—typically due to density gradients in the flow—the light rays are deflected. These deflected rays are either blocked or transmitted past the knife edge, resulting in variations in image brightness. Dark regions form where light is blocked, while bright regions appear where light passes through. This contrast enables the visualization of key flow features such as shock waves, boundary layers, shear layers, and vortices.

Sensitivity

To quantify the sensitivity of the schlieren system, it is useful to evaluate the ratio of the change in light intensity on the sensor due to refraction to the baseline intensity, expressed as $\Delta I/I$. Let a be the diameter of the pinhole and $\bar{a}$ the effective unblocked beam width perpendicular to the knife edge. For a homogenous test section with no density variation, the intensity on the sensor is uniform and proportional to $\bar{a}$. When inhomogeneities are present, the change in light intensity ΔI is linked to the beam deflection angle ϵ_y, and the corresponding beam shift Δa can be written as:

$$\Delta a = f \tan(\epsilon_y) \tag{3.9}$$

Assuming the knife edge is oriented horizontally and the beam is deflected vertically, the relative intensity change becomes:

$$\frac{\Delta I}{I} = \frac{\Delta a}{\bar{a}} = \frac{f}{\bar{a}} \tan(\epsilon_y) \tag{3.10}$$

where f is the focal length of the schlieren mirror. The deflection angle can be related to refractive index gradients across the test section:

$$\frac{\Delta I}{I} = \frac{f}{\bar{a}} \int_{z_1}^{z_2} \frac{1}{n} \frac{\partial n}{\partial y} \, dz \tag{3.11}$$

Here, z is the depth-wise direction through the test section, and n is the refractive index, defined as:

$$n = \frac{c}{c_v} \tag{3.12}$$

where c is the speed of light in vacuum and c_v in the medium. The refractive index relates to fluid density via the Gladstone-Dale equation:

$$n = 1 + k\rho \tag{3.13}$$

where k is the Gladstone-Dale constant (for air, $k_{\text{air}} \approx 0.23$ cm^3/g), which depends on temperature and light wavelength. Substituting into Equation 3.11, the expression simplifies to:

$$\frac{\Delta I}{I} = \frac{fk}{\bar{a}} \int_{z_1}^{z_2} \frac{\partial \rho}{\partial y} \, dz \tag{3.14}$$

assuming $n \approx 1$. For a vertical knife edge, the sensitivity changes direction:

$$\frac{\Delta I}{I} = \frac{fk}{\bar{a}} \int_{z_1}^{z_2} \frac{\partial \rho}{\partial x} \, dz \tag{3.15}$$

Equations 3.14 and 3.15 imply that the sensitivity of the system increases with larger mirror focal lengths and smaller pinhole diameters. Since changing mirrors is impractical, sensitivity is typically controlled by adjusting the pinhole size. These equations also highlight that schlieren visualises a path-integrated effect of density gradients across the test section.

Figure 3.11: KE filter to visualise density gradients in both directions

Knife Edge Orientation

The orientation of the knife edge is critical in determining the direction of the density gradients that the system captures. While oblique orientations exist, the most commonly used are horizontal and vertical.

In the vertical orientation, the knife edge blocks rays deflected horizontally, making the system sensitive to horizontal density gradients, as described by Equation 3.15. Conversely, in the horizontal orientation, the system detects vertical gradients, as described by Equation 3.14. Although real deflection may occur in both directions, each orientation captures only one component. To overcome this limitation, one may record schlieren images using both orientations. Alternatively, a specialised filter, as shown in Figure 3.11, can be used to visualise density gradients in both directions simultaneously.

Exposure Time

The optimal exposure time depends on factors such as flow velocity, light intensity, and magnification. Longer exposures can improve signal-to-noise ratio under low-light conditions but may introduce motion blur, smearing fine structures in the flow. For capturing instantaneous features, shorter exposure times are preferred, though this may reduce image brightness. Therefore, exposure time must be experimentally optimized for each configuration to balance sharpness and intensity.

Campaign

A high-speed schlieren campaign was conducted using a Photron Mini AX100 camera to capture unsteady flow phenomena. Since the full sensor can only operate at 4 kHz, achieving higher acquisition rates required cropping the sensor, which reduced the effective Field of View (FoV). Additionally, the FoV depended on the focal length of the lens used. A shutter speed of 1/100,000 s was employed to reduce motion blur while maintaining sufficient image brightness.

The schematic of the setup is shown in Figure 3.12. A Z-type Schlieren configuration was employed, consisting of two parabolic mirrors. The light source was focused through a pinhole to produce a beam approximately 6 mm in diameter. This configuration enhanced sensitivity to pressure fluctuations while preserving an adequate observable range of flow features. The setup featured a 360° rotatable knife edge. Preliminary tests were conducted at 5 kHz to determine the optimal knife-edge orientation. As illustrated in Figure 3.13, both horizontal and vertical orientations were evaluated. While the vertical orientation provided greater clarity for shock and expansion features, the horizontal orientation offered better visibility of both shock structures and the shear layer. Consequently, the horizontal knife-edge configuration was selected for the main campaign.

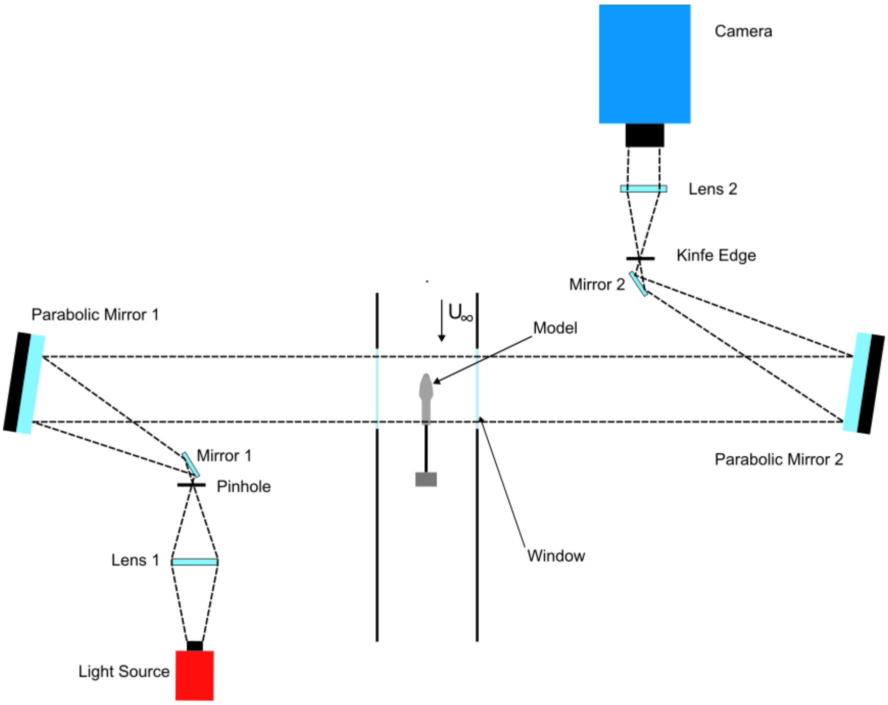

Figure 3.12: Schematic of the Schlieren setup

Three distinct FoVs were used throughout the campaign, each tailored for specific observations. These are illustrated in Figure 3.14 and summarised in Table 3.2:

- **FoV 1:** Standard configuration to simultaneously capture shock waves and the separation region (Figure 3.14(a)).
- **FoV 2:** High-sampling view (60 kHz) focused on the separation zone to detect high-frequency structures (Figure 3.14(b)).
- **FoV 3:** Close-up visualisation of shock-induced separation interactions (Figure 3.14(c)).
- **FoV 4:** Wider FoV for trial runs (Figure 3.14(d)).

According to the Nyquist criterion, the maximum resolvable frequency $f_{\max}$ is given by:

$$f_{\max} = \frac{\mathrm{SR}}{2} \tag{3.16}$$

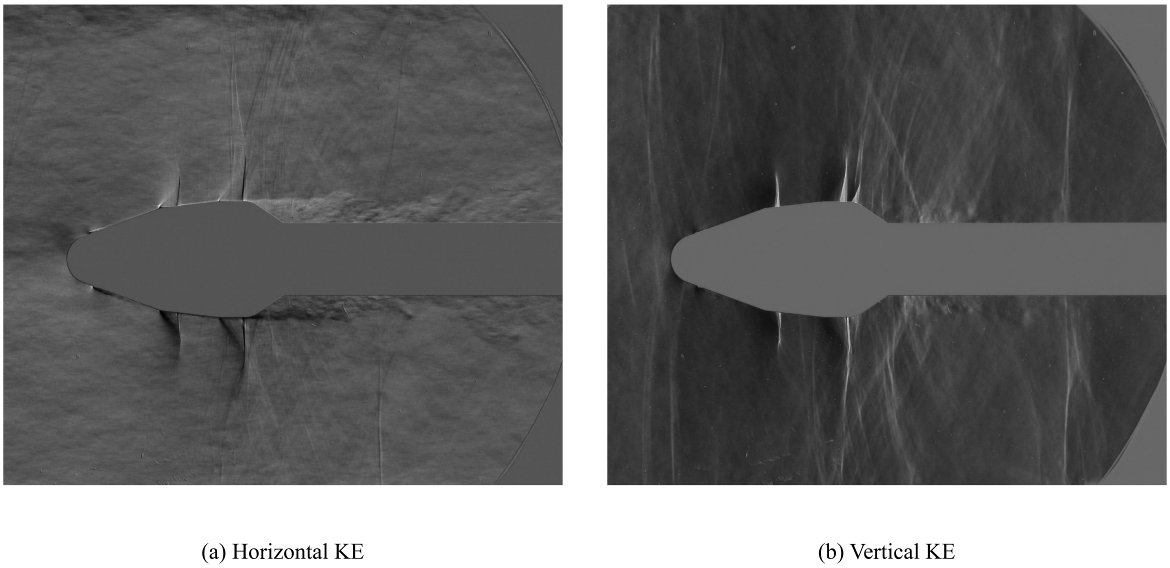

(a) Horizontal KE (b) Vertical KE

Figure 3.13: Different KE orientations

where SR is the sampling rate. For instance, a 25 kHz acquisition rate allows for resolving frequencies up to 12.5 kHz.

FoV	Lens [mm]	Acquisition Frequency [kHz]	Resolution [pixels]
FoV 1	180	25	384×256
FoV 2	300	60	256×128
FoV 3	500	25	384×256

Table 3.2: Acquisition and setup parameters for different FoVs used in Schlieren visualisation

3.4.2 Oil Flow Visualisation

Oil flow visualisation is a valuable technique for obtaining a preliminary understanding of the surface flow field. It enables visualisation of how the external airflow interacts with the surface of a solid body and reveals key mean flow features such as the laminar-to-turbulent transition point, shockwave footprints, separation and reattachment points, surface vortices, and the direction of wall streamlines [18].

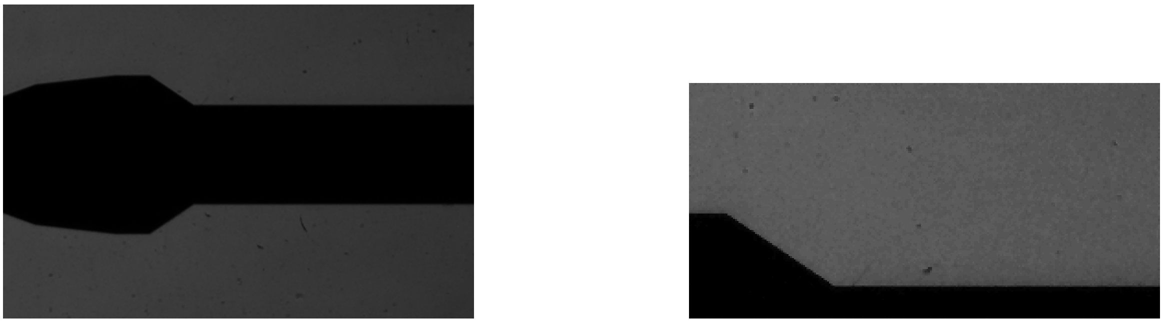

(a) FoV 1

(b) FoV 2

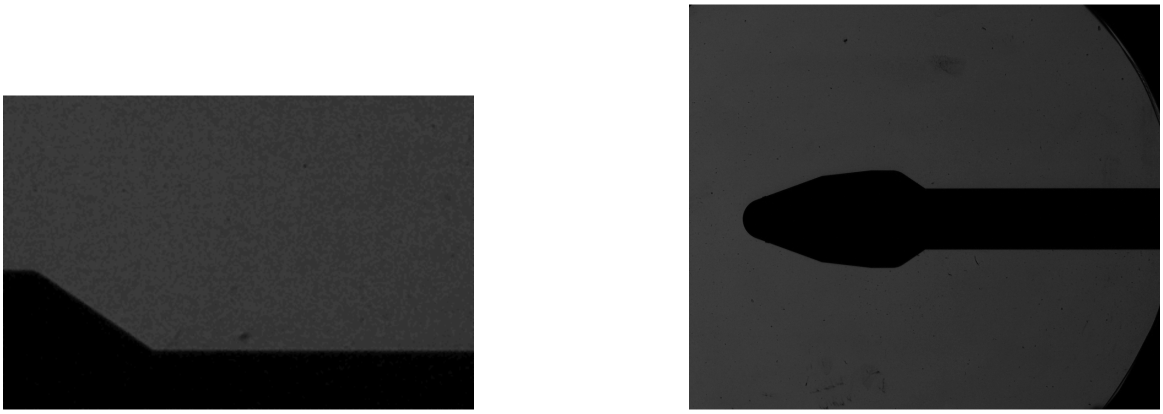

(c) FoV 3

(d) FoV 4

Figure 3.14: Fields of view employed in Schlieren visualisation

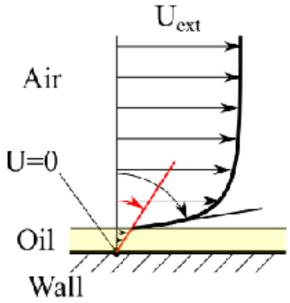

Figure 3.15: Boundary layer profile with a thin oil layer [56]

To implement oil flow visualisation, the model surface is coated with a thin layer of oil mixed with a dye to enhance contrast and visibility. The typical boundary layer profiles in both air and oil layers are presented in Figure 3.15. The no-slip boundary condition is applied at the solid wall, and at the oil–air interface, both velocity and shear stress are continuous. Due to the significantly higher viscosity of the oil compared to air, the velocity gradient within the oil layer must be very small to satisfy shear stress continuity[56]. This relationship is expressed in Equations 3.17 and 3.18.

$$\tau_{\text{oil}} = \tau_{\text{air}} \Rightarrow \mu_{\text{oil}} \left(\frac{\partial u}{\partial y}\right)_{\text{oil}} = \mu_{\text{air}} \left(\frac{\partial u}{\partial y}\right)_{\text{air}} \tag{3.17}$$

$$\mu_{\text{oil}} \gg \mu_{\text{air}} \quad \Rightarrow \quad \left(\frac{\partial u}{\partial y}\right)_{\text{oil}} \ll \left(\frac{\partial u}{\partial y}\right)_{\text{air}} \tag{3.18}$$

Since the oil velocity at the wall is zero due to the no-slip condition, and the velocity gradient is minimal, the oil layer moves extremely slowly compared to the freestream air. Combined with the oil's high viscosity and very small film thickness, the resulting flow is in the creeping (Stokes) flow regime, where viscous and pressure forces dominate. In the absence of separation, pressure gradients in the oil layer are negligible, and oil streaks closely follow the direction of the wall shear stress, effectively visualising surface streamlines.

Oil accumulation patterns provide valuable insights into the local wall shear stress distribution. The height of accumulated oil is inversely proportional to the local shear stress: regions with high wall shear stress appear darker due to the oil being swept away, while areas with low shear stress retain more oil and thus appear lighter. An example of a laminar-to-turbulent transition visualized using oil flow is shown in Figure 3.16. In the laminar boundary layer, oil tends to accumulate due to the relatively low shear stress. Upon transition to turbulence, the wall shear stress increases, causing the accumulated oil to be rapidly displaced. Further downstream, as the turbulent boundary layer develops and wall shear stress begins to decrease again, oil accumulation increases once more. Flow separation is typically identified by a region of oil accumulation, whereas flow reattachment is characterised by a zone where oil is depleted.

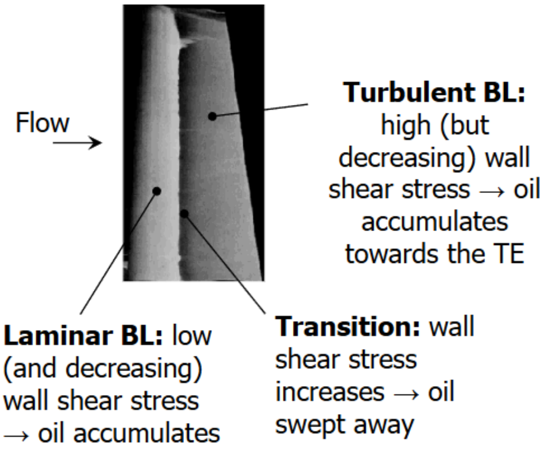

Figure 3.16: Oil flow visualisation over a wing model showing laminar-to-turbulent transition [56]

Campaign

In this thesis, oil flow visualisation is used primarily to study the mean separation behaviour of different boattail radii. A subset of configurations was selected based on preliminary Schlieren results. The R6 and R15 radius configurations were excluded from further oil flow testing; the reasoning behind this exclusion is discussed in Section 4.2.

All runs were recorded using a Nikon D3400 DSLR camera equipped with a 24.2 megapixel CMOS sensor with a pixel size of 3.89 μm, illuminated by a bright LED light source. The camera was positioned facing one of the optical windows of the wind tunnel to capture the temporal evolution of oil streak patterns. In addition to video capture, a high-resolution image was taken at the end of each run to identify and analyse mean flow features such as separation region, reattachment point, and shock locations. Figure 3.17 shows the experimental setup for the oil flow campaign.

3.4.3 Particle Image Velocimetry (PIV)

Particle image velocimetry (PIV) is a widely used, non-intrusive, and quantitative measurement technique in experimental fluid dynamics. Unlike point-based methods such as hot-wire anemometry (HWA) or laser doppler velocimetry (LDV), PIV provides a full-field representation of the velocity over a two-dimensional (planar or stereoscopic) or three-dimensional (tomographic) region of interest. While HWA and LDV can be employed to obtain spatially distributed data by traversing the measurement point, they cannot match the spatial resolution and coverage achievable through PIV.

The primary limitation of PIV lies in its temporal resolution. The high-energy pulsed laser systems required to illuminate the flow often constrain the sampling rate, making PIV less suitable for capturing high-frequency unsteady phenomena when compared to techniques like HWA or LDV. A typical PIV setup consists of three integrated subsystems: **illumination**,

Figure 3.17: Experimental setup for Oil flow campaign

seeding, and **imaging**. Figure 3.18 illustrates a standard two-dimensional, two-component (2D2C) PIV arrangement used in a wind tunnel. The core principle of PIV is based on acquiring two images of the seeded flow field in rapid succession by illuminating a laser sheet across the region of interest. From the image pairs, the displacement of particles over a known time interval can be tracked, resulting in a velocity vector field.

The laser illumination provides sufficient energy to make the particles visible to the camera by inducing light scattering. Seeding particles are carefully selected to ensure that they are neutrally buoyant and faithfully follow the local flow motion. The scattered light from the particles is recorded using a high-resolution camera, typically synchronised with the laser pulses. The captured image pair is divided into smaller interrogation windows, within which cross-correlation techniques are applied to determine the average particle displacement. Given

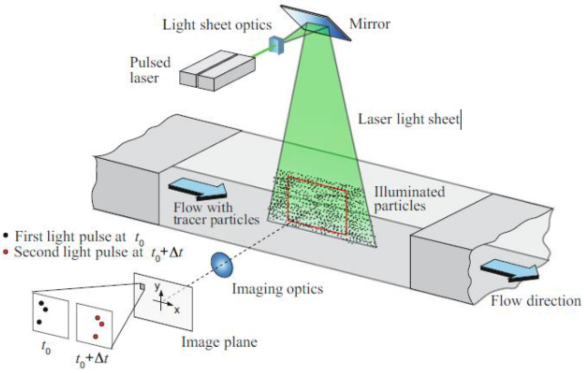

Figure 3.18: Schematic of 2D2C PIV setup

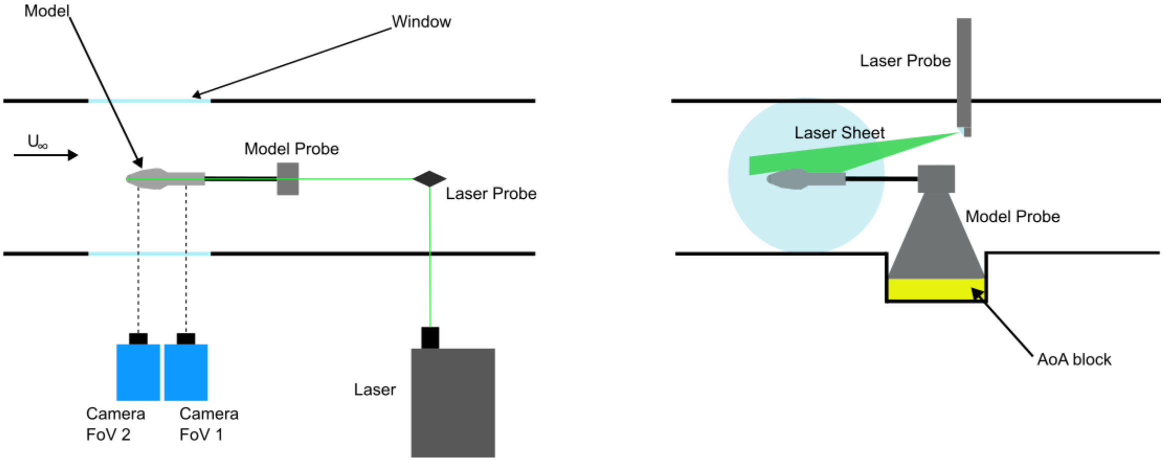

Figure 3.19: Schematic of PIV setup: Top view (left) Front view(right)

the time interval between the two exposures and the magnification factor of the imaging system, the velocity field can be accurately computed. This process results in a high-resolution, quantitative velocity map across the illuminated plane or volume.

Campaign

Since the model is axisymmetric and previous studies [19] have shown that the flow around HHF exhibits axisymmetric behaviour, a planar PIV campaign was conducted. A low-repetition-rate configuration was chosen to allow for higher spatial resolution, as the schlieren dataset already provided sufficient temporal resolution. To further enhance spatial resolution, two cameras with overlapping FoVs were employed. The complete PIV system, barring programmable timing unit (PTU), is illustrated in Figure 3.19, while the optical window setup used during the PIV campaign is shown in Figure 3.20. PIV measurements were carried out for only the R0, R10, and R20 configurations.

Laser system

The laser employed for this PIV campaign is a double-pulse Nd:YAG laser (Spectra Physics Quanta Ray PIV-400), delivering an energy output of $400mJ$ per pulse with a pulse duration of $6ns$. This short pulse duration ensures that particle displacement during illumination remains below 0.4 pixels, thereby enabling accurate velocity measurements without any motion blur in the particles. The laser operates at a wavelength of $532nm$ and a repetition rate of $10Hz$ between double pulses.

To deliver the laser into the wind tunnel test section, a custom-designed laser probe is used. This probe, designed by F. J. Donker Duyvis[23], is inserted downstream of the test section through an access port in the upper wall of the wind tunnel. It transforms the collimated laser beam into a thin laser sheet approximately $1.5mm$ in thickness, which is then directed to illuminate the region of interest on top of the model. The impact of the probe on the

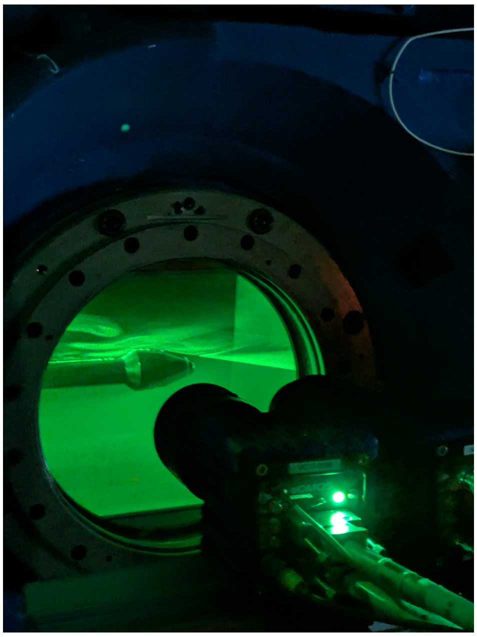

Figure 3.20: PIV setup

flowfield has been evaluated in prior schlieren tests conducted by Romero [49], who confirmed that its presence does not introduce significant disturbances.

Imaging system

The imaging system is governed by the thin lens equation, expressed as:

$$\frac{1}{f} = \frac{1}{d_i} + \frac{1}{d_o} \tag{3.19}$$

where f is the focal length of the lens, d_i is the image distance, and d_o is the object distance. Together with the magnification factor M, this equation determines the appropriate camera positioning relative to the test section for a given lens specification. The magnification factor maps entities from object space to image space and is defined as the ratio of image distance to object distance. It is equivalently expressed as the ratio of image size to object size:

$$M = \frac{d_i}{d_o} = \frac{h_i}{h_o} \tag{3.20}$$

where h_i and h_o denote the image and object sizes, respectively. The object size is dictated by the required FoV, while the image size is determined by the image sensor resolution and pixel size:

$$M = \frac{\text{pixel size} \times N_{\text{pixels}}}{\text{FoV}} \tag{3.21}$$

The choice of lens is directly dependent on the FoV requirements for the investigation. The oil flow measurements provided the necessary input to define the FoV for the PIV campaign. Since the boattail region is the primary region of interest, the FoV was centred accordingly to capture the relevant flow features. The objective was to include the shock wave structures, the boattail, and the mean reattachment location to obtain a comprehensive velocity field that complements the schlieren and oil flow measurements. Given the axisymmetric nature of the HHF flow field, only the upper portion of the model was investigated.

The FoV extends upstream of the first shock wave to downstream of the farthest reattachment location identified from the oil flow results, including an additional margin. This resulted in a FoV length of 135 mm. As two cameras were used for the campaign, two individual FoVs were acquired, with an overlap of approximately 5 to 7 mm to facilitate stitching during post-processing. This overlapping configuration ensured continuity and prevented data loss due to potential misalignment or experimental uncertainties.

Two LaVision Imager sCMOS cameras were used in this campaign, each required to achieve an FoV of 70 mm in length. The height of the FoV is relatively flexible, provided it extends beyond the supersonic pockets over the HHF model with sufficient margin. Each LaVision Imager sCMOS camera has a resolution of 2560 × 2160 pixels, with a pixel size of $6.5\,\mu$m × $6.5\,\mu$m. This results in a magnification factor of:

$$M = \frac{6.5 \times 10^{-6} \times 2560}{0.070} = 0.2377 \tag{3.22}$$

The corresponding FoV per camera is thus 70 mm × 59 mm. Figure 3.21 shows the two FoVs with the overlap. Though the cameras could operate at a maximum frame rate of 50 fps at full sensor resolution, the acquisition rate was restricted to $10Hz$ by the laser. The images have a colour depth of 16-bit and image acquisition was performed in double shutter mode with an interframing time of 120 ns.

Another important optical parameter is the f-number ($f_{\#}$), which is the ratio of the focal length of the lens to the aperture diameter. A higher $f_{\#}$ corresponds to a smaller aperture, resulting in reduced incident light on the sensor and consequently darker images. Moreover, the $f_{\#}$ strongly influences the depth of field, defined as the extent of the region that remains in focus. Increasing $f_{\#}$ increases the depth of field but may compromise overall image sharpness due to diffraction effects.

In order to ensure that the tracer particles illuminated by the laser sheet remain in focus for accurate cross-correlation, the depth of field must exceed the laser sheet thickness of 1.5 mm. The depth of field δz for a given magnification M and illumination wavelength λ is given by:

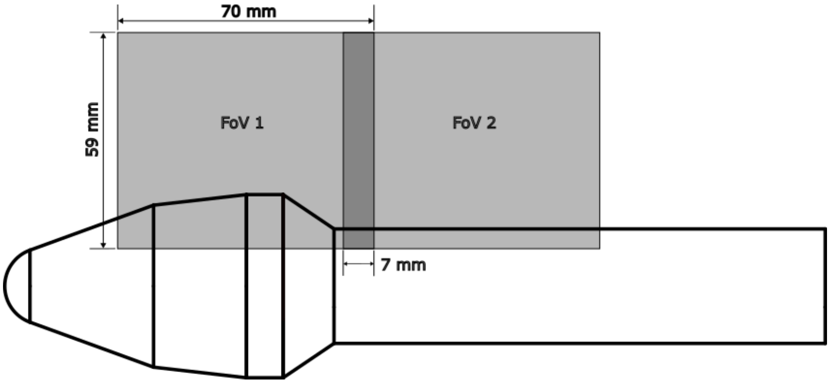

Figure 3.21: FoVs employed in PIV

$$\delta z = 4.88 \times \lambda \times f_{\#}^{2} \left(\frac{M+1}{M} \right)^{2} \tag{3.23}$$

Rearranging the above expression allows estimation of the required $f_{\#}$ as:

$$f_{\#} \geq \sqrt{\frac{\delta z}{4.88 \times \lambda \left(\frac{M+1}{M} \right)^{2}}} = 4.6 \tag{3.24}$$

Thus, to ensure the laser sheet remains in focus, the $f_{\#}$ must be at least 4.6. During the campaign, the laser sheet was initially focused at $f_{\#} = 2.8$ and later increased to $f_{\#} = 8$ to provide a sufficient safety margin.

Seeding system

The seeding system consists of a seeding generator, a seeding rake, and tracer particles. For this campaign, a PIVPART 45 seeding generator (PIVTEC GmbH) was used. The generator was directly connected to the seeding rake, which contains multiple nozzles for particle injection and is positioned in the settling chamber of the wind tunnel. The seeding density can be regulated by adjusting the number of active nozzles through an external control box. In this study, all 45 nozzles were activated to ensure sufficient seeding density throughout the test section.

The tracer particles used were DEHS (Di-Ethyl-Hexyl-Sebacat) droplets, selected for their favourable flow-tracking characteristics. These particles had a median diameter of $1\,\mu$m and a particle response time τ_p of $2\,\mu$s, which quantifies the time required for a particle to adapt to changes in the surrounding flow velocity. A low response time ensures that the particles closely follow rapid velocity fluctuations, making them suitable for time-resolved measurements. To guarantee consistent seeding quality, the generator was operated at a pressure of 3 bar.

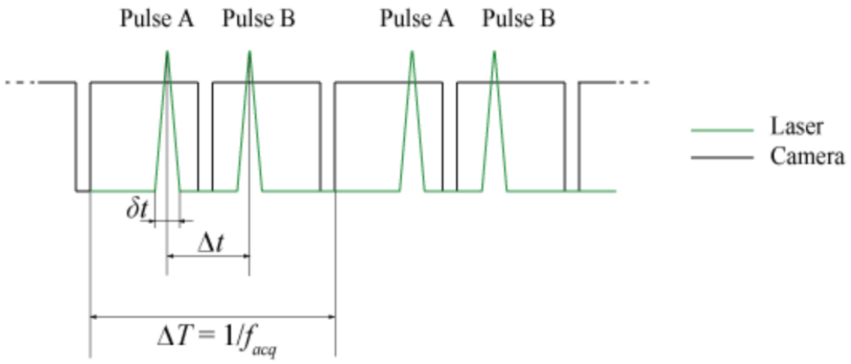

Figure 3.22: Timing diagram for PIV double frame recording

PTU

A programmable timing unit (PTU) was used to synchronise the trigger signals between the cameras and the laser system, controlled via the LaVision DaVis 8.1 software. Since the PIV measurements were conducted in double-shutter mode, two primary parameters needed to be specified: the acquisition frequency f_{acq}, which defines the interval between successive double pulses, and the pulse separation time Δt, which governs the time delay between the two exposures in each double pulse. The corresponding timing diagram illustrating the coordination between the camera exposure and laser illumination is shown in Figure 3.22. It is important to note that the laser illuminates the tracer particles only for a brief moment within the camera's exposure window, ensuring crisp capture of particle displacement.

The acquisition frequency was limited by the laser hardware to 10 Hz, while the selection of the pulse separation time Δt involved a trade-off. An excessively large Δt would cause significant particle displacement, potentially resulting in particles leaving the laser sheet and becoming undetectable. Conversely, an excessively small Δt would produce insufficient particle displacement, degrading the cross-correlation accuracy due to the low signal-to-noise ratio. Practical guidelines suggest that a particle displacement of approximately 20 pixels yields optimal cross-correlation accuracy, considering an uncertainty of around 0.1 pixels and the interrogation window size[57]. The optimal pulse separation time can be estimated using the magnification factor M and the expected maximum velocity U, according to:

$$\Delta t = \frac{\Delta x_{\text{pixels}} \times \text{pixel size}}{M \times U} \tag{3.25}$$

where Δx_{pixels} is the target particle displacement in pixels, and the pixel size is $6.5\,\mu$m. The image length consists of 2560 pixels, corresponding to a field of view length of 70 mm. For the Coe and Nute Model 11 configuration, the maximum velocity in the flow field, as reported by Romero [49], was approximately 350 m/s. Substituting these values yields a pulse separation time (Δt) of approximately $1.5\,\mu$s.

3.5 Uncertainty analysis

Uncertainty analysis is a critical component of experimental investigations and must be carefully considered to ensure both the validity and repeatability of the measurements. Therefore, multiple runs were conducted for each configuration to ensure sufficient statistical convergence.

An evaluation was carried out to determine the required number of image pairs necessary to ensure that the statistical uncertainty remained within acceptable limits for the PIV campaign. The following expressions were used to estimate the uncertainty in the mean velocity U and the velocity standard deviation σ:

$$\epsilon_U = \frac{\sigma_U}{U}\frac{k}{\sqrt{N}} \quad \text{and} \quad \epsilon_\sigma = \frac{\sigma_U}{U}\frac{k}{\sqrt{2N}} \tag{3.26}$$

where σ_U/U is the turbulence intensity, k is the coverage factor associated with the confidence interval, and N is the number of samples acquired.

A turbulence intensity of 10% was assumed, with a target uncertainty of 1%. A Gaussian probability distribution was assumed, and a confidence level of 95% was selected, corresponding to $k = 2$. From these expressions, it is evident that the uncertainty in the velocity standard deviation imposes the stricter constraint. Setting ϵ_σ to 1% yields a minimum required sample size of $N = 200$. To ensure robust statistics, this limit was conservatively increased to 350 samples per run. However, for subsequent modal analyses, a larger dataset was desirable. To balance practical constraints on wind tunnel operation and to verify repeatability, three independent runs of 350 samples each were conducted for every configuration, resulting in a total of 1050 samples per case.

It is also important to note that not all uncertainty arises from statistical sources alone. For oil flow measurements, the base configuration was repeated twice to check for consistency. Similarly, for schlieren imaging, each configuration was tested over a wider field of view to ensure measurement reliability.

In high-speed flows, an important source of PIV uncertainty arises from the finite response time of the seeding particles. The particle slip velocity — defined as the relative velocity between the fluid and the particle — can be estimated following Melling [1]:

$$\vec{U}_{slip} \approx \tau_p \cdot \vec{a}_p \tag{3.27}$$

where τ_p is the particle response time, estimated as 2 μs for DEHS particles (Ragni et al. [47]), and $\vec{a}_p$ is the particle acceleration:

$$\vec{a}_p = \frac{du_p}{dt} = \frac{u_p - u_f}{\tau_p} \tag{3.28}$$

Assuming small particle lag and quasi-steady flow, this may be approximated by the convective derivative:

$$\vec{a}_p \approx \vec{U} \cdot \nabla \vec{U} = \vec{U} \cdot \left(\frac{\partial u}{\partial x} + \frac{\partial v}{\partial y} \right) \tag{3.29}$$

Thus, the slip error becomes:

$$\epsilon_{slip} \approx \tau_p \cdot \vec{a}_p = \tau_p \cdot \vec{U} \cdot \left(\frac{\partial u}{\partial x} + \frac{\partial v}{\partial y} \right) \tag{3.30}$$

This slip uncertainty becomes most significant near shock waves and separation zones where velocity gradients are large.

The cross-correlation process used in PIV also introduces uncertainty in the individual velocity vectors, estimated following Humble et al. [29]:

$$\epsilon_{cc} = \frac{\epsilon_{corr}}{M \delta t} \tag{3.31}$$

where ϵ_{corr} is the correlation uncertainty, typically assumed to be 0.1 pixels for planar PIV, M is the magnification factor, and δt is the pulse separation time.

The interrogation window size introduces spatial resolution limitations, as only wavelengths larger than twice the window size can be accurately resolved. For single-step PIV processing, the measured-to-true velocity ratio can be expressed as [54]:

$$\frac{u}{u_0} = \text{sinc}\left(\frac{WS}{\lambda} \right) \tag{3.32}$$

This error is minimised when multi-step correlation is used, particularly for $WS/\lambda < 0.5$. Since the smallest resolvable scale in the flow is approximately twice the interrogation window size [31], an uncertainty of $\epsilon_{WS} < 1\%$ is typically assumed [61, 18].

Schlieren measurements are also subject to uncertainty, particularly because shock waves appear as projections rather than cross-sectional features. The schlieren image represents the integrated refractive effects across the test section, resulting in the visual appearance of a thicker shock than physically present. This can be quantified as half the measured shock thickness t_{SW} [18]:

$$\epsilon_{Sch} = \frac{t_{SW}}{w} \approx 1.5 \text{ mm} \tag{3.33}$$

Finally, additional uncertainty arises from wind tunnel operation and model setup. The angle of attack was controlled with a precision of ±0.2°, and minor fluctuations in Mach number were observed across individual runs.

3.6 Post Processing

3.6.1 Schlieren images processing

Schlieren datasets enable extraction of both qualitative and quantitative information about the general flow field. Given their high temporal resolution, these datasets are particularly well-suited for spectral analysis. However, due to the presence of static noise from dust on the optical windows and lenses, a set of 200 background images (acquired without flow) is recorded before each run. The median of these images is computed and subtracted from each flow image to minimize static artifacts.

Following background correction, several post-processing steps are performed. To extract general flow features, the mean and standard deviation of pixel intensities are computed. For efficient memory usage, each image is processed sequentially in a loop where the pixel intensities are accumulated. This allows only a single image to be stored in memory per iteration. The resulting summed intensity matrices are used to compute the mean ($\bar{I}$) and standard deviation (σ) as defined in Equations 3.34 and 3.35:

$$\bar{I} = \frac{1}{N}\sum I \tag{3.34}$$

$$\sigma = \bar{I'} = \sqrt{\bar{I^2} - \bar{I}^2} = \sqrt{\frac{1}{N}\sum I^2 - \left(\frac{1}{N}\sum I\right)^2} \tag{3.35}$$

Here, I represents the pixel intensity and N denotes the total number of images in the dataset.

The unsteady motion of shockwaves can be analysed using spectral techniques, as demonstrated by d'Aguanno [18] and Romero [49]. These methods also provide insight into dominant frequencies present within the flow domain. Given a time-domain signal $x(t)$, its Fourier Transform is given by:

$$X(f) = \int_{-\infty}^{\infty} x(t) \cdot e^{-i2\pi ft}\, dt \tag{3.36}$$

However, real-world signals are discrete and finite in length. The corresponding Discrete Fourier Transform (DFT) is therefore defined as:

$$X_k = \sum_{n=0}^{N-1} x_n \cdot e^{\frac{-i2\pi kn}{N}} \tag{3.37}$$

While the DFT suffices for noise-free signals, experimental data often contain significant random variations. In such cases, it is preferable to compute the Power Spectral Density (PSD), which describes how signal power is distributed across frequency. Formally, the PSD is defined as the Fourier Transform of the autocorrelation function:

$$P(f) = \sum_{k=-\infty}^{\infty} r(k) \cdot e^{-i2\pi fk} \tag{3.38}$$

where $r(k)$ denotes the autocorrelation function:

$$r(k) = E\left[x(t) \cdot x(t-k)\right] \tag{3.39}$$

Although this is the formal definition, it is seldom used in practice due to computational complexity. A more practical approach involves computing the squared magnitude of the Fourier Transform and applying appropriate normalisation. For a single-sided PSD using N samples and a sampling frequency f_s, the PSD is given by:

$$PSD(f) = \frac{2}{N \cdot f_s} \cdot |X(f)|^2 \tag{3.40}$$

In this work, Welch's method is adopted to improve statistical robustness and reduce the variance of the PSD estimate, albeit at the cost of frequency resolution. The signal is divided into overlapping segments, each of which is multiplied by a window function (commonly Hanning) to mitigate spectral leakage. The fast Fourier transform (FFT) is computed for each windowed segment, and the resulting periodograms are averaged to yield the final PSD:

$$P(f) = \frac{1}{L} \sum_{j=1}^{L} P_j(f) \tag{3.41}$$

Here, $P_j(f)$ represents the PSD of the j-th segment, and L is the total number of segments. A typical overlap of 50% is used. This averaging process significantly reduces the noise in the spectral estimate and is particularly useful when analyzing experimental datasets. To aid interpretation in log-log plots, the PSD is also premultiplied by frequency in this thesis.

The Welch parameters used for spectral analysis in this study are summarized in Table 3.3.

Table 3.3: Welch method parameters used for PSD computation.

Parameter	Value
Window function	Hanning
Segment length (n_{perseg})	1024 samples
Overlap percentage	50%

3.6.2 PIV processing

As discussed in section 3.4.3, the post-processing involves cross-correlating an interrogation window between the image pairs, resulting in one velocity vector for that interrogation window. The processing of PIV data is performed in DaVis 8.4 software. To optimise the cross-correlation, a set of pre-processing steps is done. First, a time-minimum subtraction filter is applied to reduce the background contribution across all the images. Further, a min-max filter with a filter size of 10 pixels is used to normalise the intensities of the particles and increase contrast. This pixel size was found to yield the best results for the dataset under consideration. The pre-processed image pair is shown in Figure with the interrogation window.

The acquired image pairs were processed using cross-correlation to extract the velocity field. A multi-pass approach was employed, wherein progressively smaller interrogation windows were used to improve spatial resolution. This method is particularly effective when particle displacements are large, as it mitigates limitations imposed by the quarter-window rule, which constrains the maximum resolvable displacement.

The first pass was performed using a 128×128 pixel square interrogation window with 50% overlap. This provided an initial coarse estimate of the displacement field. Subsequently, three refinement passes were conducted using 32×32 pixel circular windows with 75% overlap. The use of overlapping windows ensures that particle displacements extending beyond the size of a single window are adequately captured.

This configuration yielded approximately 42 velocity vectors per step height, providing sufficient resolution to accurately characterise the flow field. The complete set of processing parameters is summarised in Table 3.4.

Parameter	Value
Vector spacing	$43/h$
Final window size	32×32 px
Window overlap	75%

Table 3.4: PIV processing parameters. h is the boattail step height

Finally, a post-processing step is applied to the velocity fields to detect outliers. A universal outlier detection was applied with a threshold value of 2, which was chosen following the results from Westerweel and Scarano [63], who observed 90% of spurious data being filtered with such a value. A filter size of 7×7 pixels was used in this step. After filtering the outliers, the average and standard deviation of the velocity fields were obtained, and the velocity field

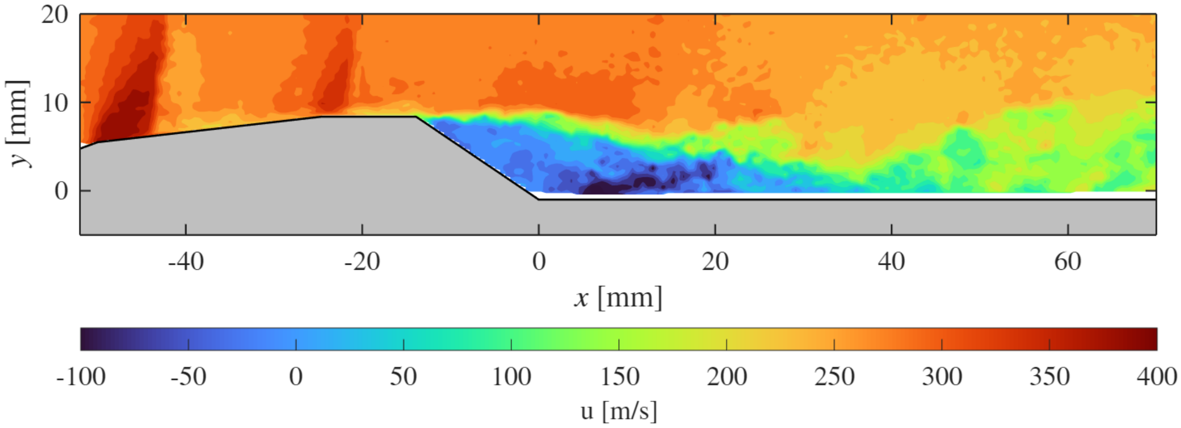

Figure 3.23: Instantaneous velocity field from PIV

was also used for modal analysis. One such velocity field is shown in Figure 3.23; it has been cropped to remove regions with inconsistent seeding in the FoV.

3.6.3 POD

Turbulent flow data is often challenging to interpret due to its inherent complexity. To address this, data-driven techniques—most notably proper orthogonal decomposition (POD)—have been widely used in fluid dynamics, with successful applications to both experimental and numerical datasets for extracting coherent structures in turbulent flows [53]. In this thesis, the PIV dataset is analysed using POD to identify the dominant spatial modes present in the flow field.

Let $u(\vec{x}, t)$ represent the velocity field as a function of both time t and spatial coordinates $\vec{x} = (x, y, z)$. The velocity field can be decomposed into a time-averaged component and a fluctuation component:

$$u(\vec{x}, t) = u_{\text{avg}}(\vec{x}) + u'(\vec{x}, t) = u_{\text{avg}}(\vec{x}) + \sum_{j=1}^{M} a_j(t)\, \phi_j(\vec{x}) \tag{3.42}$$

Here, $\phi_j(\vec{x})$ denotes the spatial POD mode, $a_j(t)$ is the corresponding temporal coefficient, and M is the total number of modes. This spatio-temporal decomposition allows the flow to be expressed as a linear combination of orthogonal modes.

In this thesis, POD is implemented using the Singular Value Decomposition (SVD) method. The fluctuation velocity data on a two-dimensional grid is flattened and arranged such that each column in the data matrix $U \in \mathbb{R}^{N_m \times N_t}$ represents the spatial field at a given timestep. Here, N_m is the number of spatial grid points, and N_t is the number of time snapshots.

The SVD of U is given by:

$$U = \Phi \Sigma A^T \tag{3.43}$$

In this formulation, $\Phi \in \mathbb{R}^{N_m \times N_t}$ contains the spatial POD modes in its columns, $\Sigma \in \mathbb{R}^{N_t \times N_t}$ is a diagonal matrix of singular values σ_j sorted in descending order, and $A \in \mathbb{R}^{N_t \times N_t}$ contains the time coefficients in its columns. The spatial mode matrix Φ is constructed by placing the left singular vectors of U (i.e., the eigenvectors of UU^T) in descending order of their associated singular values. Similarly, the matrix A is formed by placing the right singular vectors of U (i.e., the eigenvectors of $U^T U$) in the same descending order.

The energy content of each mode is proportional to the square of its corresponding singular value:

$$E_j = \sigma_j^2 \tag{3.44}$$

This energy ranking allows for dimensionality reduction by retaining only the dominant modes, which capture the most significant features of the flow. The temporal coefficients stored in the columns of A describe how each spatial mode evolves in the dataset.

POD may also be used to reconstruct the velocity field using only a subset of the most dominant modes, thereby realising a reduced order model. For a snapshot at time step i, when M is the number of modes used for the lower rank approximation, the reconstruction is given by:

$$u_{\text{recon}}(\vec{x}, t_i) = u_{\text{avg}}(\vec{x}) + \sum_{j=1}^{M} \sigma_j \, A_{ij} \, \phi_j(\vec{x}) \tag{3.45}$$

3.6.4 SPOD

Spectral Proper Orthogonal Decomposition (SPOD) is an extension of classical POD that incorporates spectral information to extract coherent structures. These structures are both energetic and temporally correlated at specific frequencies. While classical POD treats all time snapshots equally, SPOD leverages the temporal coherence by applying POD to Fourier-transformed data.

The construction of the data matrix is similar to POD, but rather than performing DFT on the whole dataset, it is segmented into overlapping windows and DFT is performed over these blocks and averaged to produce the DFT. Though this process reduces the resolution, it better handles noise. POD is then applied independently at each frequency, leading to frequency-dependent modes and their corresponding energies being extracted. This allows the decomposition to isolate the spatial modes that oscillate at well-defined frequencies, making it particularly useful for statistically stationary flows [60].

The decomposition takes the form:

$$\hat{u}(\vec{x}, f) = \sum_{j=1}^{M} \beta_j(f)\, \psi_j(\vec{x}, f) \tag{3.46}$$

Here, $\hat{u}(\vec{x}, f)$ is the Fourier-transformed fluctuating velocity field at frequency f, $\psi_j(\vec{x}, f)$ denotes the spatial SPOD mode at frequency f, and $\beta_j(f)$ is its corresponding complex amplitude. SPOD enables a frequency-by-frequency analysis of flow dynamics, making it an ideal tool for studying periodic or quasi-periodic phenomena such as vortex shedding, shockwave oscillation, tonal noise generation, and coherent wavepacket evolution.

Multiple parameters affect the output of SPOD, which includes the number of blocks and sampling frequency. The number of blocks is affected by the number of samples per block, the overlap percentage and the total number of samples in the dataset. In this thesis, 29116 schlieren images, sampled at a frequency of 25 kHz, were segmented into 27 blocks containing 2048 samples per block with a 50% overlap. This inherently restricts the frequency resolution Δf to 12.2 Hz:

$$\Delta f = \frac{f_s/2}{\frac{N_b}{2}+1} = \frac{25000/2}{\frac{2048}{2}+1} = 12.2Hz \tag{3.47}$$

where f_s is the sampling frequency and N_b is the number of samples per block. The corresponding resolution in terms of Strouhal number with respect to step height is provided in Table 3.5. With this block size, 1025 frequency bins are resolved over the range 0 to 25,000 Hz, in accordance with the Nyquist criterion.

Mach	ΔSt_h
0.6	0.0006
0.7	0.0005
0.8	0.0004

Table 3.5: Resolution of SPOD analysis in terms of St_h

4

Results and Discussions

This chapter presents and analyses the results obtained from the experimental campaigns. The discussion begins with an overview of the general flow field over Model 11 at $M = 0.8$, as observed in the present study, and a comparison with reference data from the literature to provide validation. The influence of the boattail radius on the flow is then examined, with particular emphasis on the variation of reattachment length. In addition, the effects of Mach number and angle of attack are briefly addressed to highlight their role in shaping the flow behaviour.

The subsequent sections focus on the dynamics of the shock system for both the base (Model 11) and the radius-modified configurations, providing insight into the mechanisms governing their unsteadiness. Finally, the chapter explores the dominant spatial modes extracted from the data in Section 4.6, followed by an analysis of their spectral content in Section 4.7.

4.1 General Flow Field

This section presents the general flow field over Model 11 at Mach 0.8, which forms the foundation for further analysis in subsequent sections. Figure 4.1 displays a representative schlieren image that reveals the primary flow structures around the Model 11 HHF. The most prominent features observed include: (i) two shock waves originating over the PLF, (ii) expansion regions preceding these shocks, and (iii) a separated flow region aft of the boattail.

Model 11 consists of two conical segments connected in series, producing two geometric junctions between the first and second cone (referred to as the *biconic junction*), and between the second cone and the cylindrical section (referred to as the *cone-cylinder junction*). At both these junctions, the flow encounters a local increase in cross-sectional area, resulting in expansion fans that are clearly visible in the schlieren image. The flow is accelerated to supersonic speeds through these expansion regions and subsequently terminated by a normal shock wave. Downstream of the cone-cylinder junction, due to the sharp change in geometry, the flow separates at the boattail edge, generating a shear layer. This shear layer ultimately reattaches further downstream, enclosing a recirculation region that characterises the separated flow behind the boattail.

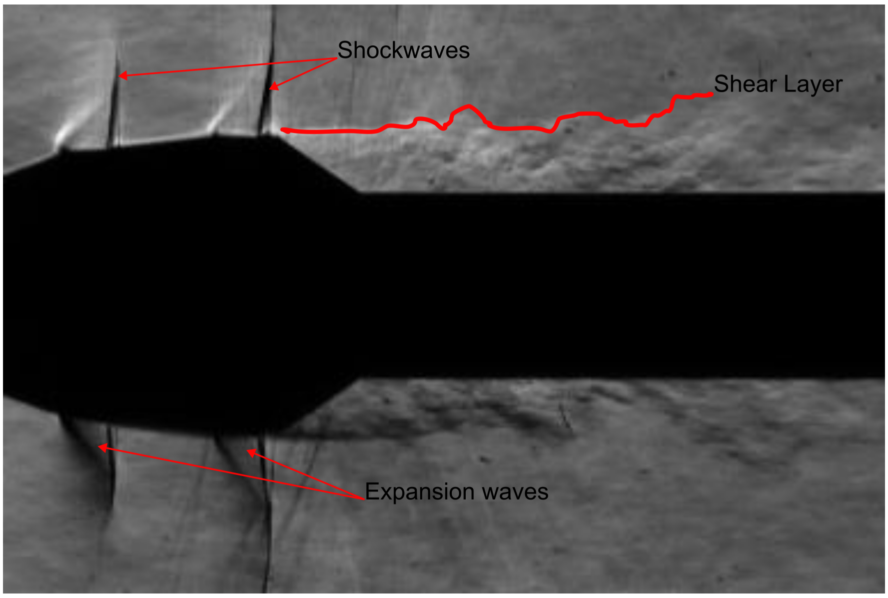

Figure 4.1: Schlieren image showing the general flow features at M = 0.8

Figure 4.2, which shows the mean horizontal velocity component ($\bar{u}$) superimposed with mean streamlines, provides deeper insight into the flow field at $M = 0.8$. Velocities exceeding the speed of sound, with peak values of approximately 370 m/s and 340 m/s in the first and second expansion regions, respectively, are observed downstream of the bi-conic and cone-cylinder junctions. The shock waves that terminate these supersonic pockets are not sharply defined in the mean velocity field, indicating their unsteady nature. Flow separation occurs at the boattail edge, forming a prominent recirculation region characterised by reversed flow. Within this zone, the flow reaches a maximum reversed velocity of approximately 70 m/s. The shear layer reattaches further downstream and remains attached as the flow gradually recovers pressure.

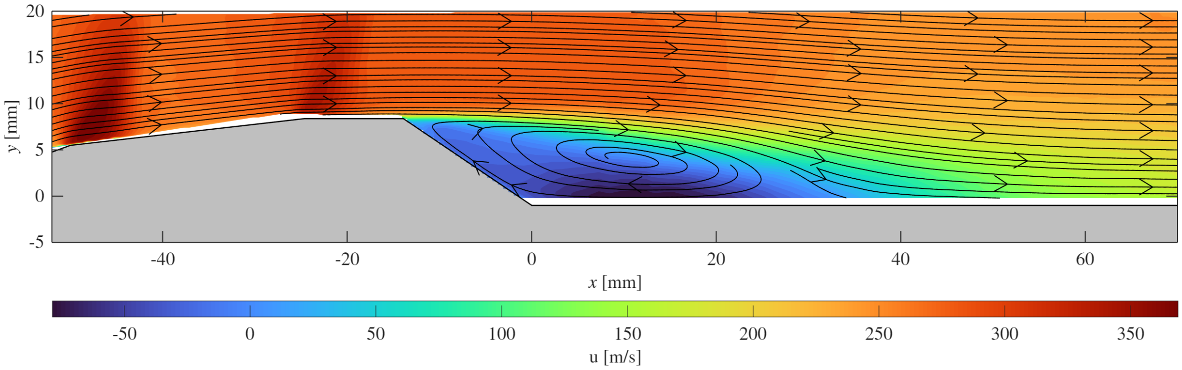

Figure 4.2: PIV mean horizontal velocity field at M = 0.8 with streamlines superimposed

The mean shock locations and separation characteristics can be inferred from the surface oil flow patterns. Figure 4.3 shows the oil flow visualisation over Model 11 at $M = 0.8$. One of

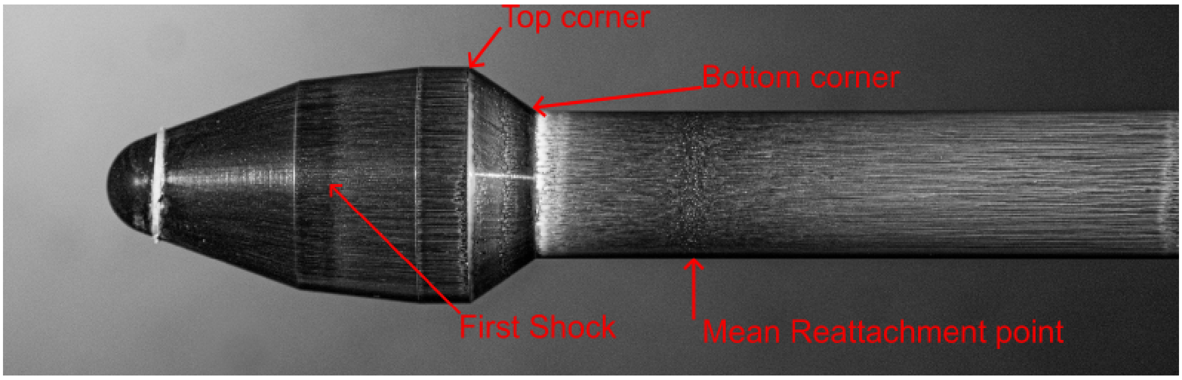

Figure 4.3: Oil flow pattern over the R0 case at M = 0.8

the most prominent features is the first shock wave immediately downstream of the bi-conic junction, identifiable by a sudden accumulation of oil. This is caused by a local pressure rise, leading to an abrupt deceleration of the boundary layer and oil stagnation. The first shock is located at a distance of $0.954D$ from the nose of the model, where $D = 50$ mm is the diameter of the cylindrical section of the HHF. While traces of the second shock are visible near the boattail edge, it is much less defined than the first shock.

Beyond the boattail, a separated flow region forms, characterised by recirculation. The reattachment point is inferred from a zone where the oil streaklines appear anchored, with streaks fanning outward in both directions. The smeared appearance of this region suggests an unsteady reattachment location that varies over time. Flow recirculation is evident from the upward-swept oil pattern on the boattail and the significant accumulation of oil at its bottom edge. The mean reattachment location, measured from the boattail top corner, is about $5.1h$, where h is the boattail step height. In the Figure 4.2, the mean reattachment is at the $x = 31mm$ mark.

A particularly interesting observation emerges near the cone-cylinder junction. Just downstream of it, a small patch of oil accumulation is visible before being swept downstream. This swept-away pattern indicates a localised acceleration of the flow—characteristic of an expansion region, where the increase in velocity causes the oil to be rapidly displaced, leaving a cleaner surface. The localised oil build-up prior to this region is indicative of a possible small-scale separation bubble, which may not be readily discernible in schlieren or PIV imagery but is suggested by the oil flow visualisation.

The shock waves and separation region exhibit a highly oscillatory nature, as illustrated by the schlieren images at different time steps in Figure 4.4. These images are spaced 6 ms apart and clearly demonstrate the unsteady behaviour of both shocks. Additionally, the varying shape of the shear layer across the frames further indicates the presence of unsteadiness in the separated region.

To better visualise this unsteadiness, the standard deviation of pixel intensities across the schlieren image sequence is computed. Regions with high standard deviation values correspond to areas of significant unsteady motion. Figure 4.5 shows the standard deviation field

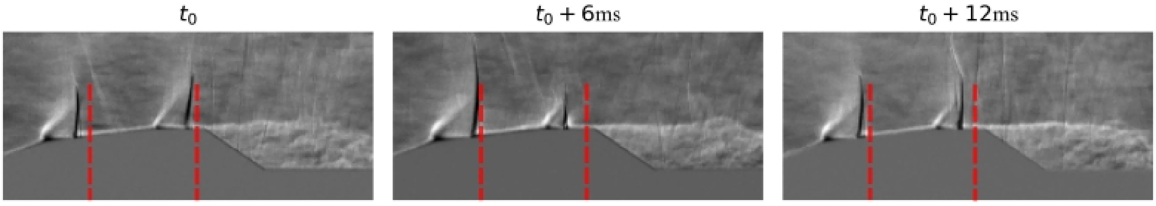

Figure 4.4: Instantaneous images showing shock movement. The red lines indicate the most downstream positions of the corresponding shocks.

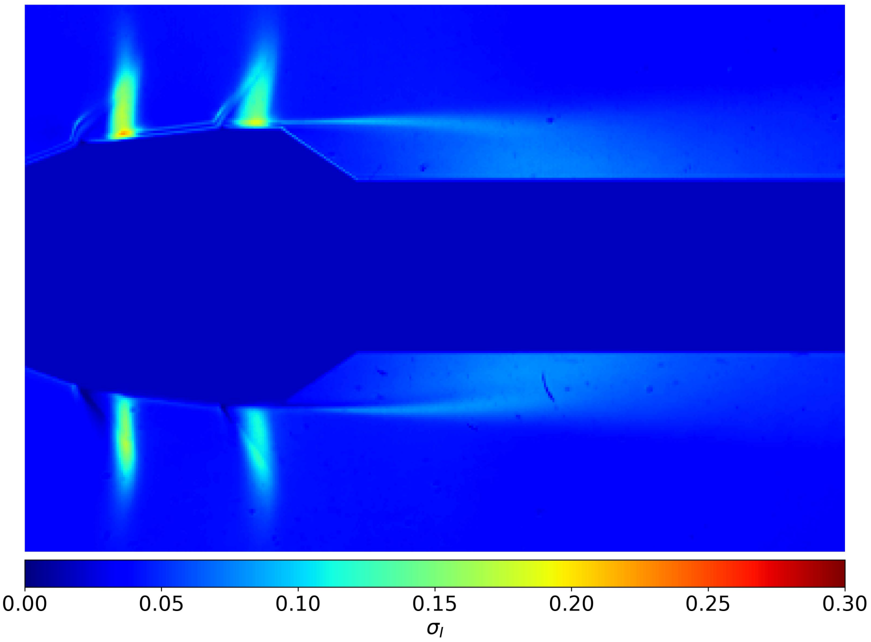

Figure 4.5: Standard deviation of Schlieren image at M = 0.8

at Mach 0.8, where the slight asymmetry between the upper and lower shock structures is attributed to the schlieren knife edge not being positioned at exactly 50% blockage, rather than to any physical asymmetry in the flow. This plot highlights the intense unsteadiness present in both the shock system and the separated shear layer. Higher standard deviation values in the separation region are also an indication that the reattachment location oscillates.

The standard deviation of the horizontal velocity component obtained from PIV measurements, shown in Figure 4.6, reveals elevated RMS values within the shear layer and separation region. While schlieren-based standard deviation images also indicate unsteady behaviour in these regions, the magnitudes are notably lower compared to those observed near the shock waves. This apparent discrepancy arises from the fundamental differences in the physical quantities visualised by each method. PIV measures the velocity components of the flow, providing a more quantitative assessment of momentum fluctuations. In contrast, schlieren visualisations represent the integrated deflection of light rays due to refractive index gradients along the optical path. As a result, three-dimensional effects and out-of-plane gradients may contaminate the schlieren signal, reducing its sensitivity in regions of weak density variation. Moreover, the flow velocity in the separation region is significantly lower, leading to diminished compressibility effects. This further limits the effectiveness of schlieren imaging in capturing unsteadiness within low-speed separated zones. While the unsteadiness is concentrated in both the shocks and shear layer, the Reynolds shear stress($-u'v'$) distribution at M = 0.8, shown in Figure 4.7, indicates turbulence production to be concentrated in the shear layer, with peaks in turbulence production noticed near the mean reattachment location.

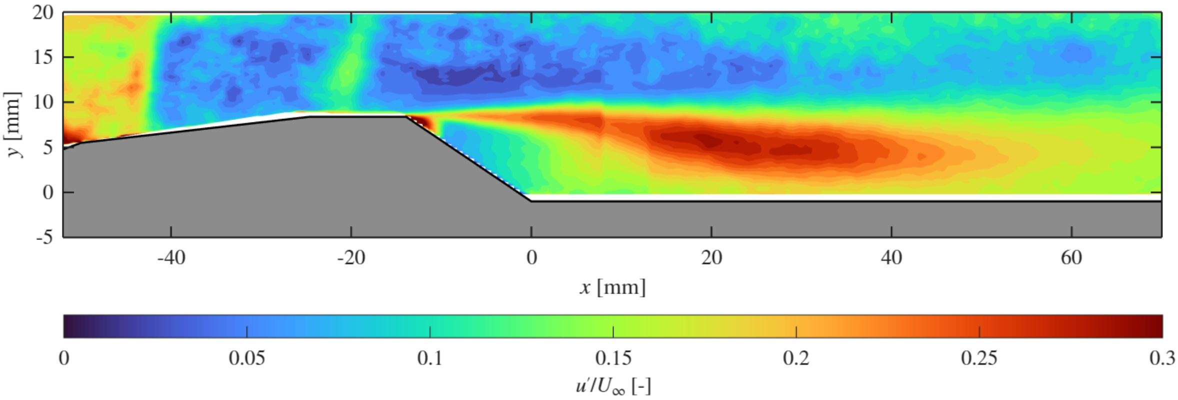

Figure 4.6: Standard deviation of horizontal velocity at M = 0.8

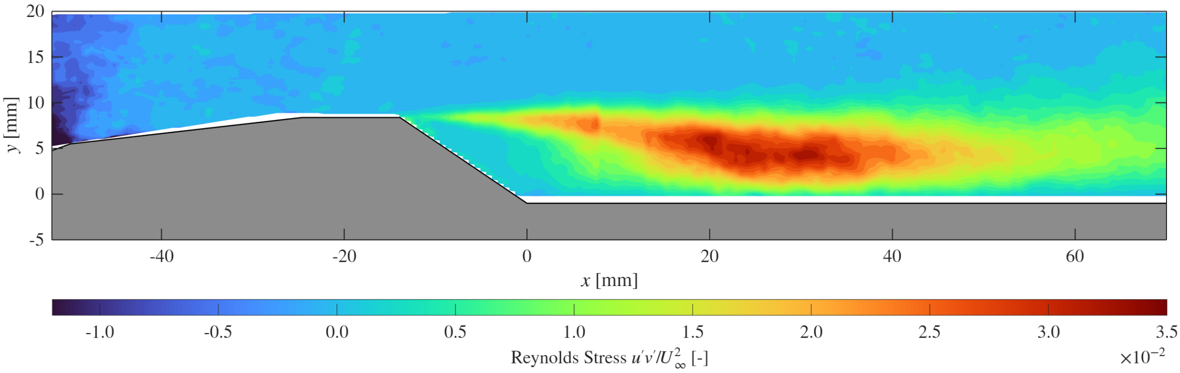

Figure 4.7: Reynolds shear stress at M = 0.8

Comparison with Literature

To validate the results, a brief comparison is made with data available in the literature. Specifically, the Model 11 test data from Romero [49] and the experiments by Panda et al. [42] are used for this purpose. Instantaneous schlieren images from these sources are shown in Figure 4.8, which includes Mach numbers $M = 0.8$ and $M = 0.85$ from Panda et al., $M = 0.8$ image from Romero's dataset and $M = 0.8$ image from the current study. Interestingly, the schlieren image at $M = 0.85$ from Panda et al. resembles the $M = 0.8$ images from Romero and the current study. As discussed by Romero [49], this agreement is likely a consequence of blockage effects in the TST-27 facility [18, 63], as further detailed in Section 3.3.1 and Appendix A.

The reattachment location, measured from the top of the boattail corner, is $5.1h$, where h is the boattail step height. Gentile [**gentile_symmetry_nodate**] reported a reattachment

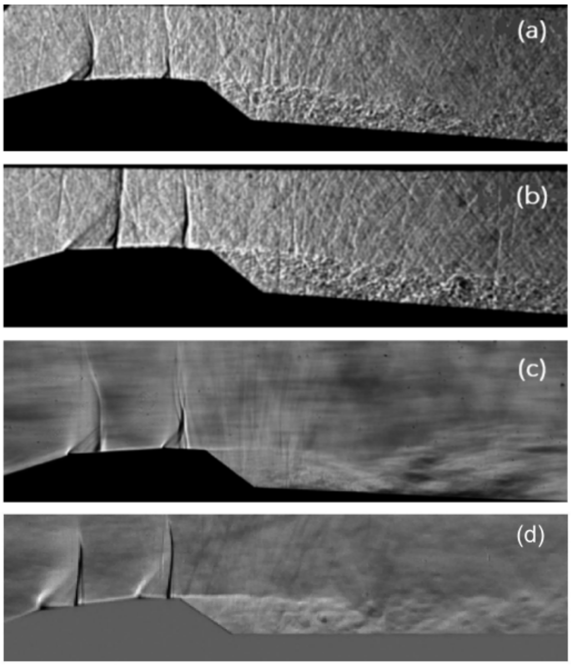

Figure 4.8: Instantaneous Schlieren images from (a) Panda et al. at $M = 0.8$, (b) Panda et al. at $M = 0.85$ [42], (c) Romero at $M = 0.8$ [49], and (d) current study at $M = 0.8$.

length of $4.1h$ for a d/D ratio of 0.6 at low subsonic speeds. Model 11, with a similar d/D ratio of 0.625, exhibits a more downstream reattachment point at $5.1h$, likely due to the higher flow speed. Other studies on BFS flows have reported shorter reattachment lengths: Kähler and Scharnowski [51] measured $3.5h$ at $M = 0.7$, Thoringy and Deck [21] reported $3.6h$, and Schrijer et al. [55] observed $3.0h$. The longer reattachment length of $5.1h$ obtained for Model 11 may be attributed to the interaction of the separated shear layer with the second shock. It should also be noted that the models used in the latter three studies had a d/D ratio of 0.4, which influences the reattachment location.

A key difference between Romero's schlieren data (Figure 4.8(c)) and the present results (Figure 4.8(d)) is the presence of motion blur in Romero's image. This arises from the lower shutter speed of 1/20,000 s used in Romero's experiment, compared with the higher shutter speed of 1/100,000 s employed in the present study. The shorter exposure time yields a sharper visualisation of the shock structures. This influence of shutter speed is also evident in the standard deviation fields: the RMS values in Romero's results (Figure 4.10(c)) are noticeably higher than those obtained in the current study (Figure 4.9). This discrepancy can be attributed to the blurred shock features in Romero's data, which artificially enhance pixel intensity fluctuations during the statistical analysis.

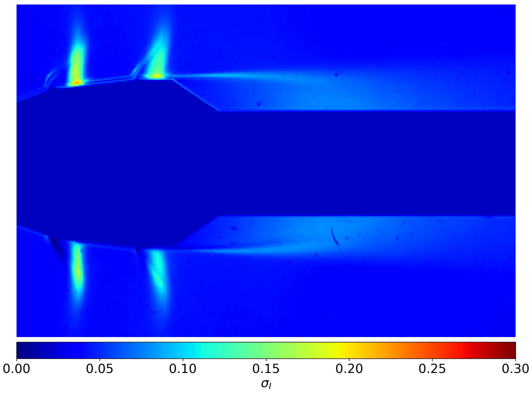

Figure 4.9: Pixel intensity standard deviation at $M = 0.8$ from the present study.

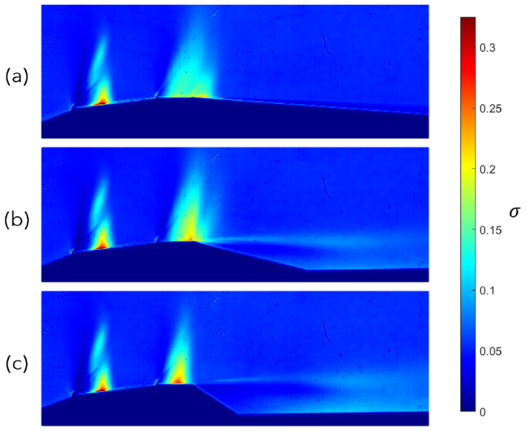

Figure 4.10: Pixel intensity standard deviation at $M = 0.8$ for boattail angles (a) $5°$, (b) $15°$, and (c) $34°$, from Romero [49].

4.2 Radius effects

To investigate the effect of boattail radius on the flow field, five boattail geometries with different radii were manufactured, as described in Section 3.3. The radii were selected based on a turbulent boundary layer analysis using the reference temperature method and were chosen to provide a well-distributed range of R/δ values. The five radii considered are: 3 mm, 6 mm, 10 mm, 15 mm, and 20 mm; and are referred to as R3, R6, R10, R15, and R20 respectively. The base Model 11 is referred to as R0.

Figure 4.11 presents instantaneous schlieren images for all five configurations, along with the baseline (no-radius) configuration at $M = 0.8$. As observed, the boattail radius promotes the formation of a third expansion region, which is subsequently terminated by a shock. The specific frames shown in Figure 4.11 were selected based on the distinct visibility of this third shock structure. After the second shock wave, the flow expands into another supersonic pocket over the boattail curvature, which is subsequently terminated by a shock wave, such that the introduction of a boattail radius promotes the formation of a third expansion–shock pair.

The frequency of occurrence of the third shock and the range of its oscillation can be examined by looking at the standard deviation plots of the schlieren images shown in Figure 4.12. The third shock is more visible from the R6 case, and its size and oscillation range increase with radius. The first shock, as expected, is unaffected by the introduction of radius; however, the second shock shows noticeable changes in its RMS values with the occurrence of a third shock. With an increase in radius, the range of oscillation for the second shock also increases, sometimes merging with the third shock. This increase in range is also attributed to the way the boattail radius is introduced in the test model. As detailed in Section 3.3, the boattail radius is not an edge fillet, but rather an extension.

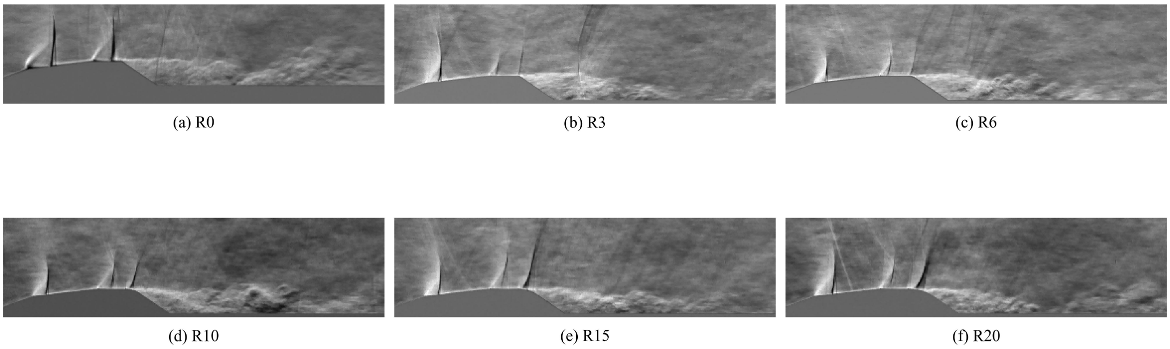

(a) R0 (b) R3 (c) R6

(d) R10 (e) R15 (f) R20

Figure 4.11: Instantaneous schlieren images across all radii configurations at $M = 0.8$

The slight change in the RMS values of the base case with the radius cases is purely due to minor variations in the knife-edge positions.

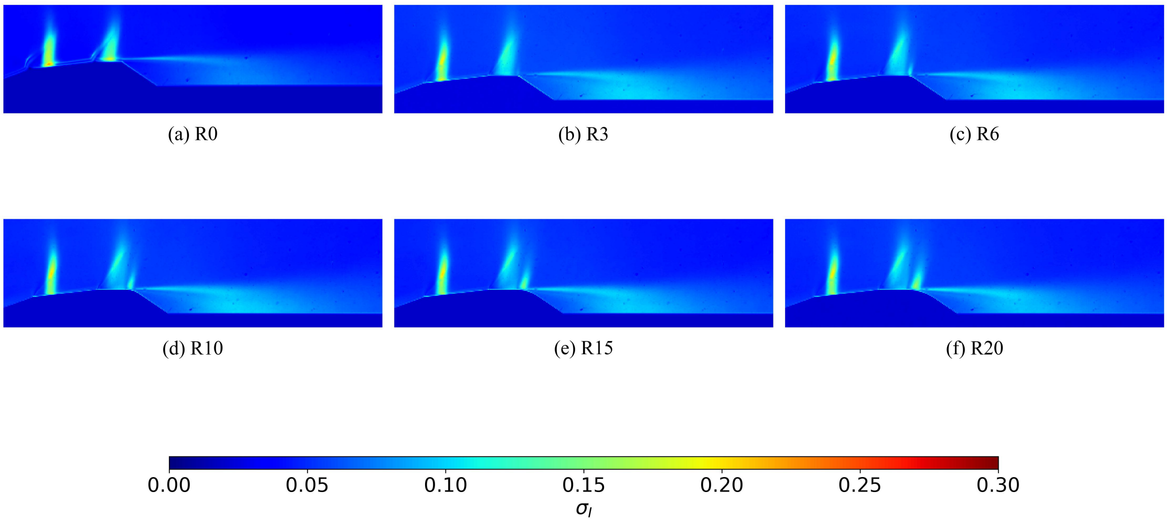

(a) R0 (b) R3 (c) R6

(d) R10 (e) R15 (f) R20

Figure 4.12: Pixel intensity standard deviation plots of all radii configurations at $M = 0.8$

An interesting observation can be made by examining the R3 configuration in both Figures 4.11 and 4.12. The fact that an R/δ value of 1.745 is sufficient to generate a third expansion–shock system provides a reverse indication that the boundary layer thickness at the boattail edge is on the order of 3 mm, since the flow is able to sense and respond to geometric curvature at that scale. However, the third shock is typically weak and rarely observed. Its presence is more likely when the second shock is located upstream. A plausible explanation is that as the second shock strengthens, it thickens the boundary layer at its foot, preventing the flow from conforming to the 3 mm curvature and thereby suppressing the formation of the third expansion region.

A similar trend is observed in the R6 configuration, as shown in Figure 4.13. The figure displays both the upstream position of the second shock—where the third shock appears—and the downstream position, where it is absent. While the third shock remains weak in the R6 case, it occurs more frequently than in the R3 configuration. Since both cases exhibit

(a) R0 - upstream (b) R0 - upstream

(c) R3 - upstream (d) R3 - upstream

(e) R6 - upstream (f) R6 - upstream

Figure 4.13: Configurations showcasing weak radius effects at $M = 0.8$

comparable flow behaviour, they are classified as exhibiting *weak radius effects*.

Starting from the R10 configuration, the third shock becomes more prominent and begins to significantly influence the overall flow field. Figure 4.14 shows instantaneous schlieren images for the R10, R15, and R20 boattail configurations, both with and without the presence of the third shock. In all three cases, a distinct third expansion region forms over the curved section of the boattail. The associated shocks grow in size with increasing radius and interact with the boundary layer, leading to shock-induced separation. Owing to the strong influence of the third shock on separation dynamics, these configurations are classified as exhibiting *strong radius effects*. However, it is important to note that shock-induced separation occurs only when the third shock is present. As is also evident from Figure 4.14, in the absence of the third shock, flow separation is driven primarily by the geometrical change. More detailed discussion on the dynamics of the third shock is provided in Section 4.5.2.

Based on the preliminary schlieren results, only the most representative configurations are selected for detailed analysis. The base case, as the name suggests, serves as a reference for comparison with boattail configurations featuring various radii. The R3 and R6 cases, which exhibit only weak radius effects, are excluded from further discussion. However, the R3 configuration is retained for oil flow visualisation studies aimed at evaluating changes in separation length. Among the three configurations that demonstrate strong radius effects, only the R10 and R20 cases are carried forward. The R15 case is excluded as it displays flow characteristics similar to the R10 and R20 cases, but with intermediate shock strength and separation features. The R10 configuration is particularly important as it marks the onset of SWBLI at the separation point, while the R20 case is selected for its representation of the most extreme flow conditions within the tested range. Thus, a major portion of the following

(a) R10 - Third shock (b) R10 - No Thrid shock

(c) R15 - Third shock (d) R15 - No Thrid shock

(e) R20 - Third shock (f) R20 - No Thrid shock

Figure 4.14: Configurations showcasing strong radius effects at $M = 0.8$

analysis will only focus on the R0, R10 and R20 cases.

4.2.1 Oil flow pattern

The mean reattachment locations for the base configuration, as well as for the R3, R10, and R20 boattail radius cases, were determined from surface oil flow visualisation. In addition to providing information about the location of the shocks and mean reattachment points, these experiments also offer insights into key flow features that evade observation in other flow diagnostic techniques. Figure 4.15(c) shows the oil flow pattern for the R10 case at $M = 0.8$. The irregular streaks observed over the nose region are due to the cooling of the model after repeated runs, which causes the oil to become more sticky to the surface and less prone to being swept away by the flow.

A comparison with the base case (Figure 4.15(a)) reveals that flow features over PLF remain consistent between the two configurations. The base case exhibits significantly lower oil accumulation near the boattail, indicating weaker separation activity in that region. In contrast, the R10 case shows distinct oil streaks along the boattail curvature, suggesting that the boundary layer remains attached for a short distance, following the curvature as the flow expands. This expansion is then terminated by a shock, which induces separation. The heavy oil accumulation at the shock location may also be indicative of a localised separation bubble forming at the shock foot, a feature not easily captured in schlieren or PIV diagnostics. The presence of this separation bubble is further discussed in Section 4.5.2.

The R20 case also shows similar flow structures, with the longer attached flow over the curvature, and larger oil accumulation near the separation location, further adding to the claim that these configurations experience strong radius effects.

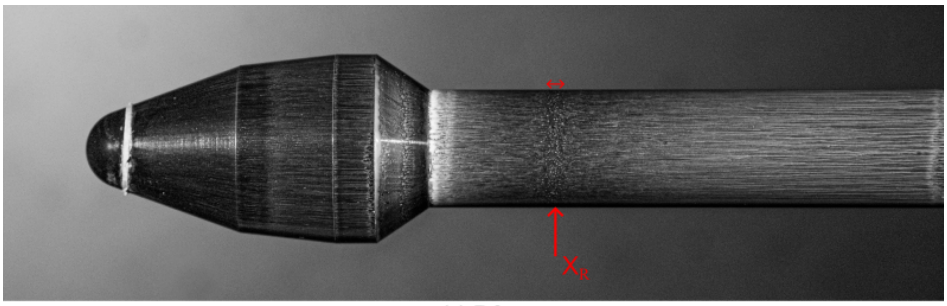

(a) R0

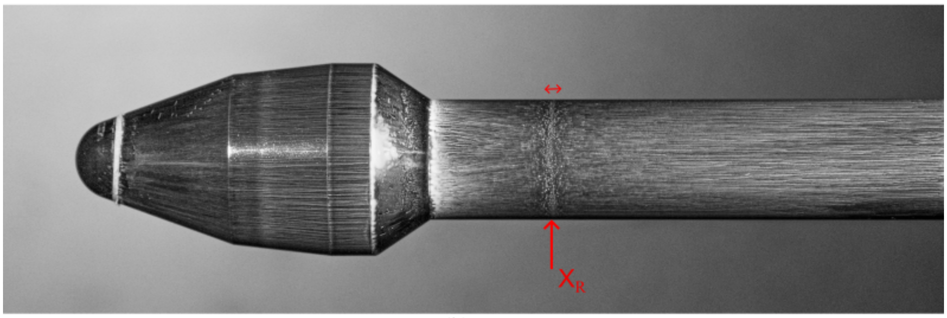

(b) R3

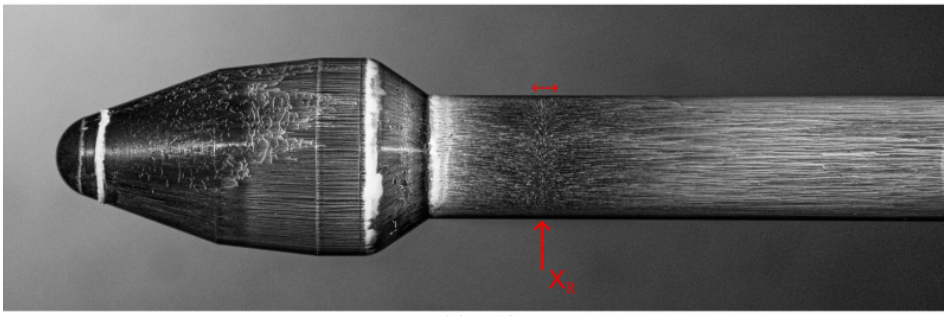

(c) R10

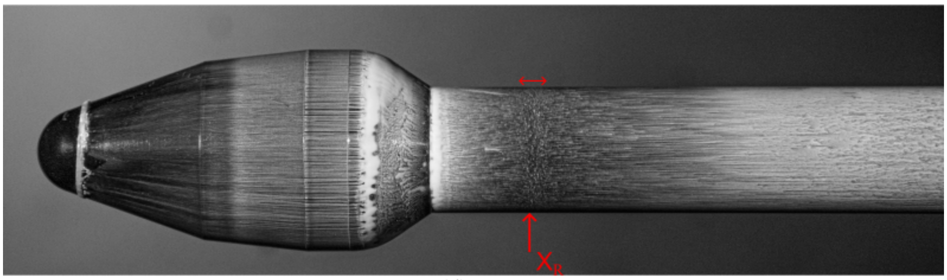

(d) R20

Figure 4.15: Effect of radius of mean reattachment point at $M = 0.8$

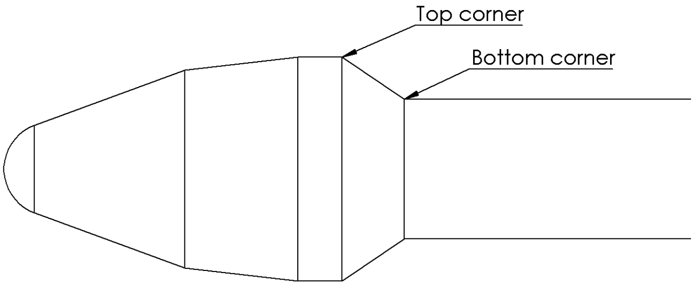

Figure 4.16: Definition of boattail corners on the base case.

4.2.2 Reattachment location

One of the key sub-research questions in this study is to evaluate the effect of boattail radius on the separation length. To address this, the mean reattachment location is determined from surface oil flow visualisation. As previously discussed, the reattachment region is inherently unsteady and spatially distributed. Therefore, the midpoint of the observable reattachment zone is taken as the representative mean reattachment location.

To this end, two reference corners of the boattail are defined in Figure 4.16. Since the radius models were constructed as extensions of the base model, they can be aligned either with the top corner or with the bottom corner in order to establish a consistent reference for measuring the reattachment location. The implications of these two alignment approaches are shown in Figure 4.17, where representative separation locations are indicated by the red circles. As noted earlier, separation on the radius models occurs over the curved section rather than at a sharp corner, and it should be emphasised that the red markers only provide an indicative representation of the separation location for the radius models, rather than an exact position. If the top corner is used as the alignment reference, an artificial progressive increase in the measured reattachment length arises with increasing radius, as the effective separation location shifts further downstream relative to the reference point. In contrast, when the bottom corner is used as the reference, the separation location of the radius models remains much closer to that of the base case, and the relative offset does not grow significantly with increasing radius. For this reason, the bottom corner alignment is adopted in the present study and is used as the origin for PIV measurements.

The reattachment length, X_R, is defined as the distance between the mean reattachment point and the bottom corner of the boattail. Additionally, the position of the first shock wave, denoted as X_{SW1}, is measured from the model nose. Both X_R and X_{SW1} are non-dimensionalised using the boattail step height, $h = 9.375\,\mathrm{mm}$.

Figure 4.18 illustrates the influence of boattail radius on the reattachment length, X_R, and the location of the first shock, X_{SW1}, for the configurations investigated. As expected, the position of the first shock remains nearly constant across all cases, at around $5h$, with a

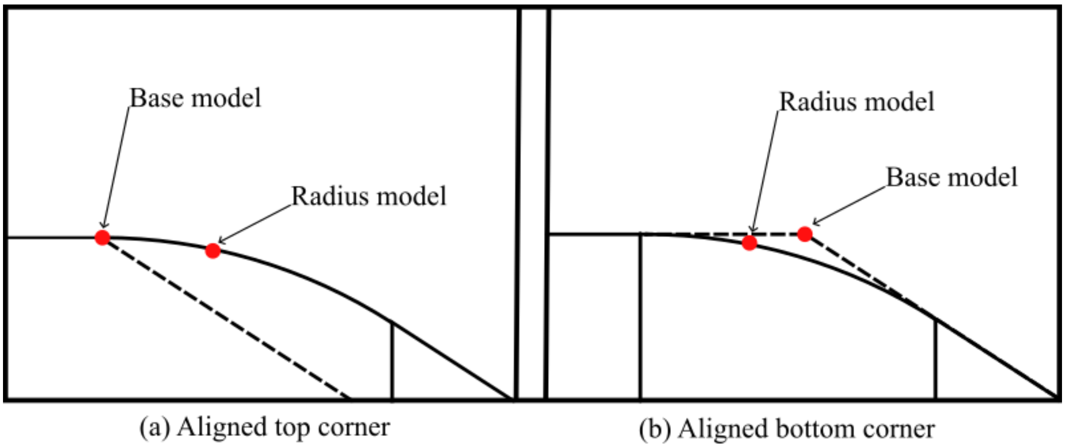

(a) Aligned top corner (b) Aligned bottom corner

Figure 4.17: Schematic illustrating the alignment of the base and radius models. Representative separation locations are marked in red.

Case	Mach	X_R	X_R/h
R0	0.7	27.3	2.9
R0	0.8	31	3.3
R10	0.7	19.6	2.1

Table 4.1: Mean reattachment length extracted from PIV data

maximum variation of approximately $0.1h$ ($\approx 1mm$). This small deviation likely arises from the data extraction process, and thus, the first shock location can be assumed invariant with respect to radius.

The surface oil flow patterns reveal that as a radius is introduced, the flow is able to follow the curvature for a short extent before separating. This results in the shear layer at separation being angled more toward the model body, effectively reducing the separation length. This trend is clearly reflected in Figure 4.18, where a monotonic decrease in X_R is observed with increasing boattail radius. Notably, the R3 configuration shows a reduction in separation length of nearly 10%, suggesting that the flow is indeed sensitive to such a small geometric change. The R10 and R20 cases exhibit even greater reductions, with X_R decreasing by approximately 15% and 25%, respectively, compared to the base configuration.

Looking at the oil flow patterns, shown in Figure 4.15, the reattachment location appears more smeared in the R20 case than the R3 case, hinting that the unsteadiness in the separation region increases with the radius, thereby increasing the range of oscillation of the reattachment point(indicated using the red arrows). This is due to shear layer lifting by the third shockwave, as will be discussed in Section 4.5.2.

The mean reattachment length is also extracted from the PIV results and are tablubalted in Table 4.1. These values are lower than the ones observed from the oil flow data. Since this data is only available for 3 configurations(Mach and radius included), it is not used in the previous analysis.

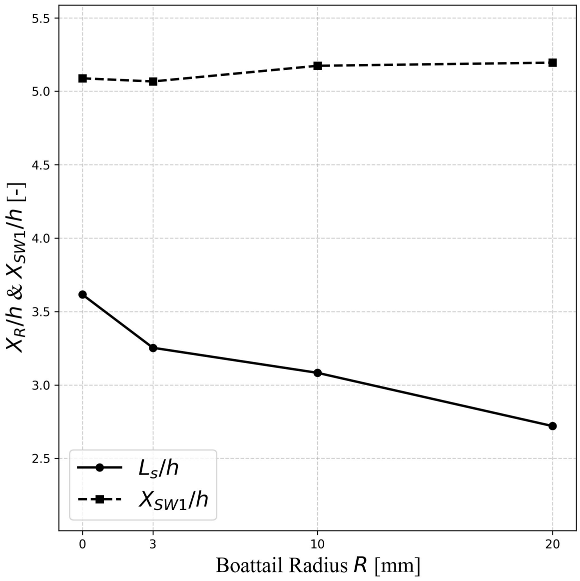

Figure 4.18: First shock and mean reattachment length for various radius cases at $M = 0.8$

4.3 Mach number effect

Figure 4.19 shows schlieren images and their corresponding standard deviation fields for all tested Mach numbers in the R0 case. At $M = 0.6$, no shocks are detected, and the expansion is limited. The corresponding RMS field shows elevated values confined to the separated region downstream, suggesting limited unsteadiness upstream. This may also be linked to weaker compressibility effects at lower Mach numbers, which reduce schlieren sensitivity to subtle disturbances. At $M = 0.7$, a single shock is observed at the bi-conic junction. Although this shock exhibits oscillations, its motion is confined to a narrow range, and the associated expansion region remains smaller compared to the $M = 0.8$ case. Consistently, the RMS intensity in the separation region is concentrated more in upstream regions as the Mach number decreases, indicating progressively shorter separation lengths. This trend is corroborated by the oil flow data, shown later in Figure 4.21.

Figure 4.20 presents the corresponding results for the R10 case at different Mach numbers. The overall trends are consistent with the base case. At $M = 0.6$, only the initial expansion fans at the bi-conic and cone-cylinder junctions are visible, with no discernible shocks. A distinguishing feature of the R10 geometry, however, is the emergence of a third expansion region over the boattail curvature, which reflects stronger curvature-driven acceleration. At $M = 0.7$, a weak shock forms at the bi-conic junction, accompanied by enhanced RMS levels in the third expansion region, implying mild unsteadiness in that zone. At $M = 0.8$, the fully developed three-shock system becomes evident.

Figure 4.21 provides a comparison of the Mach number effect on the reattachment length. In both cases, the separation length increases nearly linearly with Mach number, with the R10 case exhibiting reattachment lengths roughly 15% shorter than R0 across all conditions. This

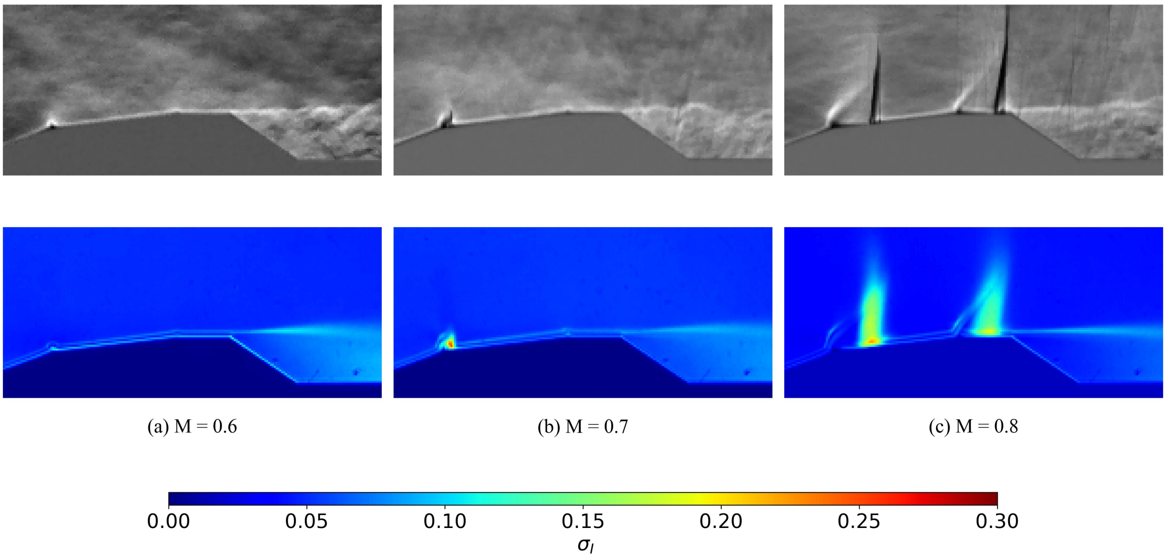

(a) M = 0.6 (b) M = 0.7 (c) M = 0.8

Figure 4.19: Effect of Mach number on the R0 case.

suggests that the reduction in separation length due to the boattail radius is consistent across the Mach numbers investigated, suggesting that Mach number and radius effects act largely independently.

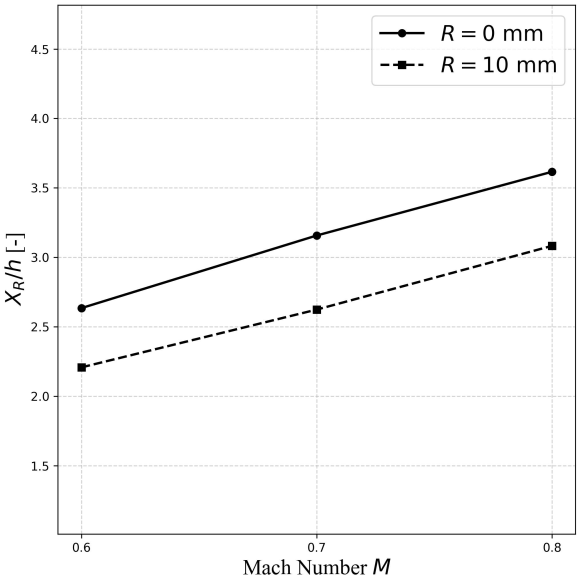

Figure 4.21: Mach number effect on the mean reattachment length on R0 and R10 case

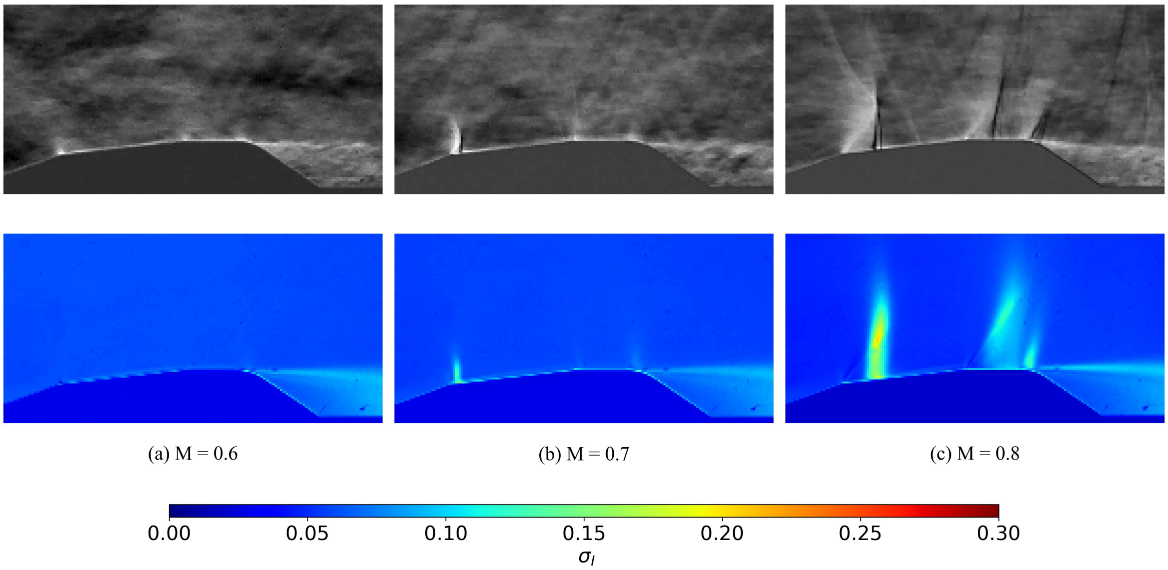
(a) M = 0.6

(b) M = 0.7

(c) M = 0.8

Figure 4.20: Mach number effect on the R10 case

4.4 Angle of Attack effect

To assess the effect of angle of attack (AoA) on the flow field, tests were conducted at an AoA of 4°. This value was selected as it aligns with most prior literature and falls within the typical operational range of launch vehicles, which generally fly at angles between -6° and $+6^\circ$ degrees. Therefore, 4° is considered representative for such conditions.

Figure 4.22 shows the oil flow patterns for the base and R10 boattail radius configurations at $M = 0.8$. The side facing the incoming flow (bottom side in the figure) is referred to as the *windward* side, and the opposite as the *leeward* side. Introducing an angle of attack breaks the symmetry of the flow field, resulting in a tilted shockwave trace, a skewed reattachment location, and upward-bent streaklines near the reattachment zone. In particular, the position of the first shock is altered: in the R10 case, it shifts upstream on the windward side to $4.95h$, and downstream on the leeward side to $5.4h$, relative to its nominal symmetric location of $5.17h$ at 0° AoA. The reattachment region also deviates noticeably. While the 0° AoA cases display nearly straight surface streaklines along the model, the 4° cases exhibit pronounced asymmetry, with streamlines curving upward and the reattachment zone becoming skewed.

These changes are summarised in Figure 4.23. A consistent trend across configurations is evident: the first shock shifts downstream on the leeward side and upstream on the windward side, except for the R3 case. In most configurations, the separation length on the windward side remains close to its 0° counterpart, while the leeward side shows a notable upstream shift. Interestingly, the base case deviates from this trend, showing a similarly reduced reattachment length compared to the 0° case on either side, although the flow patterns appear curved.

A plausible explanation for both phenomena lies in the asymmetric expansion of the incoming

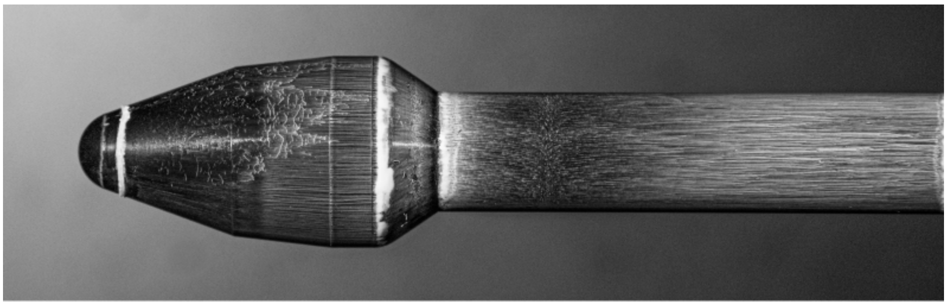

(a) 0° AoA

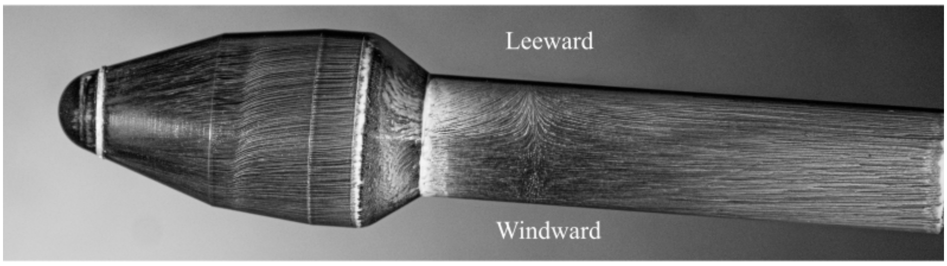

(b) 4° AoA

Figure 4.22: Oil flow patterns on R10 case at M = 0.8

flow. On the leeward side, the bi-conic junction and boattail curvature produce stronger expansion due to the larger geometric deflection (+4°). This enhanced expansion delays shock formation and shifts it downstream. At the same time, the stronger expansion around the boattail postpones flow separation, resulting in a reduced reattachment length. Supporting this interpretation, oil accumulation on the leeward boattail radius is observed slightly downstream of that on the windward side, consistent with delayed separation and reattachment. An additional contributing factor could be asymmetric blockage: on the leeward side, the diverging cross-section reduces velocity, while on the windward side, the converging cross-section increases it. This hypothesis, however, requires verification through PIV measurements on both windward and leeward sides.

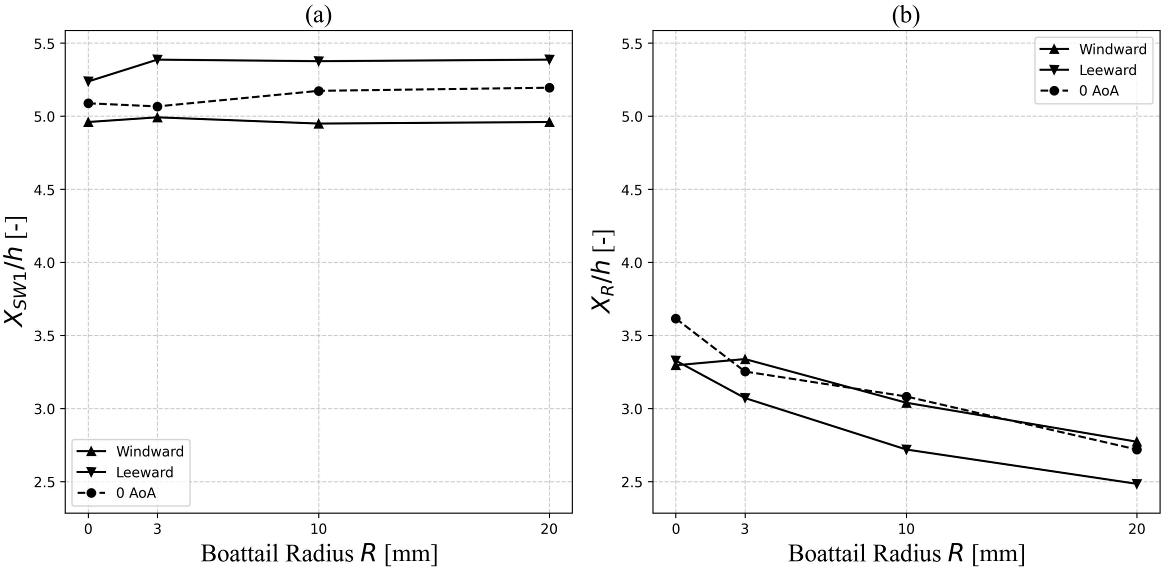

Figure 4.23: Angle of attack effect on (a) First shock location (b) Reattachment length length on R0, R3, R10 and R20 cases at $M = 0.8$

4.5 Dynamics of the Shock System

This section details the dynamics of the shock system in both the base and radius configurations. Examining the instantaneous schlieren images reveals patterns in terms of shock movements and shear layer unsteadiness. When the second shock is located in its downstream position—near the boattail edge—large structures are observed within the separation region, suggesting a more downstream reattachment point. Conversely, when the shock is near its upstream position, the separation region appears more compact. Looking at schlieren videos, it is confirmed that a larger structure is shed whenever the second shock moves downstream. This could be because of the shear layer being lifted at the foot of the shock.

Such coupling between the flow features provides detailed insights into the flow, and also helps in analysing the spatial and temporal modal analysis discussed in later sections.

4.5.1 Model 11

The dynamics of the dual-shock system in the base configuration significantly influence the development and behaviour of the shear layer. Figure 4.24 illustrates instantaneous schlieren images that capture representative shock configurations. The system exhibits a repeatable cyclic interaction between the two shocks, which can be described in the following four phases:

- **Phase 1 – Initial state:**
  The cycle begins with both the first and second shocks located near their most up-

stream positions. The expansion regions at the cone-cylinder and bi-conic junctions are relatively small, and the separation region near the base remains limited in size.

- **Phase 2 – Downstream movement of second shock:**
  As the expansion over the cone–cylinder junction intensifies, the second shock (SW2) begins to shift downstream, while the first shock (SW1) remains essentially stationary. The downstream displacement of SW2 raises the pressure at the separation point, reduces the local velocity, and enlarges the separated region.

- **Phase 3 – First shock follows:**
  SW1 moves downstream, following the earlier shift of SW2, resulting in enlarged expansion regions. The separation zone remains broadly similar to the previous phase.

- **Phase 4 – Upstream movement of second shock:**
  As SW1 reaches its downstream position, the rise in pressure behind it lowers the local velocity, reducing the extent of the expansion over the cone–cylinder junction. Consequently, SW2 rapidly moves upstream.

- **Cycle reset:**
  Finally, SW1 also shifts upstream, returning the system to its original configuration as in Phase 1, thus completing the oscillatory loop.

This cyclic behaviour is also evident in Figure 4.25, which shows the temporal evolution of a single pixel line intersecting both shock waves over the first 1000 frames. While the overall pattern remains consistent, the oscillation cycles vary in both frequency and amplitude over time. The corresponding cross-correlation between the positions of the first and second shocks, together with its Fourier transform, is shown in Figure 4.26. In this analysis, the second-shock signal is taken as the reference and the first-shock signal as the moving signal. A distinct correlation peak is observed at a time delay of approximately 0.56 ms, indicating the time required for a structure associated with the second shock to appear at the location of the first. Approximating the separation between the two shocks as 20 mm yields an upstream convective velocity of about 36 m/s. In comparison, the flow velocity in this region is roughly 270 m/s, while the local speed of sound is about 320 m/s. The estimated upstream convective velocity, therefore, falls within the order of magnitude expected for acoustic-wave propagation, suggesting that the coupling between the two shocks is mediated by acoustic waves. This interpretation is consistent with observations by Panda et al., [42] who reported upstream convection of disturbances over the PLF at velocities in the range $-0.3 \leq U_c/U \leq -0.1$, which compares well with the normalised convective velocity of -0.14 obtained in the present analysis. It was also noted that the upstream propagation of disturbances disappeared for supersonic conditions, further strengthening the argument that the disturbances are acoustic in nature. Finally, the Fourier transform of the correlation signal reveals a dominant frequency at 423 Hz, which will be discussed in Section 4.7.

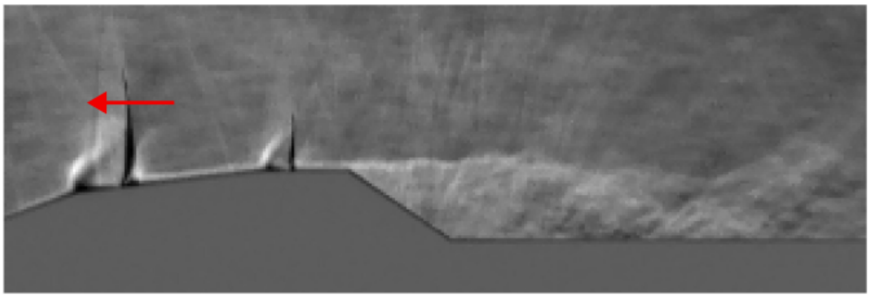

(a) Phase 1

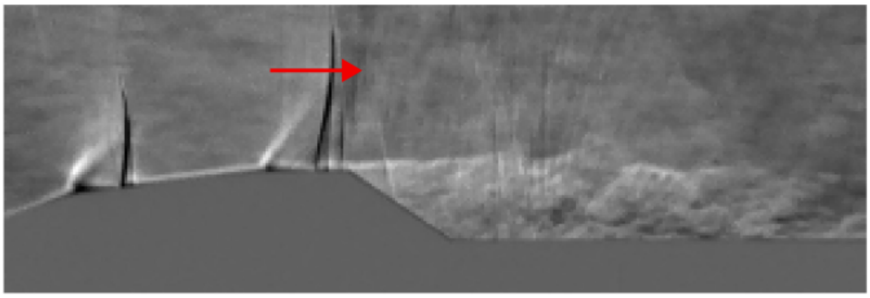

(b) Phase 2

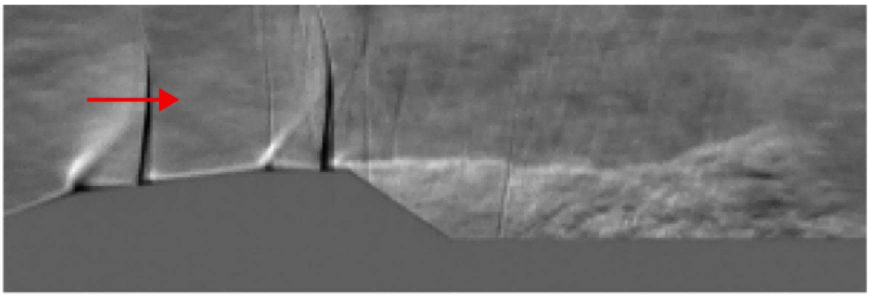

(c) Phase 3

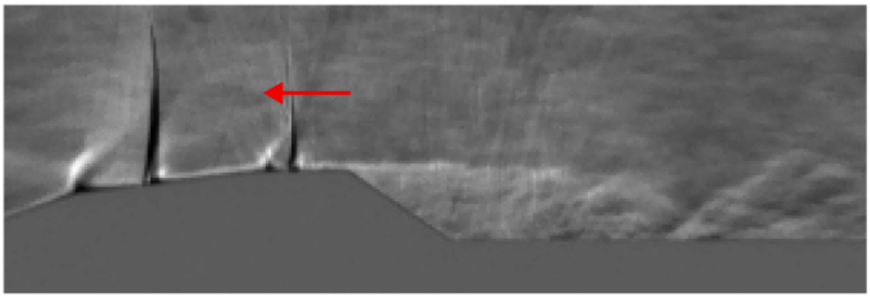

(d) Phase 4

Figure 4.24: Coupling between the shock waves and the shear layer for base case at M = 0.8

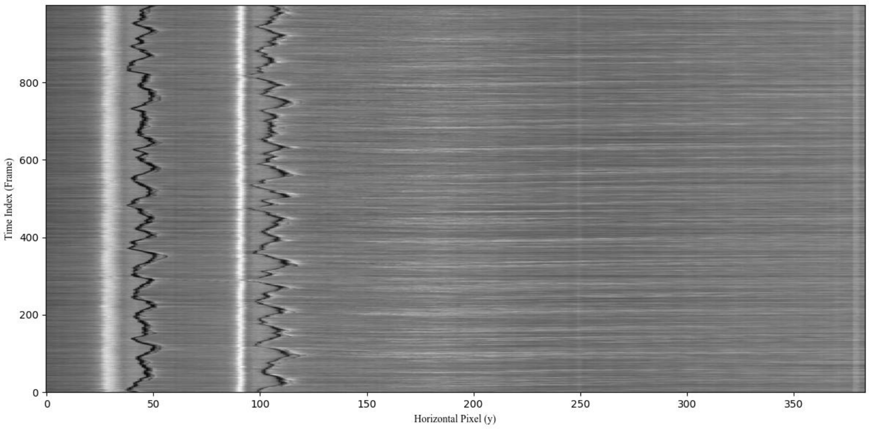

Figure 4.25: Evolution of pixel line containing both the shocks over the first $0.04s$

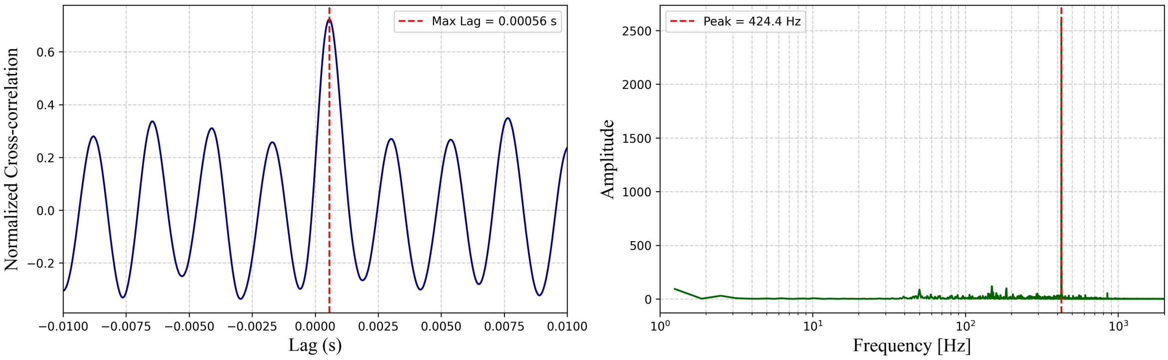

(a) (b)

Figure 4.26: Cross-Correlation between the First and Second shock positions (a) Correlation coefficient (b) FFT of correlation coefficient

4.5.2 Radius effect

The introduction of boattail curvature significantly alters the dynamics of the shock system by introducing a third shock that interacts with the shear layer. While the second shock previously modulated the separation behaviour in the base configuration, the addition of a third shock leads to a more complex coupling mechanism. Figure 4.27 illustrates representative schlieren snapshots that capture this modified interaction. The updated shock dynamics can be characterised as follows:

- **Phase 1 – Initial state:**
  The cycle begins with both the first and second shocks (SW1 and SW2) located near their upstream positions, as in the base case. A third expansion region appears over the boattail curvature. At this stage, the expansion regions are minimal, and the shear layer remains relatively undisturbed.
- **Phase 2 – Growth of third shock and shear layer disturbance:**

SW3 appears and grows in size, interacts with the separated region, and triggers the shedding of a larger structure into the shear layer, indicating stronger coupling between SW3 and the separation region.

- **Phase 3 – Merging of second and third shocks:**
  The presence of a third supersonic pocket reduces the pressure downstream of SW2, triggering it to move downstream. The downstream motion of the second shock limits the expansion over the boattail curvature, forcing SW3 to weaken. Eventually, SW2 and SW3 merge. This merging is intermittent, though sometimes SW3 vanishes without merging.
- **Phase 4 – Collapse of second expansion and upstream motion:**
  A minor downstream shift of SW1 is sufficient to collapse the expansion region at the cone-cylinder junction. This collapse drives SW2 rapidly upstream, while SW3 appears a while later.
- **Cycle reset:**
  SW1 begins to return to its upstream location. The system reverts to a configuration similar to Phase 1, completing the oscillatory sequence.

Refer to Figure C.5 in Appendix C for the temporal evolution of a pixel line containing all three shocks.

SWBLI

Figure 4.28 presents zoomed-in instantaneous schlieren images superimposed on mean oil flow patterns for the R10 and R20 boattail radius configurations at $M = 0.8$, where the third shockwave is most prominent. These images reveal clear signs of strong interaction between the shockwave and the boundary layer. The third shock appears to exhibit a lambda-shock structure—albeit with limited resolution—which is a hallmark of a SWBLI. This interpretation is further supported by the oil flow patterns, which show pronounced oil accumulation along the boattail curvature, indicating a separation bubble at the shock foot, and reinforcing the classification of this interaction as a strong SWBLI.

Additionally, in both images, the shear layer appears to lift immediately downstream of the third shock foot. Within the separation region, a larger structure can also be seen forming. This indicates that the presence of the third shock interacts strongly with the boundary layer, inducing flow separation, elevating the shear layer, and promoting the shedding of larger coherent structures. These dynamics contribute to increased fluctuations in the reattachment location, as already shown in Section 4.2.2.

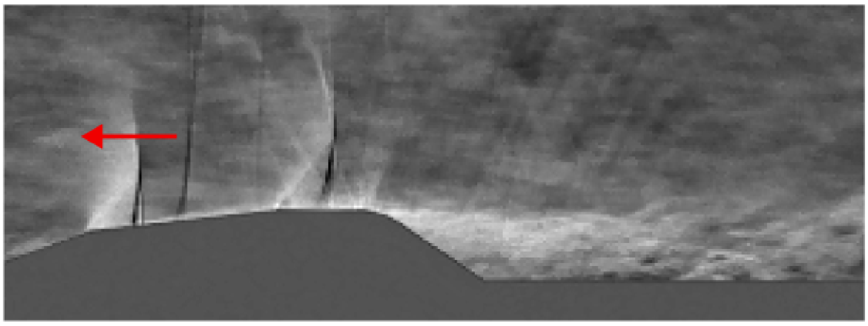

(a) Phase 1

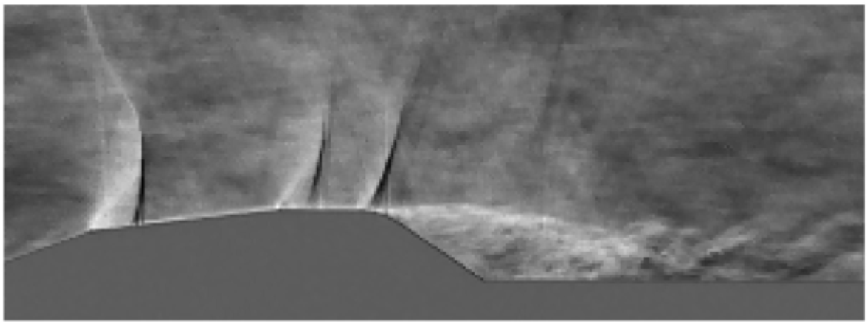

(b) Phase 2

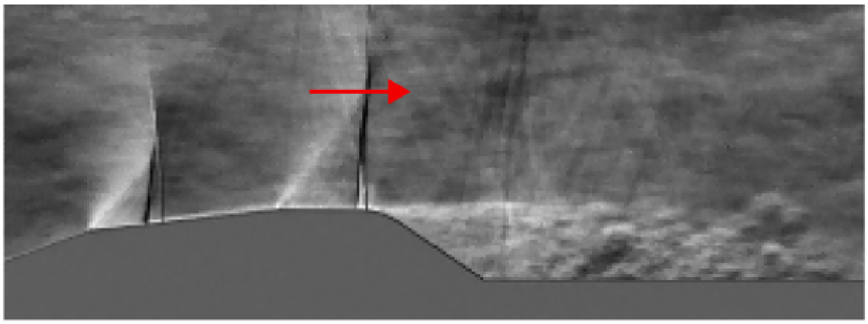

(c) Phase 3

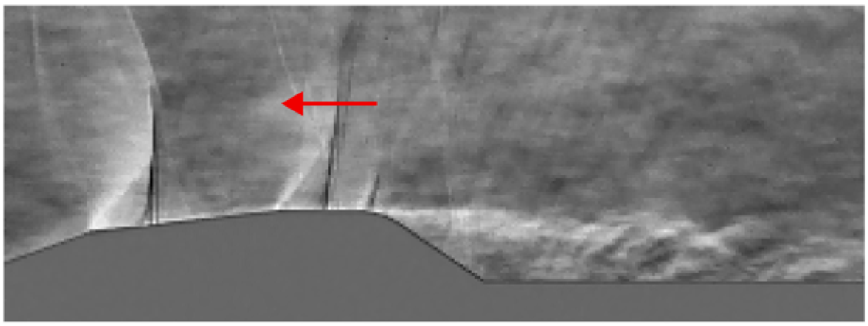

(d) Phase 4

Figure 4.27: Updated shock dynamics for the Radius effect at $M = 0.8$

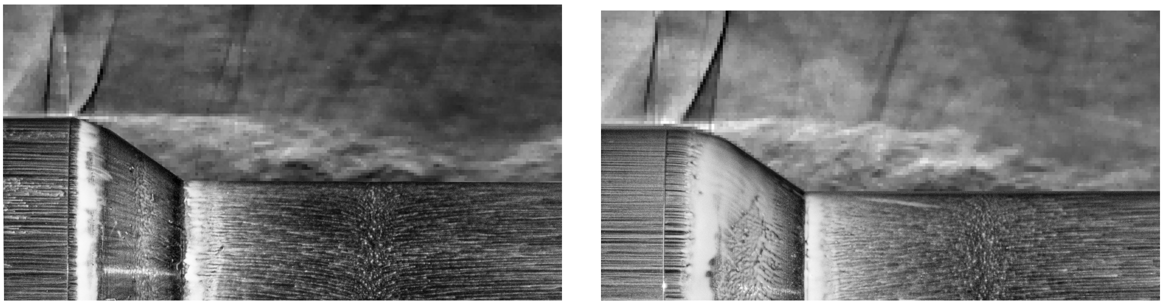

(a) R10

(b) R20

Figure 4.28: Instantaneous schlieren and mean oil flow superimposed images depicting SWBLI at $M = 0.8$.

4.6 Spatial modal analysis

To extract the coherent flow structures, the PIV dataset is analysed using proper orthogonal decomposition(POD). The fluctuations in horizontal(u') velocity component are stacked on top of the vertical(v') velocity component, facilitating the extraction of co-interactive behaviour between the two. The results are then compared with the BFS literature to conclude.

The POD mode energy fraction, along with the cumulative energy sum, is plotted in Figure 4.29 for the first 50 modes at both $M = 0.7$ and $M = 0.8$. The distributions at both Mach numbers are similar, with minimal variations. At $M = 0.7$, the first three modes contribute approximately 23.5% of the total energy, with 50% of the energy captured within the first 18 modes. Similarly, at $M = 0.8$, the first three modes contribute about 23% of the total energy, with 50% of the energy contained in the first 19 modes. The obtained energy spectrum is in very good agreement with the BFS results of Schrijer et al. [55] who found similar values for the energy distribution.

The first mode represents approximately 11% of the total energy at both Mach numbers, and the second(6.5%) and third (5.5%) modes contribute about 12% together. These three modes will be discussed in detail in the following sections. Notably, Mode 2 and Mode 3 are closely spaced in the spectrum, forming a mode pair.

4.6.1 Mode 1: Flapping motion

The spatial distribution of the first POD mode at $M = 0.7$ is shown in Figure 4.30. It exhibits a local maximum for the u component and a local minimum for the v component in the separation region. When the amplitude of this mode reaches its positive maximum, it induces a locally downstream and radially inward motion, increasing the velocity along the shear layer and pushing it toward the second stage. Consequently, the first mode moves the shear layer closer to the boattail corner, effectively reducing the separation region. At its

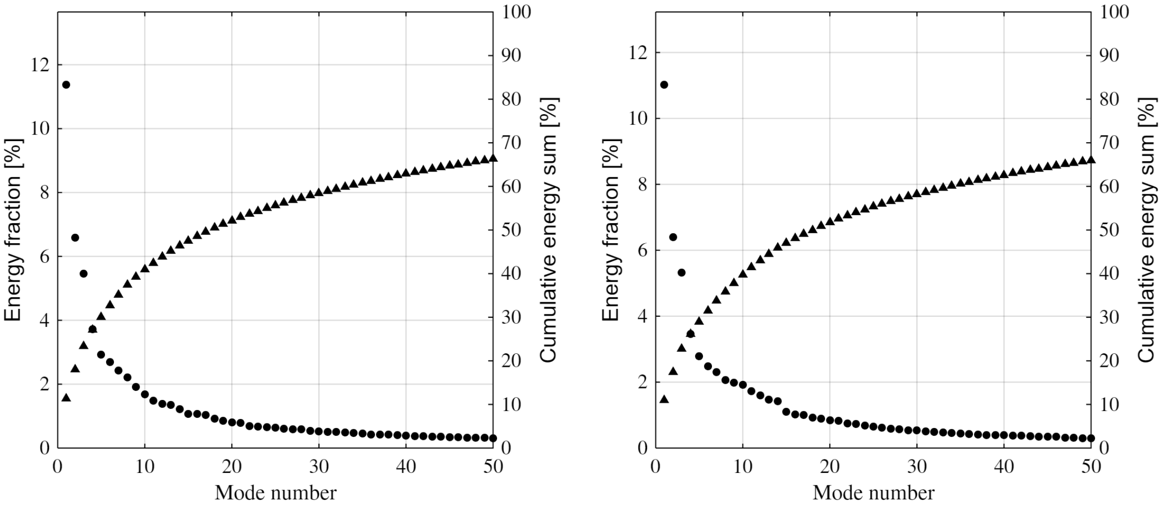

(a) $M = 0.7$

(b) $M = 0.8$

Figure 4.29: POD energy spectrum for R0 case.

negative maximum, the opposite occurs: the first mode pushes the shear layer away from the second stage, enlarging the separation region. Thus, this mode can be associated with the flapping motion of the shear layer and the corresponding cyclic shrinking and growth of the separated region.

A physical explanation of the shear layer flapping mechanism was given by Driver et al. [22]. They associate the flapping phenomenon with an out-of-equilibrium shear layer that modifies the rate of reverse flow. This occurs when a vortical structure carrying more forward momentum than its neighbours escapes the reattachment zone without much of its mass being entrained into the separation region (momentum ejection from the separation region). The resulting reduction in reverse flow causes the separated region to shrink, increasing the shear layer curvature and its impingement angle. This, in turn, strengthens the pressure gradient at reattachment, which retards more low-velocity fluid and reinflates the separation region.

This mechanism becomes evident when the mode structure, scaled with its maximum amplitude, is superimposed on the mean flow field, as shown in Figures 4.31 and 4.32. The u-component plots provide the most notable observations. When the mode is added to the mean u field, the shear layer exhibits increased curvature and downstream motion, resulting in a smaller separation region. The corresponding v-component plot shows a high concentration of radially inward motion upstream of the mean reattachment location (27 mm from the boattail bottom corner), indicating the influence of shear layer curvature and suggesting a higher angle of impingement on the second stage. Conversely, when the mode is subtracted from the mean flow, the u-component plot reveals an expanded reversed-flow region extending beyond the mean reattachment location. In the v-component plot, traces of radially upward motion appear beyond $x = 40$ mm, further supporting the conclusion of an enlarged separation region. These observations confirm that the shear layer flapping associated with this mode is a primary contributor to the unsteadiness observed at the reattachment location.

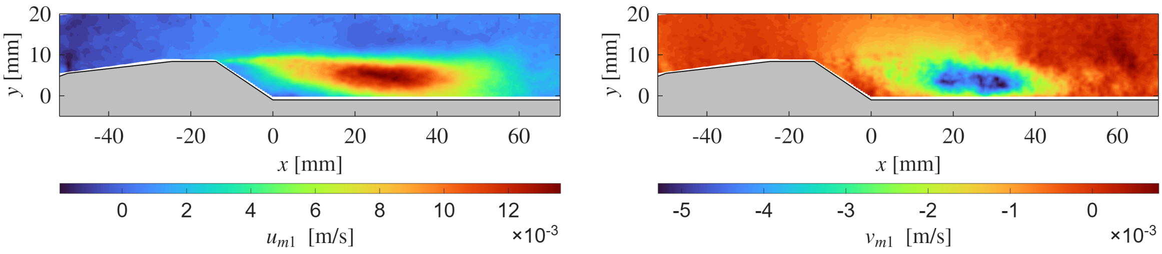

(a) u component (b) v component

Figure 4.30: Shape of the first POD mode at $M = 0.7$.

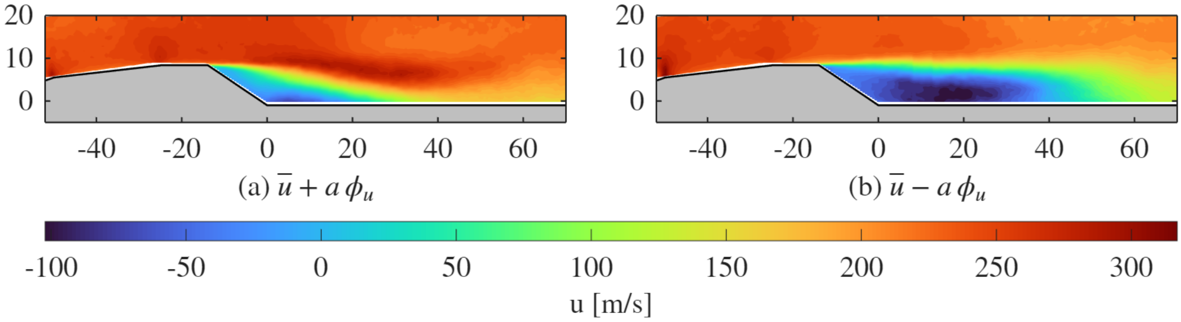

Figure 4.31: u component of first mode superimposed on the mean flow at $M = 0.7$.

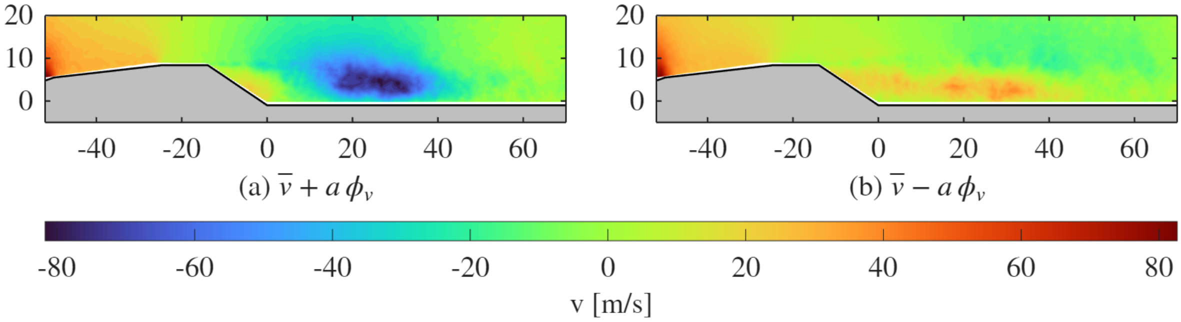

Figure 4.32: v component of first mode superimposed on the mean flow at $M = 0.7$.

Interestingly, a contribution from the second shock is visible in the first mode shape at $M = 0.8$, shown in Figure 4.33. It appears as a local minimum in the u-component shape and as a local maximum in the v-component shape. Notably, this second shock contribution is out of phase with that from the separation region. This means that when the separation region is shrunk, the second shock is weaker and upstream, and when the separation region is enlarged, the second shock is more prominent and downstream. The mode-superimposed mean image in Figure 4.34 provides further insight into this coupling between the second shock and the separation region. The separation region is smaller when the second shock is near its upstream position, and larger when it is near its downstream position.

Physically, this can be explained in relation to shock strength. At the downstream position of the second shock, the expansion over the cone–cylinder junction causes the flow velocity to reach approximately 360 m/s, producing a stronger shock. Due to the high pressure behind the second shock, the shear layer loses energy, resulting in a larger separation region. Conversely, when the second shock is at its upstream position, the expansion region is smaller, producing a weaker shock. and leading to a smaller separation region.

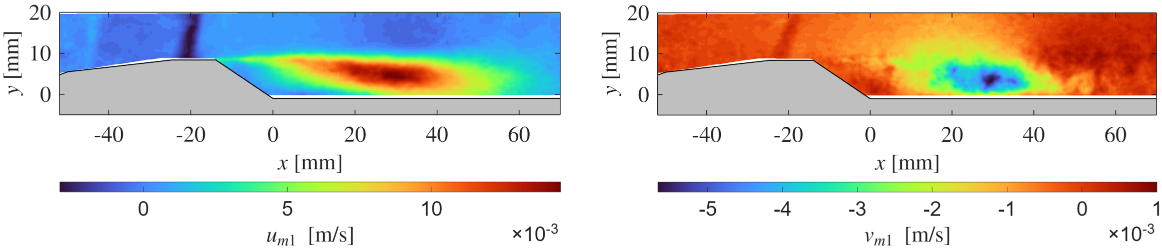

(a) u component

(b) v component

Figure 4.33: Shape of the first POD mode at $M = 0.8$.

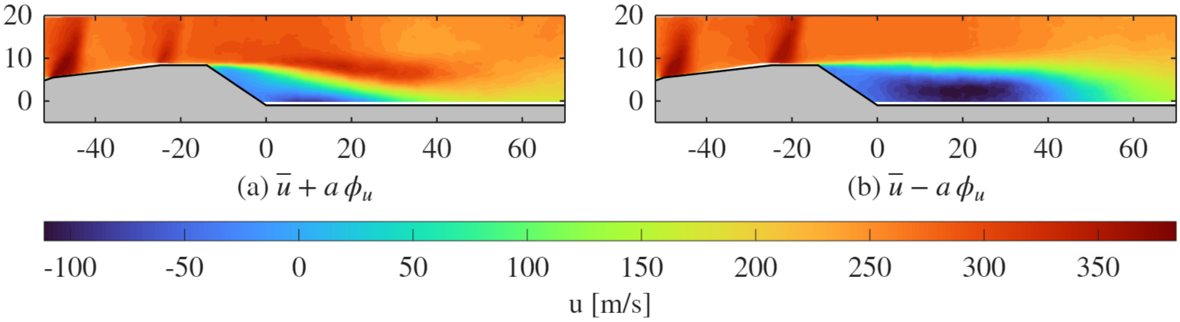

(a) $\bar{u} + a\,\phi_u$

(b) $\bar{u} - a\,\phi_u$

Figure 4.34: u component of first mode superimposed on the mean flow at $M = 0.8$.

4.6.2 Mode 2: Undulation motion

The spatial distribution of the second POD mode at $M = 0.7$ is shown in Figure 4.35. It exhibits two local extrema in both the u- and v-component shapes: the first at $x = 20$ mm and the second at $x = 50$ mm. The region of negligible contribution between these two extrema lies near the mean reattachment point at $x = 27$ mm. The local extrema in u are out of phase with the corresponding extrema in v. The first local extremum causes a reduction in the horizontal velocity component and an increase in the vertical velocity component, resulting in an upward displacement of the shear layer. In contrast, the second extremum increases the horizontal component and decreases the vertical component, producing a downward displacement of the shear layer. Thus, the second POD mode is associated with an inflection of the shear layer and can be linked to the undulating motion of the shear layer.

The amplitude-scaled mode shapes superimposed on the mean flow, shown in Figures 4.36 and 4.37, provide a clearer view of the flow structures associated with the second mode.

The first local extremum, when at maximum positive amplitude, traps more fluid inside the separation region. The second local extremum induces higher downstream and radially downward motion, curving the shear layer toward reattachment. This represents momentum injection into the separation region. Conversely, when at maximum negative amplitude, the opposite occurs, and an inflection in the shear layer is visible in the u-component plot. In this case, a region of slow-moving fluid is being shed, representing momentum ejection from the separation region.

The local extrema in the second mode are located upstream and downstream of the mean reattachment point. The v-component mode-superimposed image(Figure 4.37) shows the undulation motion contributing to either side of the mean reattachment point. Therefore, the undulation motion of the shear layer has minimal influence on the unsteadiness of the reattachment location, but is primarily responsible for the momentum injection and ejection processes in the separation region. The second mode at $M = 0.8$ shows a similar structure with no significant contribution from either of the shocks and is therefore not presented here. The reader is referred to the Appendix F for the mode shapes.

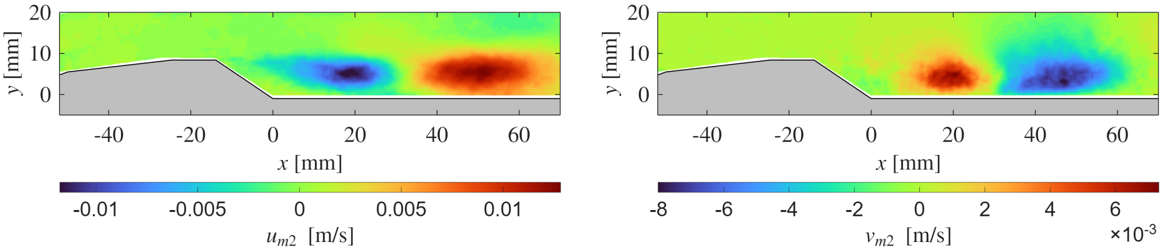

(a) u component

(b) v component

Figure 4.35: Shape of the second POD mode at $M = 0.7$.

Mode 3

The shape of the third POD mode at $M = 0.7$ for the R0 case is shown in Figure 4.38. This mode exhibits a wavelength similar to that of the second mode, but with its extrema located further upstream. Due to the alternating arrangement of local maxima and minima, this mode also contributes to the undulation of the shear layer. Being closely spaced in the POD spectrum, the second and third modes form a mode pair associated with the undulating motion of the shear layer and are responsible for the momentum injection and ejection processes within the separation region.

4.6.3 Radius effects

To analyse the impact of the boattail radius on the spatial modes in the flow, the R10 and R20 cases were planned to be tested at $M = 0.7$ and $M = 0.8$. However, due to operational limitations in the TST-27, only one run for the R10 case at $M = 0.7$ was conducted. As

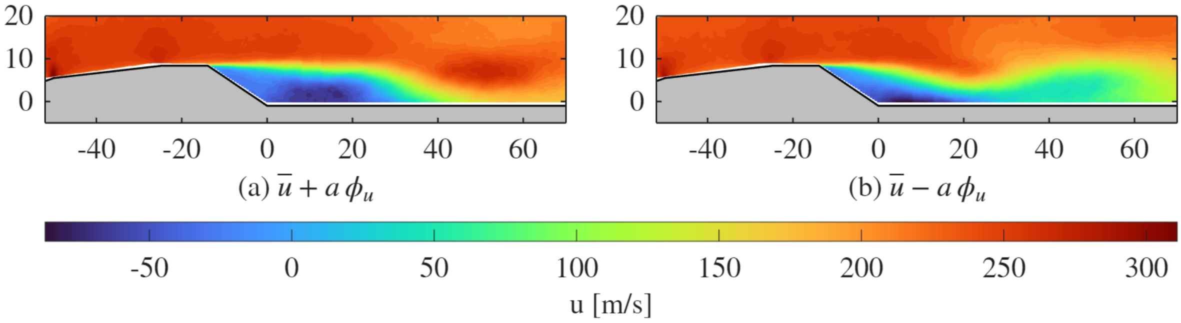

Figure 4.36: u component of second mode superimposed on the mean flow at $M = 0.7$.

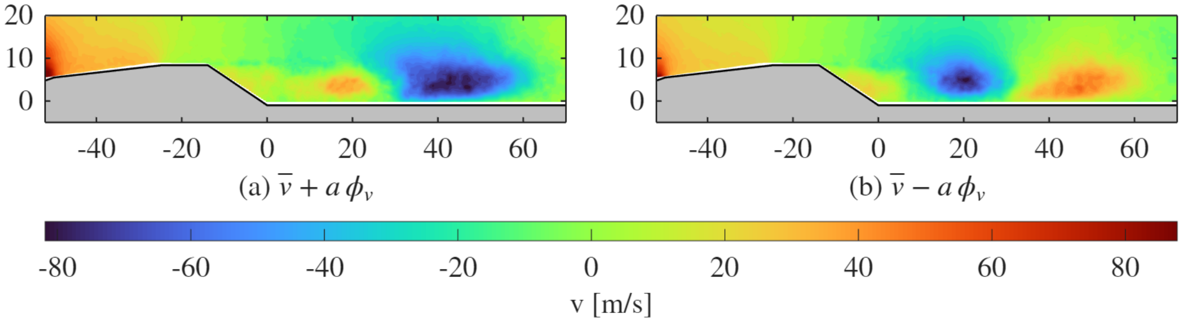

Figure 4.37: v component of second mode superimposed on the mean flow at $M = 0.7$.

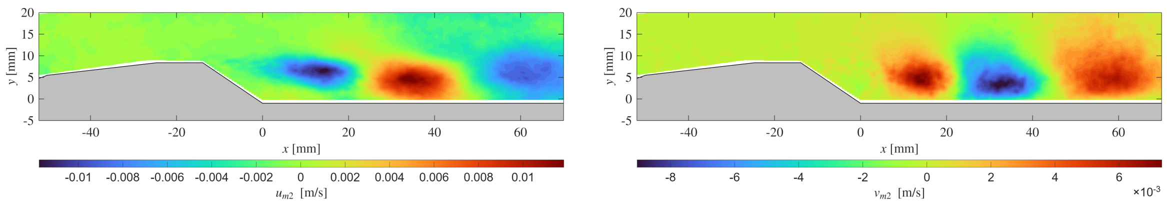

(a) u component

(b) v component

Figure 4.38: Shape of the third POD mode at $M = 0.7$.

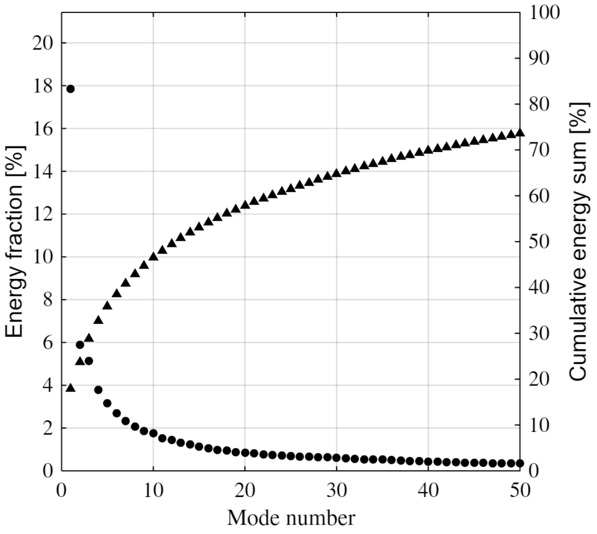

Figure 4.39: POD energy spectrum for R10 case at M = 0.7

mentioned in Section 3.4.3, a total of 1050 PIV snapshots were planned for each configuration, and this was achieved for the R0 case, but only 350 snapshots were captured for the R10 case. The POD energy spectrum for R10 at $M = 0.7$ is shown in Figure 4.39. Approximately 50% of the total energy is captured in the first 13 modes, with the first three modes contributing 29% in total, compared to only 23.5% for the R0 case at $M = 0.7$. This increase arises mainly from the first mode, which alone contributes 18%, while the second and third modes account for 6% and 5%, respectively. To ensure that this increase is not simply an artefact of the smaller sample size, a reduced run of 350 snapshots was also analysed for the R0 case at $M = 0.7$.

The first mode shape shown in Figure 4.40 shows a contribution from the third expansion region over the boattail curvature. This appears as a positive contribution in the u component and a negative contribution in the v component, in phase with the contribution from the separation region in both cases. Further more the contribution from the separation region is more curved on the upper part, indicating that the boattail radius affects the shear layer and thus impacts the shape of the separation region.

The coupling between the separation region and the third expansion region can be inferred from the mode-superimposed mean images in Figures 4.41 and 4.42. At its maximum positive amplitude, there is expansion over the boattail curvature, causing the flow to be deflected downward at separation resulting in a smaller separation region. This is precisely visible from the v component plots, where a higher concentration of radially inward movement is seen over the curvature of the boattail. At its maximum negative amplitude, there is no expansion over the boattail radius and the flow separates almost before the curvature begins, leading to a larger separation region. This mode contributes to higher oscillation in the reattachment point than the R0 case due to the flow following the boattail curvature. This is also seen as an increase in the energy content of the flapping mode.

The undulating modes (Mode 2 and 3) are similar in structure as the ones for R0 case and the reader is referred to the Appendix F to look at the mode shapes.

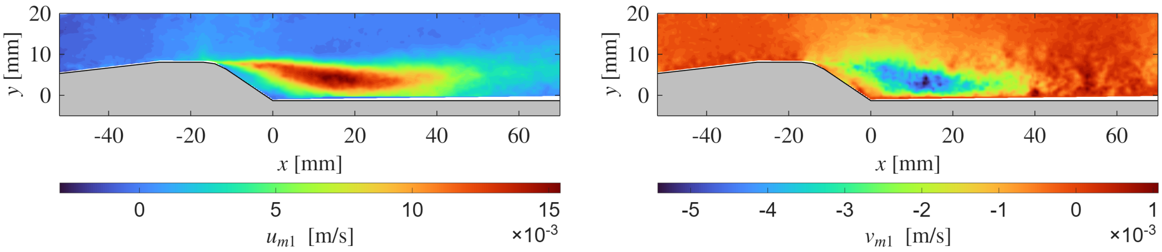

(a) u component

(b) v component

Figure 4.40: Shape of the first POD mode at $M = 0.7$ for R10 case.

Prediction for M = 0.8 case

For M = 0.8 case, it is expected that the contibution from the second shock for the flapping motion will be taken over by the third shock. This is based on seeing a contribution of the thrid expansion region to flapping mode at M = 0.7, and also due to the shear layer lifting at the third shock foot seen in the schlieren images. Like the second shock in the R0 case, the contribution from the third shock in R10 and R20 is expected to be out of phase with the separation region. This will cause the separation region to be larger when the thrid shock is present and be smaller when its not present. This pattern is seen in Section 4.7, where spectral POD modes from the schlieren images are discussed.

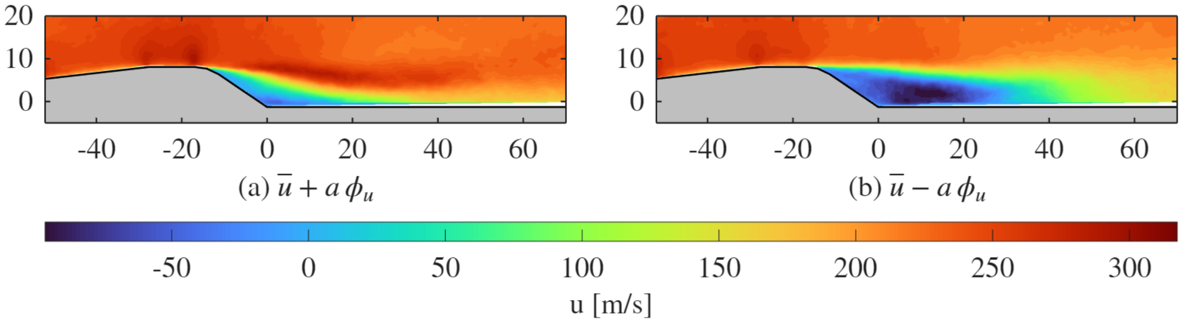

Figure 4.41: u component of first mode superimposed on the mean flow at $M = 0.7$ for R10 case.

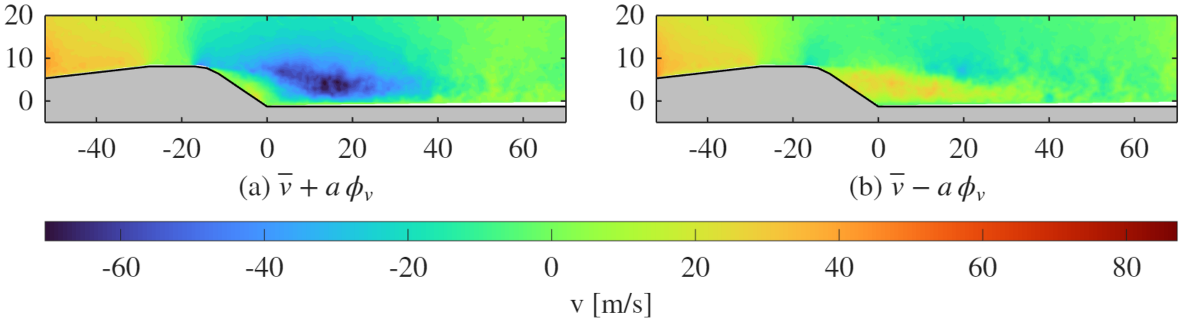

Figure 4.42: v component of first mode superimposed on the mean flow at $M = 0.7$ for R10 case.

4.7 Spatio-temporal Modal analysis

The use of a high acquisition rate of 25 kHz in schlieren enables detailed spectral analysis of the flow field, with a maximum resolved frequency of 12.5 kHz. To this end, two complementary methods are employed. First, a pixel of interest is selected, and the pixel intensities within a surrounding 4 × 4 window are averaged. The Fourier transform of this averaged intensity time series is then computed to identify dominant energetic frequencies. Second, the entire Schlieren image dataset is processed using a spectral proper orthogonal decomposition (SPOD) algorithm, which extracts the dominant spatial modes associated with these energetic frequencies. It is done in an effort to extract the frequencies at which the flapping and undulation modes oscillate. The spectrum from SPOD is generated by summing the first 5 modes at each resolved frequency. As already mentioned in Section 3.6.4, the frequency resolution of this analysis is $12.2 Hz$ and Strouhal number resolution ranges from 0.0004 to 0.0006. The frequency spectrum is presented in terms of the Strouhal number based on the step height of the HHF, which is defined as follows:

$$St_h = \frac{f \times h}{u} \tag{4.1}$$

where f is the frequency in Hz, h is the step height in m, and u is the freestream velocity in m/s.

Figure 4.44 presents the Strouhal number spectra obtained from pixel intensity signals at three representative locations in the flow: the shear layer, the first shock, and the second shock (as indicated in Figure 4.43). The first shock shows a single tonal peak at $St_h = 0.0156$, indicating oscillation at a frequency of 410 Hz. This frequency has previously been identified as a characteristic noise of the wind tunnel in earlier studies conducted in this facility [49, 19, 18]. Solana [46] performed Schlieren measurements in an empty test section and found that the facility noise is concentrated at 415 Hz, remaining unchanged for the two Mach numbers tested ($M = 0.75$ and $M = 0.8$). It is therefore inferred that the first shockwave couples with

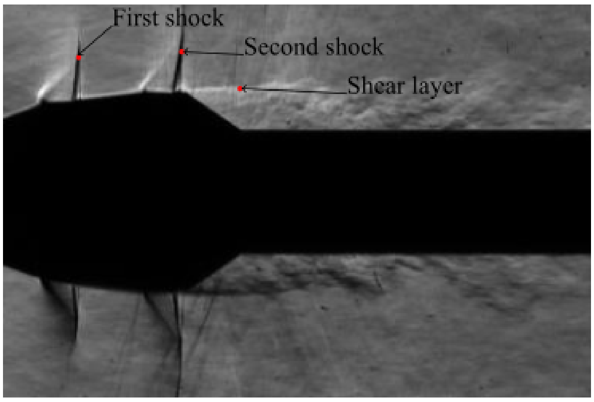

Figure 4.43: Location of sample pixels for FFT

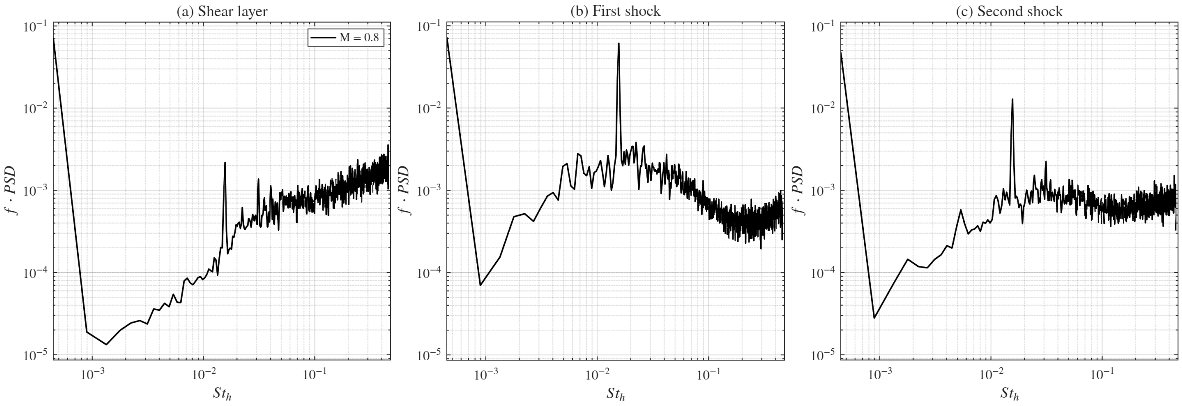

Figure 4.44: FFT of pixel intensities at different locations for R0 at M = 0.8

the tunnel's pressure disturbances and oscillates at this same frequency.

Inspection of the pressure-tap frequency spectrum from Panda et al. [42] (Figure 4.45) suggests the presence of peaks near 400 Hz and 800 Hz at $M = 0.8$ for the K05 location, downstream of the bi-conic junction. Although these features were not explicitly discussed in their study, they may indicate that the shock system in their configuration oscillated at a frequency close to 400 Hz, distinct from the tunnel background noise reported around 1200 Hz. In the present facility (TST-27), the tunnel background noise is centred at $\sim$ 415 Hz. The close agreement between this facility tone and the $\sim$ 400 Hz peak observed in Panda's spectrum suggests that the shock oscillations become frequency-locked with the dominant tunnel disturbance.

The second shock shows two peaks—one at $St_h = 0.0156$ and another at $St_h = 0.031$. The second peak corresponds to a frequency of 847 Hz, which is close to the first harmonic of the 410 Hz fundamental. These two peaks are also visible in the shear layer spectrum, although with significantly lower intensity, and there is a much higher contribution from the higher frequencies in the shear layer.

4.7.1 Mach number effect

The Strouhal number spectra for the R0 configuration at different Mach numbers are presented in Figure 4.46. Panel (a) shows the premultiplied FFT spectra obtained from pixel intensity fluctuations in the shear layer, while panel (b) shows the corresponding SPOD spectra, summed over modes 1–5.

For the $M = 0.6$ case, the shear-layer FFT spectrum does not exhibit any distinct tonal peaks. This is likely due to the weak compressibility effects at this low Mach number, combined with the low convection speed of structures within the separated region, making their detection in schlieren images more difficult. However, the SPOD spectrum for $M = 0.6$ reveals multiple peaks, albeit at lower energy levels than those observed for the higher Mach number cases. The first of these occurs at $St_h = 0.027$, followed by a harmonic at $St_h = 0.052$. The other peaks observed in SPOD spectra could be artifacts from the processing algorithm, as the mode

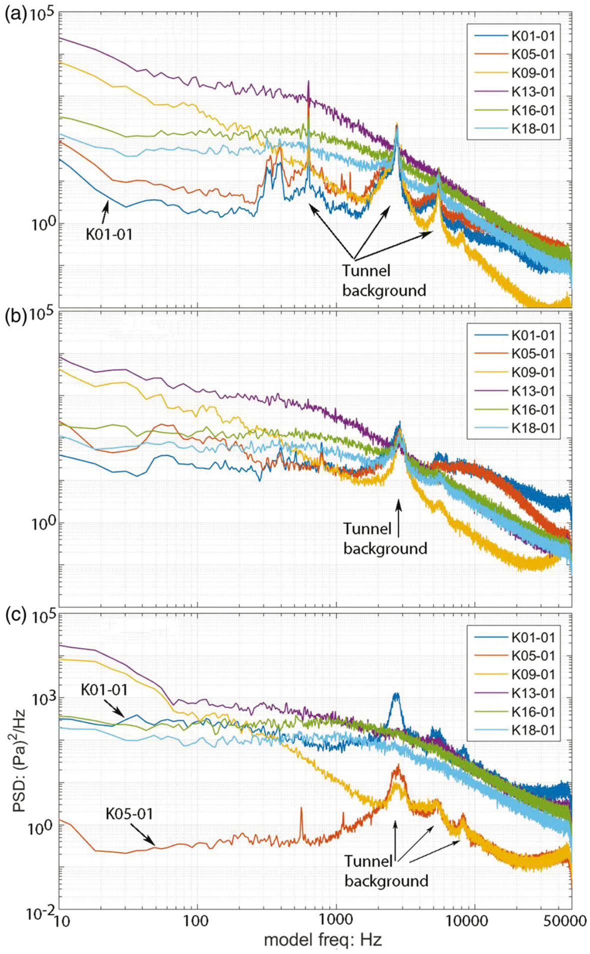

Figure 4.45: Frequency spectrum from pressure transducers reported by Panda et al.[42] (a) M = 0.6 (b) M = 0.8 (c) M = 1.1

shapes at those frequencies don't exhibit coherent structure and show large contributions from the freestream. Refer Appendix H, for the mode shapes at these frequencies.

In contrast, the $M = 0.7$ and $M = 0.8$ cases show well-defined spectral peaks at $St_h = 0.017(412Hz)$ and $St_h = 0.015(410Hz)$, respectively. As discussed earlier, these correspond to the characteristic facility noise of the TST-27 wind tunnel, which occurs at a fixed frequency of approximately 415 Hz, independent of the flow Mach number. Because the Strouhal number is normalised by the flow speed, the same absolute frequency manifests at different St_h values for different Mach numbers.

Both $M = 0.7$ and $M = 0.8$ also exhibit secondary peaks at their respective first harmonics of the tunnel noise: $St_h = 0.034$ for $M = 0.7$ and $St_h = 0.031$ for $M = 0.8$. These harmonic peaks are present in both the shear-layer FFT spectra and the SPOD spectra, but with greater clarity and energy concentration in the SPOD results, indicating that contributions arise from the overall flow field rather than just the shear layer. Both the spectra for M = 0.8 show a broadband peak in the range $St_h = 0.01$ to $St_h = 0.08$, inclusive of the two tonal peaks, unlike at other Mach numbers. This could be due to the intense pressure waves in the windtunnel being spread across a frequency range.

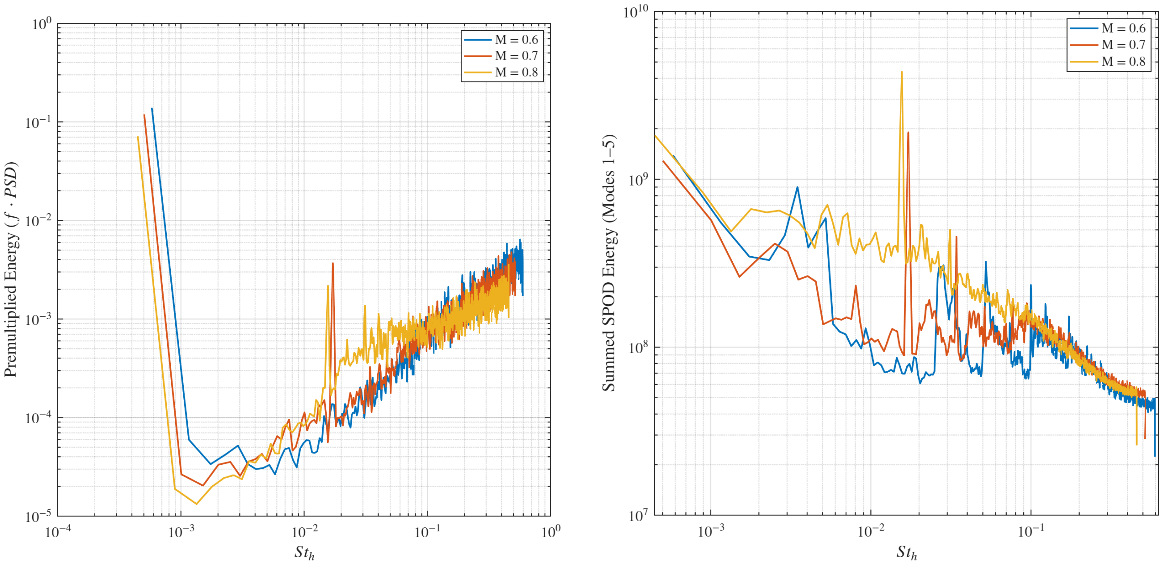

(a) FFT in the shear layer

(b) SPOD spectrum

Figure 4.46: Strouhal number spectrum for R0 case at different Mach numbers

The mode shapes corresponding to the flapping mode for the R0 case are shown in Figure 4.47. For $M = 0.7$ and $M = 0.8$ [Figures 4.47(b) and 4.47(c)], the flapping mode exhibits contributions from both the first and second shocks. As discussed in Section 4.6, at $M = 0.8$ the shear-layer flapping is primarily coupled to the oscillation of the second shock, and such coupling is expected to be confined to the separation region and the second shock. However, the SPOD modes also reveal contributions from the first shock. This arises because SPOD extracts dominant spatial modes at specific frequencies, and therefore any component oscillating at the same frequency—as in the case of the first shock—appears in the corresponding mode, even if it is not physically coupled to the shear layer dynamics.

Interestingly, the SPOD mode shapes show the second shock and the shear layer to be in phase, which is opposite to the out-of-phase behaviour observed in the POD results. This difference is not due to a discrepancy or error, but rather a result of the physical quantity visualised by schlieren imaging. Schlieren visualises gradients of refractive index, which in compressible flows are directly related to pressure gradients. In the instantaneous images, the expansion region and shear layer on the upper surface appear as lighter regions. The present mode shape therefore indicates that when the expansion region over the cone–cylinder junction is larger, the shear layer remains relatively straight, producing a larger separation bubble. Conversely, when the second expansion is weaker, the shear layer angles downward into the second-stage, thereby reducing the extent of the separation region. In other words, a downstream position of the second shock corresponds to a straight shear layer, whereas an upstream position is associated with a curved shear layer.

As discussed earlier, the shocks are locked to the facility's characteristic frequency. Since the flapping mode promotes coupling between the second shock and the shear layer, the shear layer flapping at higher Mach numbers is also locked to this frequency. For $M = 0.6$, where no discernible shocks are present, the shear-layer flapping is free to occur at its natural frequency of $St_h = 0.027$ $(567Hz)$. In the absence of tunnel frequency coupling, it is expected that the flapping frequency of the shear layer (and associated shock oscillations) at higher Mach numbers would also be close to this value. Notably, the first and the second shock appear out of phase with each other, further strengthening the dynamics of the system discussed in Section 4.5.1

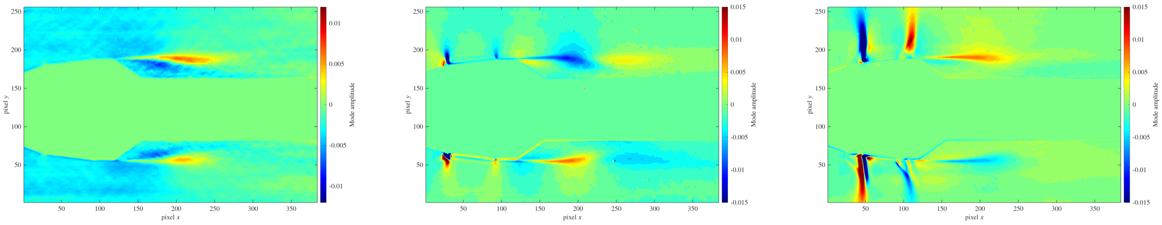

(a) M = 0.6, $St_h = 0.027$ (b) M = 0.7, $St_h = 0.017$ (c) M = 0.8, $St_h = 0.015$

Figure 4.47: Flapping mode at different Mach numbers for R0 case

The undulation modes for the R0 case at different Mach numbers are presented in Figure 4.48. In agreement with the POD mode shapes discussed earlier, the SPOD results show no significant contributions from either the first or second shock at the higher Mach numbers. The mode shapes obtained from SPOD are also less spatially coherent compared to the POD results, which can be attributed to the influence of background tunnel pressure waves contaminating the flow signal. In addition, the flow structure within the separation region is not as clearly discernible. This is primarily because the slow-moving fluid in this region produces relatively weak compressibility effects, making it more difficult for schlieren imaging to resolve the features sharply.

The undulation mode at $M = 0.6$ occurs at a much higher Strouhal number, $St_h = 0.99$, compared to the lower values observed at the higher Mach numbers ($St_h = 0.076$ for $M = 0.7$ and $St_h = 0.071$ for $M = 0.8$). This discrepancy is again likely linked to the reduced compressibility effects at $M = 0.6$.

4.7.2 Radius effect

The Strouhal number spectra for the R0, R10, and R20 cases at $M = 0.8$ are shown in Figure 4.49. The peaks associated with the shock oscillations occur at the same Strouhal number across all three boattail radius configurations, indicating that the dominant shock dynamics remain locked to the tunnel's characteristic frequency. However, as seen in Figure 4.49(a), the shear layer energy levels increase for the radius cases, suggesting stronger large-scale unsteadiness in the separated flow.

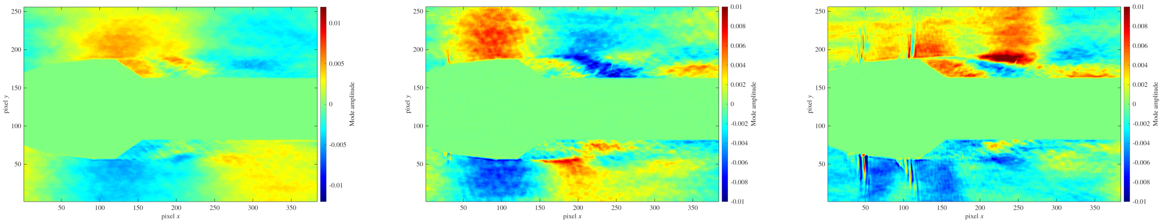

(a) M = 0.6, $St_h = 0.99$ (b) M = 0.7, $St_h = 0.076$ (c) M = 0.8, $St_h = 0.071$

Figure 4.48: Undulation mode at different Mach numbers for R0 case

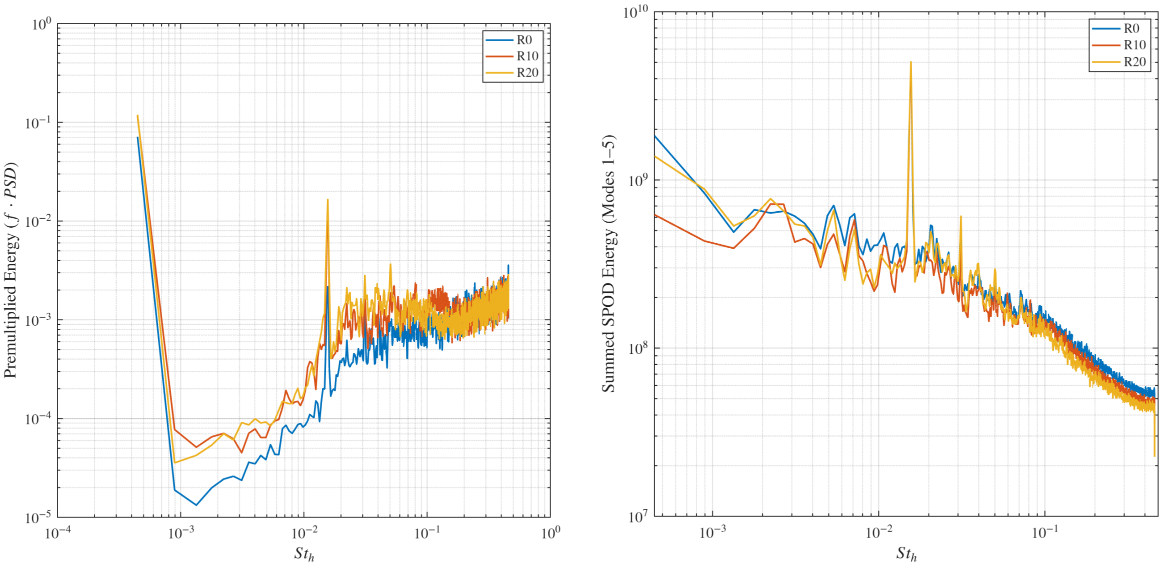

(a) FFT in the shear layer (b) SPOD spectrum

Figure 4.49: Strouhal number spectrum for R0, R10 and R20 cases at M = 0.8

The corresponding flapping and undulation mode shapes for the R10 and R20 cases are presented in Figures 4.50 and 4.51, respectively. The most notable radius-induced changes appear in the flapping mode structures. As predicted in Section 4.6.3, the radius cases show a distinct contribution from a third shock wave, located along the boattail curvature. Consistent with the prediction earlier, this third shock oscillates out of phase with the shear layer motion.

The coupling mechanism between the third shock and the shear layer can be interpreted using the same analogy discussed earlier for the R0 flapping modes. In schlieren images, the third shock manifests as a darker region on the upper side of the model, over the boattail curvature. The mode shapes indicate that when the third shock is present (darker region), the shear layer on the upper surface becomes straighter (uniform lighter band), which correlates with a larger separation bubble. Conversely, when the third shock disappears and the flow follows the curvature to expand (lighter region over the boattail curvature), the shear layer curves more steeply towards the second stage, reducing the size of the separation bubble.

The clear out-of-phase relationship between the three-shock structure and the shear layer observed in these SPOD modes reinforces the dynamics described in Section 4.5.2, further highlighting the influence of boattail radius on the shock–shear layer interaction.

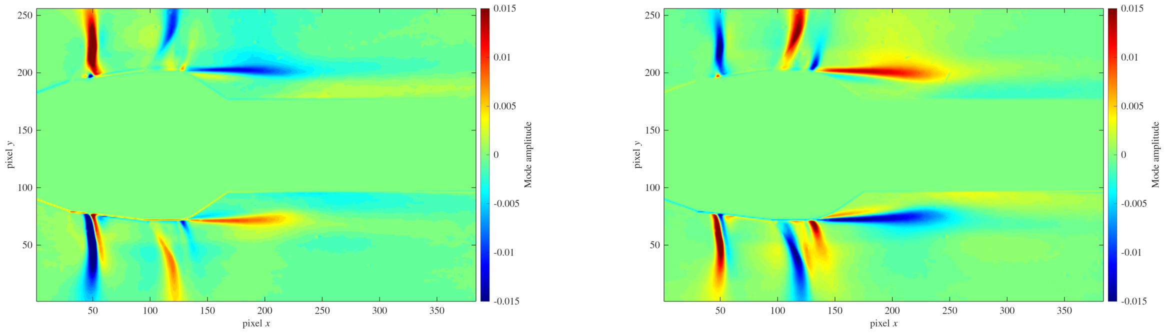

(a) R10, $St_h = 0.0156$

(b) R20, $St_h = 0.0156$

Figure 4.50: Flapping mode at at M = 0.8 for R10 and R20 cases

4.7.3 Discussion

The Strouhal numbers for the flapping and undulation modes across all tested configurations were extracted. The flapping mode maintains a consistent St_h for a given Mach number, while the undulation mode shows noticeable variation across configurations at $M = 0.7$ and $M = 0.8$, as illustrated in Figure 4.52. The corresponding Strouhal numbers for both modes are summarised in Table 4.2, where the mean value is reported for Mach numbers exhibiting configuration-dependent variation.

Scharnowski et al. [58], using DMD on a Zonal RANS–LES simulation of a planar BFS at $M = 0.8$, reported $St_h = 0.01$ for the flapping mode and $St_h = 0.07$ for the undulation mode (termed "pumping" and "flapping," in their article). In comparison, Schrijer et al. [55]

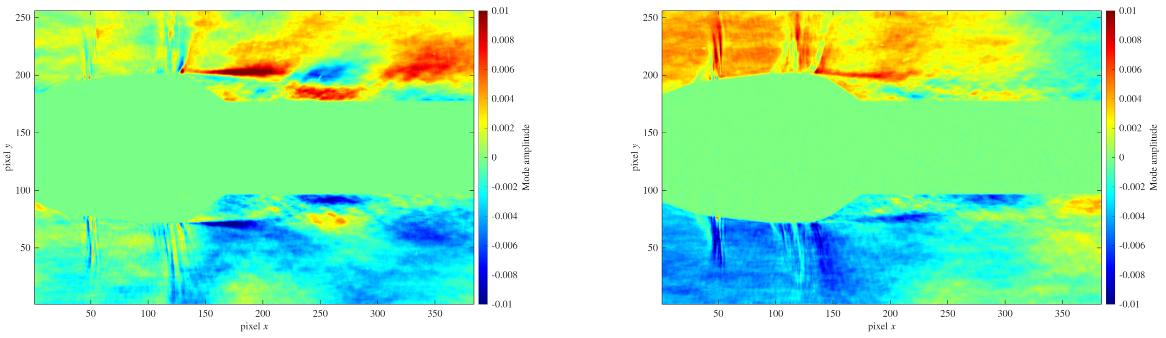

(a) R10, $St_h = 0.082$

(b) R20, $St_h = 0.072$

Figure 4.51: Undulation mode at M = 0.8 for R10 and R20 cases

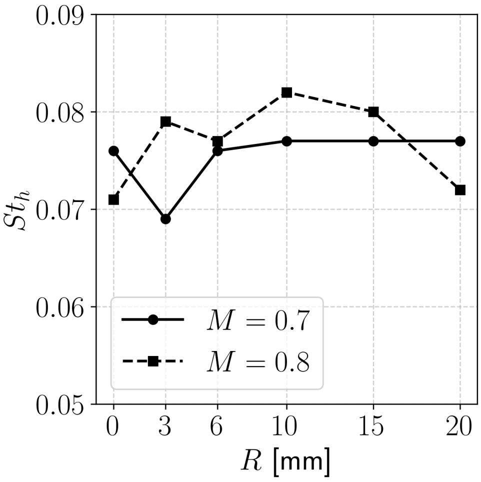

Figure 4.52: Strouhal numbers of the undulation mode across all configurations.

employed high-speed PIV on an axisymmetric BFS at $M = 0.7$, obtaining higher values of $St_h = 0.047$ and $St_h = 0.134$ for the flapping and undulation modes, respectively.

At $M = 0.6$, the extracted flapping- and undulation-mode frequencies align closely with Schrijer et al. [54], but differ from Scharnowski et al. [58], likely due to geometric and flow-setup differences between axisymmetric and planar BFS configurations. At higher Mach numbers ($M = 0.7$ and $M = 0.8$), the extracted flapping-mode frequencies deviate from those reported in both planar [58] and axisymmetric [55] BFS studies; this discrepancy in St_h is attributed to locking of the shocks to the tunnel's characteristic frequency in the present facility. By contrast, the undulation-mode frequencies show closer agreement with literature values (e.g. $St_h \approx 0.07$ in [58]). It is worth noting that the models in those studies had $d/D = 0.4$, whereas Model 11 has $d/D = 0.625$, which may also contribute to the observed differences. Overall, the present results compare well with the BFS literature, except for modes directly influenced by shock–tunnel interactions.

Mach Number	Flapping St_h	Undulation St_h
0.6	0.027	0.10
0.7	0.017	0.077
0.8	0.015	0.077

Table 4.2: Extracted Strouhal numbers with respect to step height (St_h)

5

Conclusion

This study investigated the effect of boattail radius on transonic flows over Hammerhead Fairings (HHFs). An academic HHF configuration, the Coe and Nute Model 11, was selected as the test platform owing to its extensive documentation in literature and its ability to capture the essential flow features of HHF geometries. The motivation for this research stemmed from the absence of a systematic investigation into the influence of boattail radius on HHF flows. Although prior work has characterised HHF aerodynamics using techniques such as schlieren imaging, shadowgraphy, and unsteady pressure-sensitive paints, advanced measurement methods such as particle image velocimetry (PIV) have only recently been applied to the Model 11, and no published study has examined its unsteady flow dynamics using advanced modal decomposition techniques. This thesis, therefore, aimed to address two primary gaps: the influence of boattail radius on HHF aerodynamics and the characterisation of the unsteady flow field using advanced analysis tools.

To define a meaningful set of boattail radii, the turbulent boundary layer (TBL) thickness at separation was estimated using the reference temperature method and a flat-plate approximation. Radius values were then selected to ensure the ratio of radius to TBL thickness ranged from near unity to an order of magnitude greater. Two experimental campaigns were conducted. The first consisted of an exploratory high-speed schlieren study across all radius configurations, followed by oil-flow visualisation at selected cases to extract mean flow features. The second campaign focused on PIV measurements at selected configurations, optimised for high spatial resolution at the expense of temporal resolution. Post-processing employed advanced techniques such as proper orthogonal decomposition (POD) and spectral proper orthogonal decomposition (SPOD).

Key Outcomes

RQ1: How does the boattail edge radius affect the flow in a hammerhead fairing configuration? The introduction of a boattail radius was found to generate a third expansion region over the curvature, occasionally terminated by a third shock. Configurations were classified into two categories: *weak radius effects* (R3, R6) with minimal third shock presence, and *strong radius effects* (R10, R15, R20) with a prominent third shock and a λ-shock structure. Strong radius configurations promoted shock-induced separation, producing a small separation bubble at the shock foot. The addition of a boattail radius also reduced reattachment length substantially—by about 10% for R3, and by 15–25% for R10 and R20 compared to the baseline. However, the third shock lifted the shear layer, leading to higher oscillations in the reattachment location, as indicated by smeared oil-flow patterns.

RQ2: How can the unsteady flow field be characterised? The separation region was dominated by two primary modes, similar to those in backward-facing step (BFS) flows. The first, a *flapping mode*, governed oscillations in the reattachment point; its higher energy content in the R10 case indicated larger oscillations in reattachment point. The second, an *undulation mode*, was linked to momentum injection and ejection from the separation bubble. The flapping mode was strongly influenced by geometric and flow features—at $M = 0.8$ for R0 it was coupled to the second shock, whereas at $M = 0.7$ for R10 it interacted with the third expansion region. SPOD mode shapes confirmed that flapping behaviour in radius cases at $M = 0.8$ was associated with the third shock. Spectral analysis revealed that the flapping mode occurred at $St_h = 0.027$ for $M = 0.6$, close to the BFS literature, but shifted to $St_h = 0.017$ and $St_h = 0.015$ at $M = 0.7$ and $M = 0.8$ due to tunnel-induced frequency locking. The undulation mode appeared at $St_h = 0.077$ for $M = 0.7$ and $M = 0.8$, again in line with BFS literature, but was higher ($St_h = 0.1$) at $M = 0.6$.

In addition to these results, a detailed interpretation of the system dynamics was developed, supported by complementary evidence from the SPOD mode shapes. Cross-correlation of the first and second shock positions revealed an upstream convective velocity of approximately 36 m/s, suggesting that the associated disturbances are acoustic in nature. Overall, the findings demonstrate that increasing the boattail radius shortens the separation length but simultaneously introduces an additional shock system, which amplifies the unsteadiness of the reattachment location. These effects carry important implications for the unsteady loading and overall stability of launch vehicles, and warrant further investigation through direct quantification of the unsteady forces.

5.1 Limitations

The main limitations of this study were:

1. The presence of facility-induced pressure waves, which locked shock oscillations to the tunnel's characteristic frequency, limiting true spectral characterisation.
2. PIV measurements were acquired at only 10 Hz, restricting spectral analysis of POD time coefficients and preventing phase-averaged shock position studies.
3. Operational constraints curtailed the PIV campaign, resulting in no $M = 0.8$ data for radius configurations.
4. Knife-edge blockage ratio changes between test days affected schlieren image contrast and illumination consistency.
5. Rapid succession of oil-flow runs led to reduced model surface temperature, causing oil to adhere more strongly and producing patchy patterns.

6. Literature on transonic BFS flows reporting the spectral content of the modes is only available for models with $d/D = 0.4$. Since Model 11 has $d/D = 0.625$, this geometric difference could have contributed to the variations observed in the Strouhal number values.

5.2 Recommendations for Future Work

Future research should:

1. Complete PIV measurements for radius cases at higher Mach numbers to extend understanding of unsteady behaviour.
2. Conduct high-speed PIV to complement schlieren-based spectral analysis.
3. Perform comprehensive CFD studies to determine spectral characteristics free from facility effects and to enhance physical interpretation.
4. Investigate edge radius effects in canonical BFS flows using both experimental and computational methods.
5. Quantify unsteady aerodynamic loads on the Model 11 with varying boattail radii.

In summary, this work provides the first systematic experimental investigation of boattail radius effects on HHF aerodynamics, combining schlieren, oil-flow, and PIV measurements with advanced modal analysis. The findings show that while larger boattail radii can beneficially reduce separation length, they introduce additional shock structures that intensify unsteady separation dynamics, potentially impacting vehicle stability. These results contribute valuable new data to the open-access HHF database and offer insight into design trade-offs relevant to both academic research and industrial applications.

Bibliography

[1] Melling A. *PIV uncertainty propagation - IOPscience.*

[2] John David Anderson. *Fundamentals of aerodynamics.* en. Sixth edition. McGraw-Hill series in aeronautical and aerospace engineering. New York, NY: McGraw-Hill Education, 2017.

[3] A.C. Avelar, E. Basso, J.B.P.F. Filho, C.P.F. Francisco, and P.G.M. Romero. "Analysis of the flow patterns on the fore-body section of a sounding vehicle in the transonic regime." In: *Journal of the Brazilian Society of Mechanical Sciences and Engineering* 40.3 (2018). DOI: 10.1007/s40430-018-1030-y.

[4] Ana Cristina Avelar, João Batista, P Falcão Filho, and Josenei G Medeiros. "Experimental analysis of the flow field on a hammerhead fairing satellite launch vehicle in transonic regime using pressure sensitive paint." en. In: (2015).

[5] Suresh B.N. and Sivan K. *Integrated Design for Space Transportation System.* Springer, 2015.

[6] Holger Babinsky and John K Harvey. "Shock Wave - Boundary Layer Interactions." In: *Cambridge University Press* (2011).

[7] I. Bolgar, S. Scharnowski, and C.J. Kähler. "Passive flow control for reduced load dynamics aft of a backward-facing step." In: *AIAA Journal* 57.1 (2019), pp. 120–131. DOI: 10.2514/1.J057274.

[8] Istvan Bolgar, Sven Scharnowski, and Christian J. Kähler. "The Effect of the Mach Number on a Turbulent Backward-Facing Step Flow." en. In: *Flow, Turbulence and Combustion* 101.3 (Oct. 2018), pp. 653–680. DOI: 10.1007/s10494-018-9921-7.

[9] P. Catalano, M. Marini, A. Nicoli, and A. Pizzicaroli. "CFD contribution to the aerodynamic data set of the vega launcher." In: *Journal of Spacecraft and Rockets* 44.1 (2007), pp. 42–51. DOI: 10.2514/1.23534.

[10] Kalyana Chakravarthy, Konark Arora, and Debasis Chakraborty. "Use of digitally filtered inflow conditions for LES of flows over backward facing steps." In: *European Journal of Mechanics - B/Fluids* 67 (Jan. 2018), pp. 404–416. DOI: 10.1016/j.euromechflu.2017.10.006.

[11] Lin Chen, Keisuke Asai, Taku Nonomura, Guannan Xi, and Tianshu Liu. "A review of Backward-Facing Step (BFS) flow mechanisms, heat transfer and control." en. In: *Thermal Science and Engineering Progress* 6 (June 2018), pp. 194–216. DOI: 10.1016/j.tsep.2018.04.004.

[12] Kyong Chol Chou. "Aerodynamic problems of Launch Vehicles." In: *Journal of Astronomy and Space Sciences* (1984).

[13] Charles F Coe and B Nute. *Steady and Fluctuating pressures at transonic speeds on Hammerhead launch vehicles.* en. 1962.

[14] Charles F. Coe. *Steady and fluctuating pressures at transonic speeds on two space vehicle payload shapes*. Tech. rep. NASA Ames Research Center, 1962.

[15] Charles F. Coe. *The effects of some variations in launch-vehicle nose shape on steady and fluctuating pressures at transonic speeds*. Tech. rep. NASA Ames Research Center, 1962.

[16] S.R. Cole and T.L. Henning. “Buffet response of a hammerhead launch vehicle wind-tunnel model.” In: *Journal of Spacecraft and Rockets* 29.3 (1992), pp. 379–385. DOI: 10.2514/3.26362.

[17] Vinicius Merlin Santos Costa. “Applications of pressure sensitive paints to Hammerhead launcher aerodynamics.” MA thesis. TU Delft, 2024.

[18] Alessandro D’Aguanno. “Physics and Control of Transonic Buffet.” en. In: (2023). DOI: 10.4233/7e4f868b-7716-4c36-8fa0-b55572d1572b.

[19] Alessandro D’Aguanno, Ferry Scheijer, and Bas van Oudheusden. *Transonic PIV based unsteady pressure measurements for launcher environment*. Tech. rep. TU Delft, 2024.

[20] A. D’Aguanno, A.G. Romero, F.F.J. Schrijer, and B.W. van Oudheusden. “Flow analysis of hammerhead launcher geometries in the transonic regime.” In: 2024. DOI: 10.2514/6.2024-2145.

[21] Sébastien Deck and Pascal Thorigny. “Unsteadiness of an axisymmetric separating-reattaching flow: Numerical investigation.” In: *Physics of Fluids* 19.6 (June 2007), p. 065103. DOI: 10.1063/1.2734996.

[22] David M. Driver, H. Lee Seegmiller, and Joe G. Marvin. “Time-dependent behavior of a reattaching shear layer.” en. In: *AIAA Journal* (May 2012). DOI: 10.2514/3.9722.

[23] F.J. Donker Duyvis. “Laser sheet probe design for PIV in high speed wind tunnels.” In: *PIVNET II International workshop on the applications of PIV in compressible flows, Delft, The Netherlands*. 2005.

[24] L.E. Ericsson. “Hammerhead wake effects on elastic vehicle dynamics.” In: *Journal of Spacecraft and Rockets* 34.2 (1997), pp. 145–151. DOI: 10.2514/2.3193.

[25] *Experimental Visualizations of a Generic Launch Vehicle Flow Field: Time-Resolved Shadowgraph and Infrared Imaging*. en. DOI: 10.2514/6.2017-1403.

[26] R.M. Hall, S.X. Bauer, and J.A. Blevins. “Aerodynamic characterization of the ares launch vehicles.” In: *Journal of Spacecraft and Rockets* 49.4 (2012), pp. 558–563. DOI: 10.2514/1.A32174.

[27] Weibo Hu, Stefan Hickel, and Bas W. Van Oudheusden. “Low-frequency unsteadiness mechanisms in shock wave/turbulent boundary layer interactions over a backward-facing step.” en. In: *Journal of Fluid Mechanics* 915 (May 2021), A107. DOI: 10.1017/jfm.2021.95.

[28] Laura Hudy, Ahmed Naguib, William Humphreys, and Scott Bartram. *PIV Measurements of a 2D/3D Separating/Reattaching Boundary Layer Downstream of an Axisymmetric Backward-facing Step*. en. DOI: 10.2514/6.2005-114.

[29] R. A. Humble, F. Scarano, and B. W. van Oudheusden. “Unsteady Flow Organization of a Shock Wave/Turbulent Boundary Layer Interaction.” en. In: *IUTAM Symposium on Unsteady Separated Flows and their Control*. Springer, Dordrecht, 2009, pp. 319–330. DOI: 10.1007/978-1-4020-9898-7_27.

[30] S. Jamshed, M. Husain, and I. Afzal. “Numerical Analysis of Buffet-Causing Phenomenon in Hammerhead Shaped Body.” In: 2023, pp. 677–683. DOI: 10.1109/IBCAST59916.2023.10712805.

[31] R. de Kat and B. W. van Oudheusden. “Instantaneous planar pressure determination from PIV in turbulent flow.” en. In: *Experiments in Fluids* 52.5 (May 2012). Company: Springer Distributor: Springer Institution: Springer Label: Springer Number: 5 Publisher: Springer-Verlag, pp. 1089–1106. DOI: 10.1007/s00348-011-1237-5.

[32] R. Kumar and P.R. Viswanath. “Passive control of surface pressure fluctuations in reattaching flows.” In: *Aeronautical Journal* 106.1066 (2002), pp. 669–674.

[33] R. Kumar, P.R. Viswanath, and A. Prabhu. “Mean and fluctuating pressure in boat-tail separated flows at transonic speeds.” In: *Journal of Spacecraft and Rockets* 39.3 (2002), pp. 430–438. DOI: 10.2514/2.3826.

[34] Rajan Kumar. “Meand and Fluctuating Pressure field in boat-tail separated flows at transonic speeds.” MA thesis. Indian Institute of Science, 1999.

[35] Quanzheng Li, Gang Wang, Mengzhu Qin, and Lincheng Xu. “Numerical study of flows over launch vehicles with various fairing by second-moment closure Detached-eddy simulation.” en. In: (2024).

[36] Haixu Liu, Bing Wang, Yincheng Guo, Huiqiang Zhang, and Wenyi Lin. “Effects of Inflow Mach Number and Step Height on Supersonic Flows over a Backward-Facing Step.” EN. In: *Advances in Mechanical Engineering* 5 (Jan. 2013). Publisher: SAGE Publications, p. 147916. DOI: 10.1155/2013/147916.

[37] Yi Liu, Gang Wang, Hongyu Zhu, and Zhengyin Ye. “Numerical analysis of transonic buffet flow around a hammerhead payload fairing.” en. In: *Aerospace Science and Technology* 84 (Jan. 2019), pp. 604–619. DOI: 10.1016/j.ast.2018.11.002.

[38] Petr Louda, Jaromír Příhoda, Karel Kozel, and Petr Sváček. “Numerical simulation of flows over 2D and 3D backward-facing inclined steps.” en. In: *International Journal of Heat and Fluid Flow* 43 (Oct. 2013), pp. 268–276. DOI: 10.1016/j.ijheatfluidflow.2013.05.023.

[39] Rakhab C. Mehta. “Computational Fluid Dynamics Analysis and Design of Payload Shroud of Satellite Launch Vehicle.” en. In: *Scholars Journal of Engineering and Technology* 10.4 (Apr. 2022), pp. 16–34. DOI: 10.36347/sjet.2022.v10i04.001.

[40] Scott M. Murman, Laslo T. Diosady, and Patrick J. Blonigan. “Comparison of Transonic Buffet Simulations with Unsteady PSP Measurements for a Hammerhead Payload Fairing.” en. In: *55th AIAA Aerospace Sciences Meeting*. Grapevine, Texas: American Institute of Aeronautics and Astronautics, Jan. 2017. DOI: 10.2514/6.2017-1404.

[41] NASA. *Buffeting During Atmospheric Ascent*. Tech. rep. NASA, 1964.

[42] J. Panda, T.J. Garbeff, N.J. Burnside, and J.C. Ross. “Unsteady pressure fluctuations measured on a hammerhead space vehicle and comparison with Coe and Nute’s 1962 data.” In: *International Journal of Aeroacoustics* 17.1-2 (2018), pp. 70–87. DOI: 10.1177/1475472X17743626.

[43] J. Panda, N.H. Roozeboom, and J.C. Ross. “Wavenumber-frequency spectra on a launch vehicle model measured via unsteady pressure-sensitive paint.” In: *AIAA Journal* 57.5 (2019), pp. 1801–1817. DOI: 10.2514/1.J057449.

[44] D.J. Piatak, M.K. Sekula, and R.D. Rausch. “Ares launch vehicle transonic buffet testing and analysis techniques.” In: *Journal of Spacecraft and Rockets* 49.5 (2012), pp. 798–807. DOI: 10.2514/1.A32175.

[45] T.S. Prahlad. “A profile of aerodynamic research in VSSC with application to satellite launch vehicles.” In: *Sadhana* 12.1-2 (1988), pp. 125–182. DOI: 10.1007/BF02745662.

[46] Solana Perez R. “On the unsteady development of the flow under transonic Buffet onditions: Experimental study of the interaction of shock and pressure waves using PIV and Schlieren visualisation.” MA thesis. TU Delft, 2017.

[47] D. Ragni, F. Schrijer, B. W. van Oudheusden, and F. Scarano. “Particle tracer response across shocks measured by PIV.” en. In: *Experiments in Fluids* 50.1 (Jan. 2011). Company: Springer Distributor: Springer Institution: Springer Label: Springer Number: 1 Publisher: Springer-Verlag, pp. 53–64. DOI: 10.1007/s00348-010-0892-2.

[48] H.-G. Rho, P.A. Nguyen, J.-S. Bae, S.-H. Park, and K.-H. Byun. “Analysis of the Hammerhead Launch vehicle using CFD CAE coupled method in the transonic regime.” In: vol. 6. 2022, pp. 4285–4296.

[49] Andrea González Romero. “Experimental investigation into the aerodynamics of hammerhead launcher configuration in transonic regime.” MA thesis. TU Delft, 2023.

[50] Kshitij Sabnis and Holger Babinsky. “A review of three-dimensional shock wave–boundary-layer interactions.” In: *Progress in Aerospace Sciences*. SI: Ramjet/Scramjet Aerodynamics: A Progress Review 143 (Nov. 2023), p. 100953. DOI: 10.1016/j.paerosci.2023.100953.

[51] S. Scharnowski and C. J. Kähler. “Investigation of a transonic separating/reattaching shear layer by means of PIV.” In: *Theoretical and Applied Mechanics Letters* 5.1 (Jan. 2015), pp. 30–34. DOI: 10.1016/j.taml.2014.12.002.

[52] Sven Scharnowski, Mickael Bosyk, Ferdinand Schrijer, and Bas van Oudheusden. “Passive Flow Control for the Load Reduction of Transonic Launcher Afterbodies.” In: *AIAA Journal* (2019).

[53] Peter J. Schmid. “Data-driven and operator-based tools for the analysis of turbulent flows.” en. In: *Advanced Approaches in Turbulence*. Elsevier, 2021, pp. 243–305. DOI: 10.1016/B978-0-12-820774-1.00012-4.

[54] F. F. J. Schrijer and F. Scarano. “Effect of predictor–corrector filtering on the stability and spatial resolution of iterative PIV interrogation.” en. In: *Experiments in Fluids* 45.5 (Nov. 2008), pp. 927–941. DOI: 10.1007/s00348-008-0511-7.

[55] F. F. J. Schrijer, A. Sciacchitano, and F. Scarano. “Spatio-temporal and modal analysis of unsteady fluctuations in a high-subsonic base flow.” In: *Physics of Fluids* 26.8 (Aug. 2014), p. 086101. DOI: 10.1063/1.4891257.

[56] Andrea Sciacchitano and Morgan Li. *Lecture Slides — AE4180 Flow Measurement Techniques*. Lecture slides, available via Brightspace. TU Delft. 2024.

[57] Andrea Sciacchitano, Fulvio Scarano, and Bernhard Wieneke. “Multi-frame pyramid correlation for time-resolved PIV.” In: *Experiments in Fluids* (2012).

[58] V. Statnikov, I. Bolgar, S. Scharnowski, M. Meinke, C. J. Kähler, and W. Schröder. "Analysis of characteristic wake flow modes on a generic transonic backward-facing step configuration." In: *European Journal of Mechanics - B/Fluids* 59 (Sept. 2016), pp. 124–134. DOI: 10.1016/j.euromechflu.2016.05.008.

[59] K. Sunil, I. Johri, and P. Priyadarshi. "Aerodynamic Shape Optimization of Payload Fairing Boat Tail for Various Diameter Ratios." In: *Journal of Spacecraft and Rockets* 59.4 (2022), pp. 1135–1148. DOI: 10.2514/1.A35215.

[60] Aaron Towne, Oliver T. Schmidt, and Tim Colonius. "Spectral proper orthogonal decomposition and its relationship to dynamic mode decomposition and resolvent analysis." In: *Journal of Fluid Mechanics* 847 (2018), pp. 821–867. DOI: 10.1017/jfm.2018.283.

[61] Paul Van Gent, Qais Payanda, Steve Brust, Bas Van OUdheusden, and Ferry Schrijer. "Experimental study of the effects of exhaust plume and nozzle length on transonic and supersonic axisymmetric base flows." en. In: (2017). Artwork Size: 15 pages Medium: PDF Publisher: Proceedings of the 7th European Conference for Aeronautics and Space Sciences. Milano, Italy, 3-6 july 2017, 15 pages. DOI: 10.13009/EUCASS2017-657.

[62] N. S. Vikramaditya and M. Viji. "Dynamics and spectral character of unsteady pressure field on afterbody of generic space launcher: Transonic flows." In: *European Journal of Mechanics - B/Fluids* 107 (Sept. 2024), pp. 121–137. DOI: 10.1016/j.euromechflu.2024.06.007.

[63] Jerry Westerweel and Fulvio Scarano. "Universal outlier detection for PIV data." en. In: *Experiments in Fluids* 39.6 (Dec. 2005). Company: Springer Distributor: Springer Institution: Springer Label: Springer Number: 6 Publisher: Springer-Verlag, pp. 1096–1100. DOI: 10.1007/s00348-005-0016-6.

A

Solid Blockage Estimation

To verify the approximate increase of $\Delta M = +0.05$ reported by Romero [49] and D'Aguanno [20], the one-dimensional (1D) compressible flow relation between Mach number and area variation is used to estimate the effect of solid blockage. This analysis is based purely on geometry and neglects the influence of wind tunnel boundary layer growth. The following governing equation is employed:

$$(1 - M^2) \cdot \frac{dV}{V} = -\frac{dA}{A} \tag{A.1}$$

$$dV = a \cdot dM \tag{A.2}$$

where M is the setpoint Mach number, V is the freestream velocity, A is the test section area, and a is the speed of sound. Equation above is an approximation, assuming a negligible change in sonic velocity due to blockage. The freestream conditions are calculated using isentropic relations, as summarised in Table below. A blockage ratio of 2.75% at $\alpha = 0°$ is applied to estimate the corresponding change in Mach number.

M	ΔM
0.8	0.061
0.7	0.037
0.6	0.026

Table A.1: Blockage effect on Mach number

The resulting values of ΔM range from +0.026 to +0.061, closely aligning with the predicted increase of approximately +0.05. This confirms that the estimated blockage-induced rise in Mach number is physically reasonable.

B

Wind Tunnel Test Matrix

The experimental work was conducted in two campaigns. The first was an exploratory campaign using Schlieren imaging and surface oil-flow visualisation to map the principal flow features and guide case selection. The second campaign focused on high–spatial resolution PIV measurements at selected configurations. Owing to operational constraints in the TST-27 facility, the PIV campaign could not be completed in full; only 7 of the planned 18 runs were executed. The test matrices for both campaigns are provided on the following pages.

Measurement technique	**Block**	**SN**	**FoV**	**BT angle (°)**	**BT radius (mm)**	**AoA (°)**	**Mach**	**Comments**
Schlieren	1	1	2	34	0	0	0.8	
	2	2	1	34	0	0	0.6	
		3					0.7	
		4					0.8	
		5				4	0.6	
		6					0.7	
		7					0.8	
		8		15	0	0	0.7	
		9					0.8	
	3	10	1	34	3	0	0.7	
		11					0.8	
		12			6	0	0.7	
		13					0.8	
		14			10	0	0.6	
		15					0.7	
		16					0.8	
		17			15	0	0.7	
		18					0.8	
		19			20	0	0.6	
		20					0.7	
		21					0.8	
	4	22	3	34	3	0	0.6	
		23					0.7	
		24					0.8	
		25			6		0.6	
		26					0.7	
		27					0.8	
		28			10		0.6	
		29					0.7	
		30					0.8	
		31			20		0.6	
		32					0.7	
		33					0.8	
		34	1		3	4	0.7	
		35					0.8	
		36			6		0.8	
		37			10		0.7	
		38					0.8	
		39			15		0.8	
		40			20		0.7	
		41					0.8	
	5	42	4	34	0	0	0.8	Without tripstrips
		43			10		0.8	
Shadowgraphy	6	44	1	34	0	0	0.8	
Schlieren	7	45	1		0	0	0.8	Flipped KE
		46	3	34	0	0	0.8	first shock
		47			10		0.8	first shock
		48	1	34	0	0	0.75	
		49			10		0.75	
	8	50	4	34	10	0	0.8	Horizontal KE
		51	4	34	10	0	0.8	Vertical KE
		52			0		0.6	
		53					0.7	
		54					0.8	

Oil Flow	9	55		34	3	0	0.8	
		56			10		0.6	
		57					0.7	
		58					0.8	
		59			20		0.8	
		60			0	4	0.8	
		61			3		0.8	
		62			10		0.8	
		63			20		0.8	
		64			10	0	0.8	Without tripstrip

Measurement Technique	SN	BT radius	AoA	Mach	Runs Planned	Runs performed
PIV	1	0	0	0.7	3	3
	2			0.8	3	3
	3	10		0.7	3	1
	4			0.8	3	-
	5	20		0.7	3	-
	6			0.8	3	-

C

Schlieren results

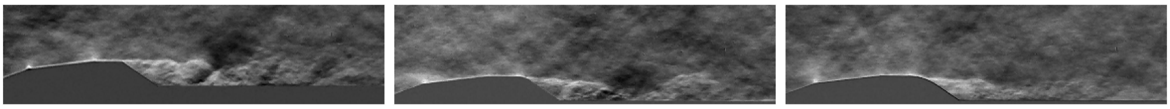

(a) R0

(b) R10

(c) R20

Figure C.1: Instantaneous schlieren images across all radii configurations at M = 0.6

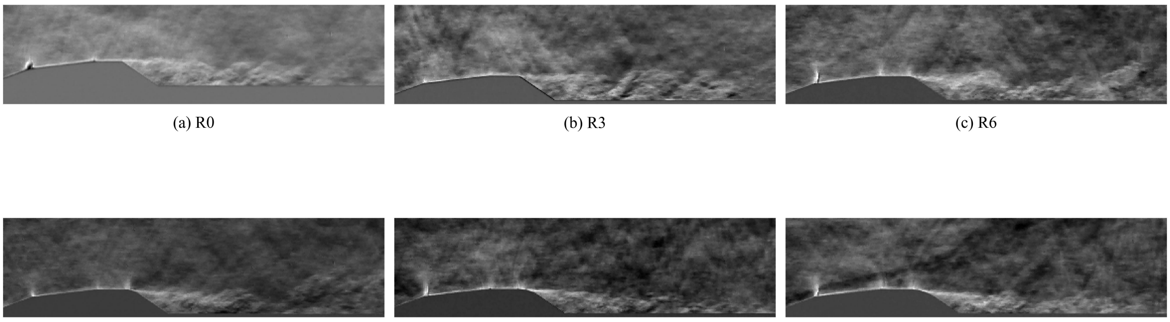

(a) R0

(b) R3

(c) R6

(d) R10

(e) R15

(f) R20

Figure C.2: Instantaneous schlieren images across all radii configurations at M = 0.7

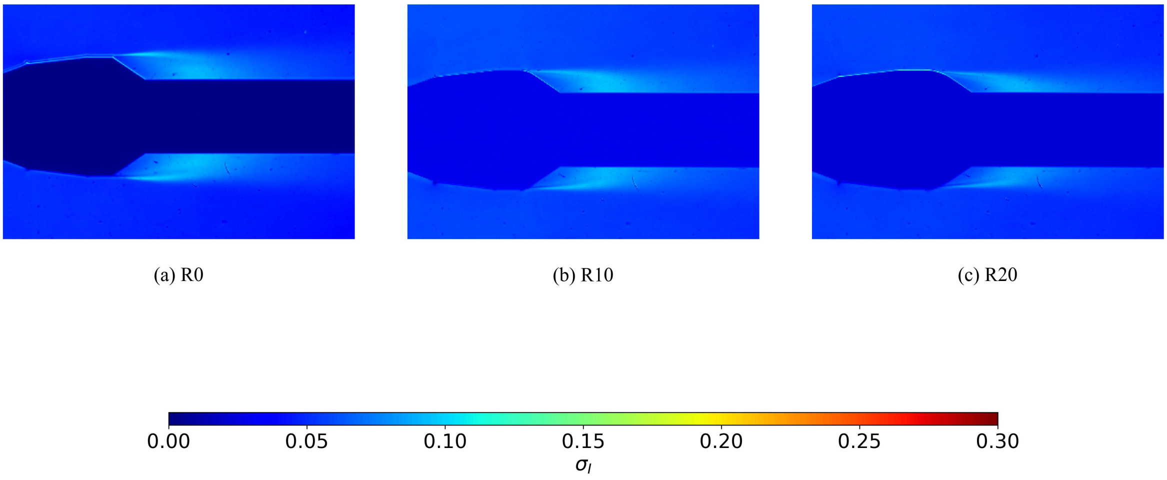

(a) R0

(b) R10

(c) R20

Figure C.3: Pixel intensity standard deviation plots of all radii configurations at M = 0.6

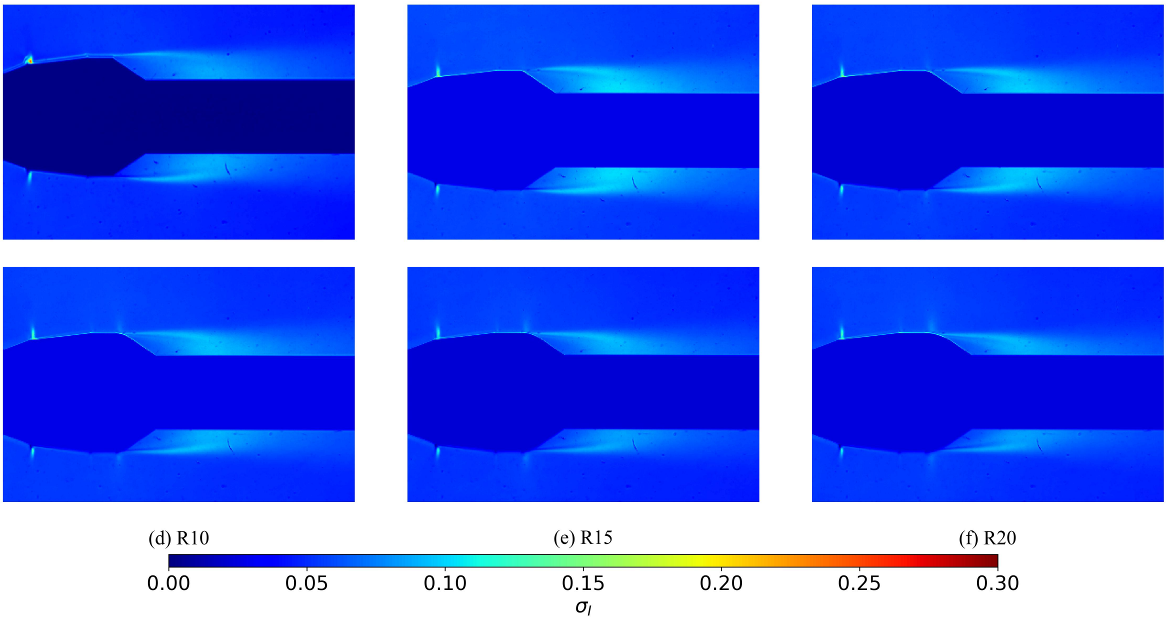

(d) R10 (e) R15 (f) R20

Figure C.4: Pixel intensity standard deviation plots of all radii configurations at M = 0.7

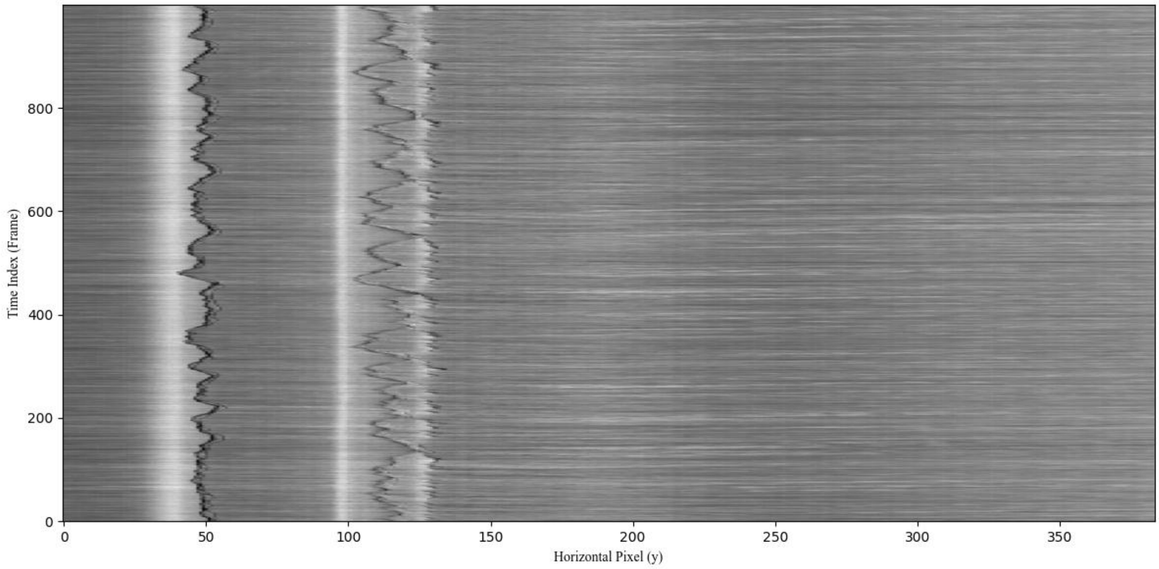

Figure C.5: Time evolution of pixel line intensity for R10 case at M = 0.8

D

Impact of Trip strip

To assess the impact of the trip strip, two schlieren runs and one oil-flow run were performed at $M = 0.8$. Figure D.1 shows instantaneous Schlieren images for the R0 and R10 cases, captured at a reduced acquisition rate of 5 kHz. The observed flow structures are consistent with those reported by Romero [49], obtained using a similar field of view, and also the present study with a zoomed-in FoV.

Figure D.2 presents the oil-flow pattern over the R0 case. The separation length extracted from this image is approximately $3.5h$ from the bottom corner, which agrees well with the results from runs with the trip strip, differing by only about 1 mm. This small discrepancy may be attributed to uncertainties in the extraction technique.

Interestingly, a noticeable accumulation of oil is observed near the forward region of the nose, at the location where the trip strip would normally be installed. The slight discontinuity at the geometric transition between the hemispherical nose and the first cone seems to promote this accumulation. This suggests that the transition itself could act as an additional tripping mechanism. Therefore, the flow behaviour observed with and without the trip strip is expected to be broadly similar.

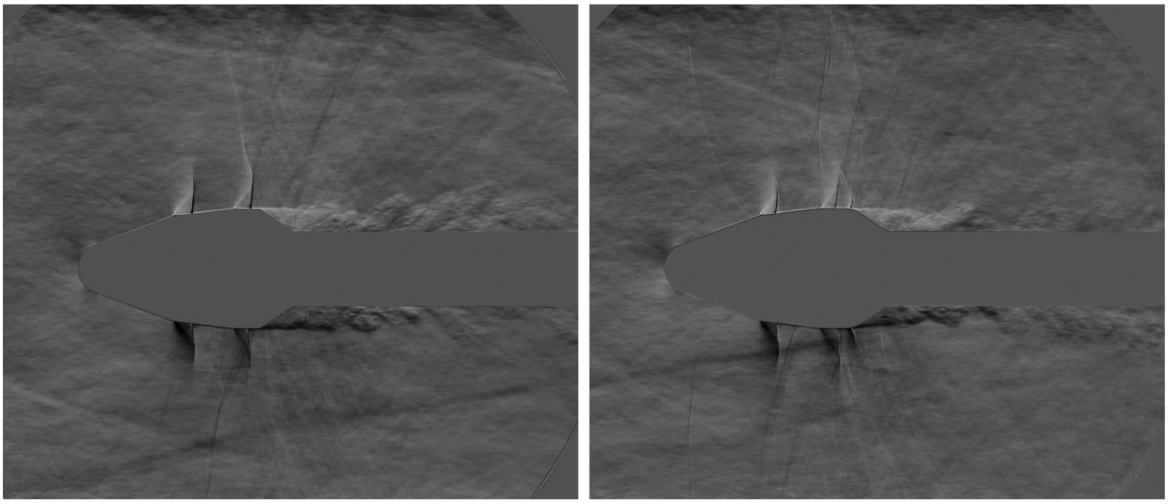

(a) R0

(b) R10

Figure D.1: Instantaneous schlieren images without tripstrip at M = 0.8

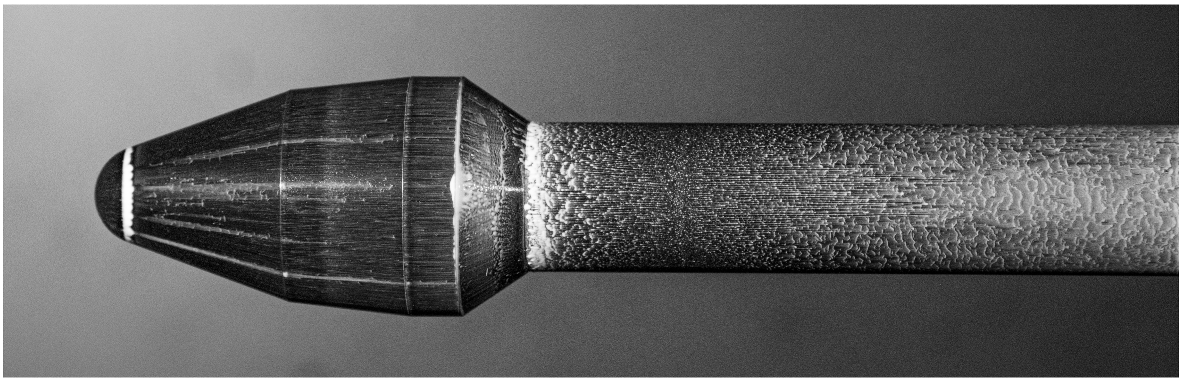

Figure D.2: Oil flow image for R0 case without tripstrip at M = 0.8

E

PIV results

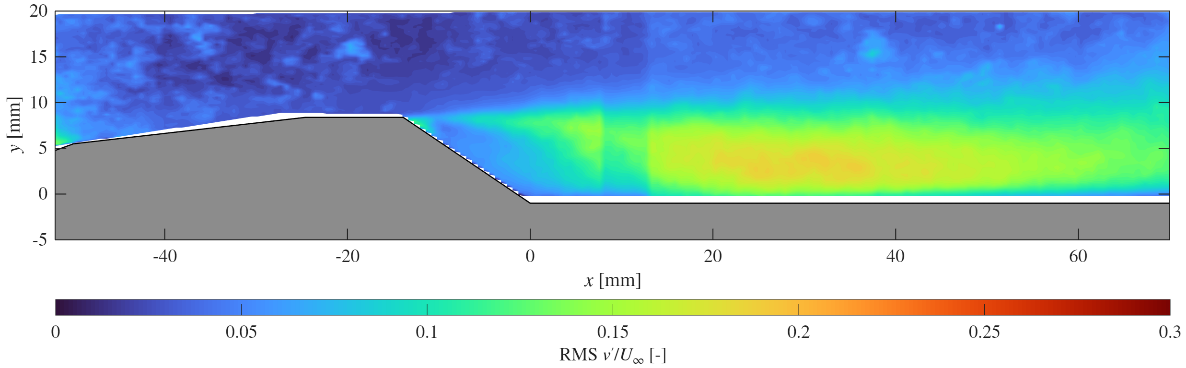

Figure E.1: Standard deviation of vertical velocity at M = 0.8 for R0 case

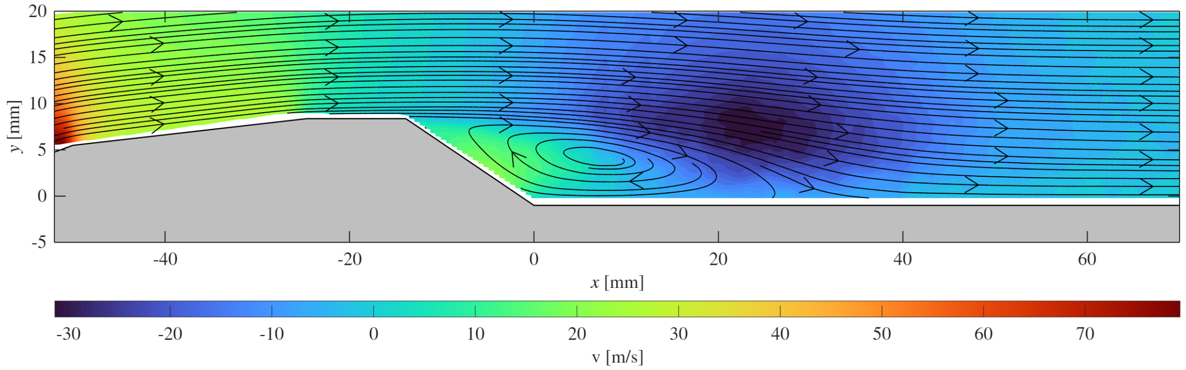

Figure E.2: PIV mean vertical velocity field at M = 0.7 with streamlines superimposed for R0 case

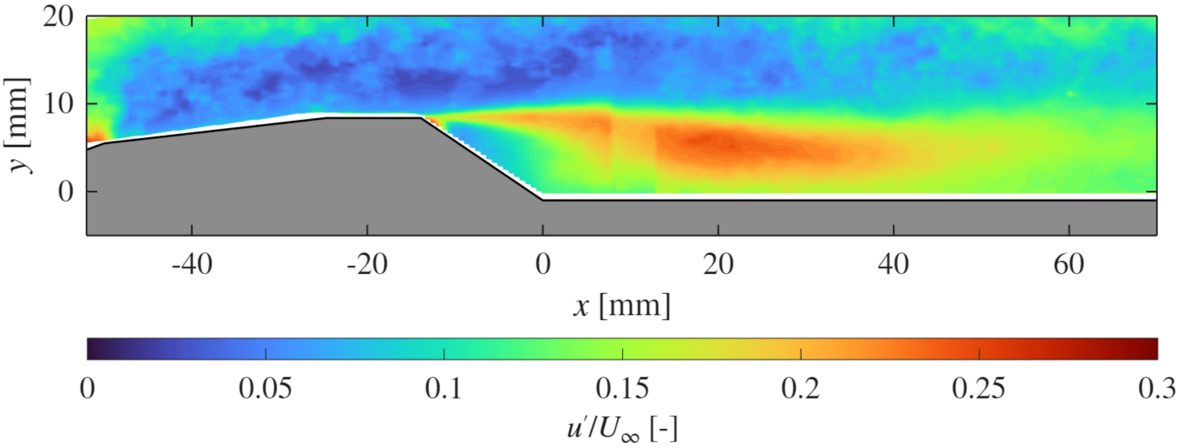

Figure E.3: Standard deviation of horizontal velocity at M = 0.7 for R0 case

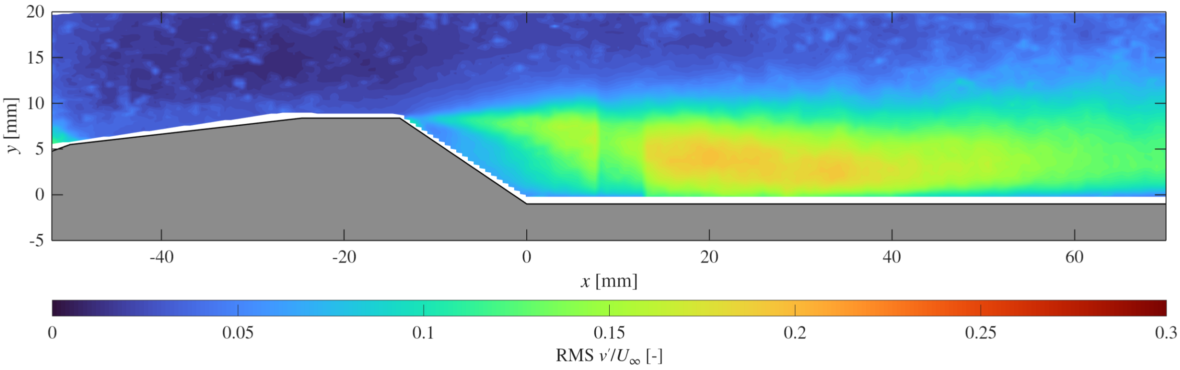

Figure E.4: Standard deviation of vertical velocity at M = 0.7 for R0 case

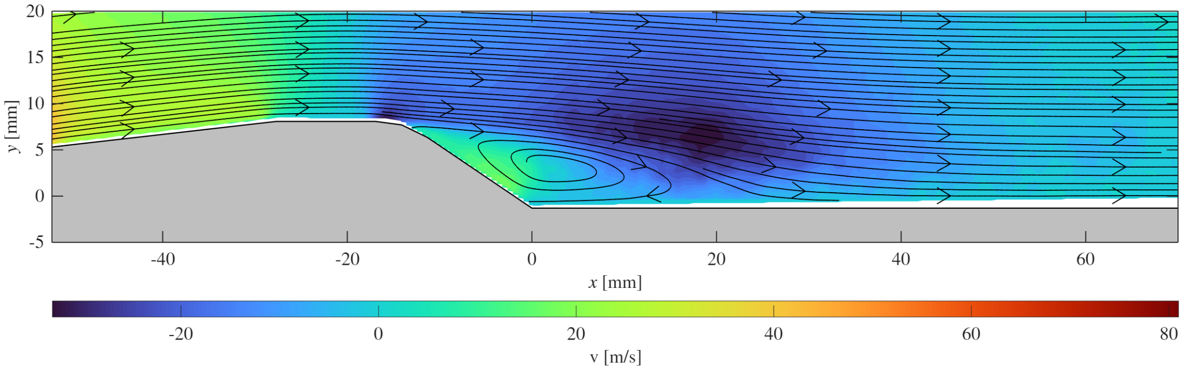

Figure E.5: PIV mean vertical velocity field at M = 0.7 with streamlines superimposed for R10 case

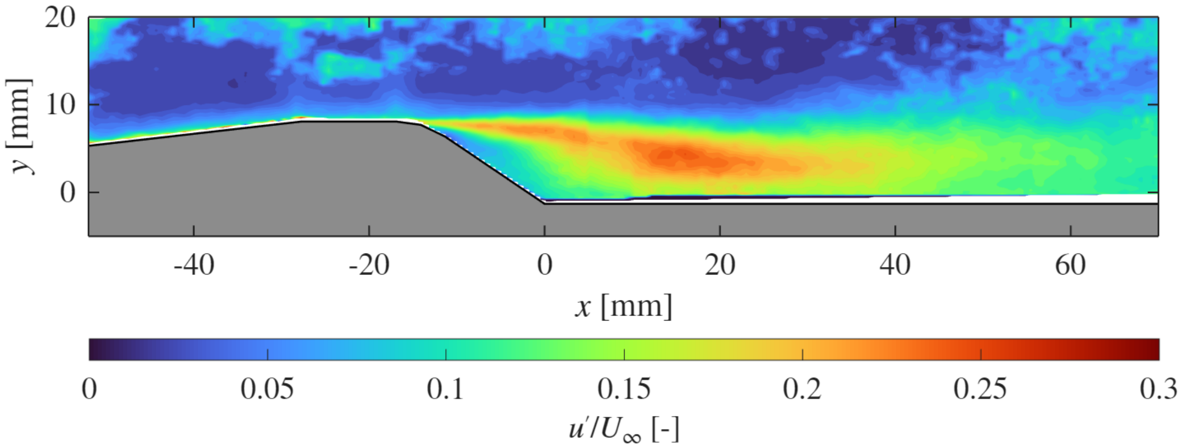

Figure E.6: Standard deviation of horizontal velocity at M = 0.7 for R10 case

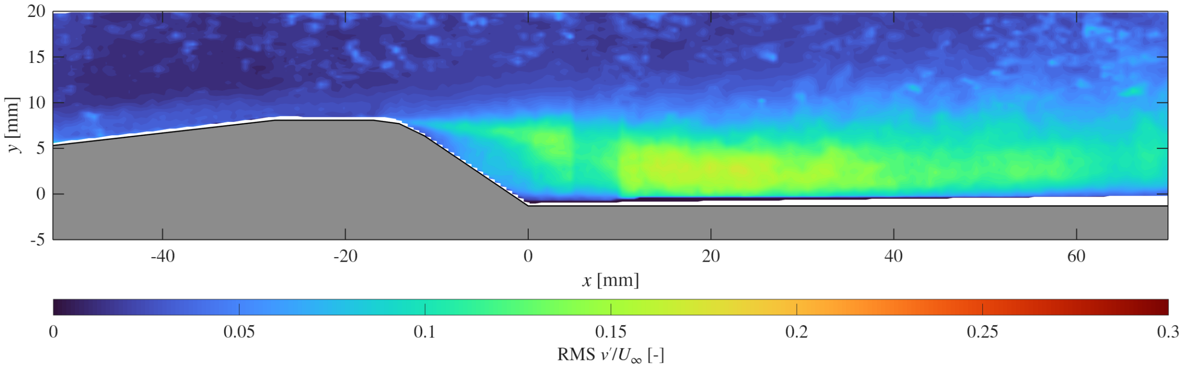

Figure E.7: Standard deviation of vertical velocity at M = 0.7 for R10 case

F

POD modes

F.1 R0 case at M = 0.8

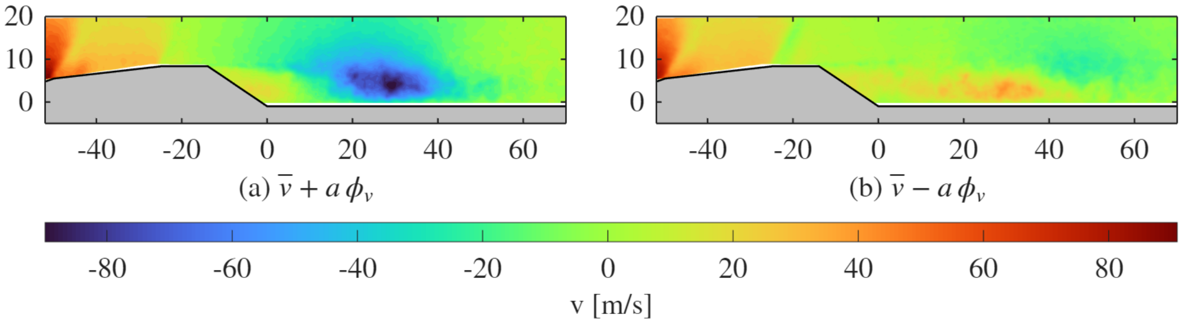

Figure F.1: v component of first POD mode superimposed on the mean flow at $M = 0.8$ for R0 case.

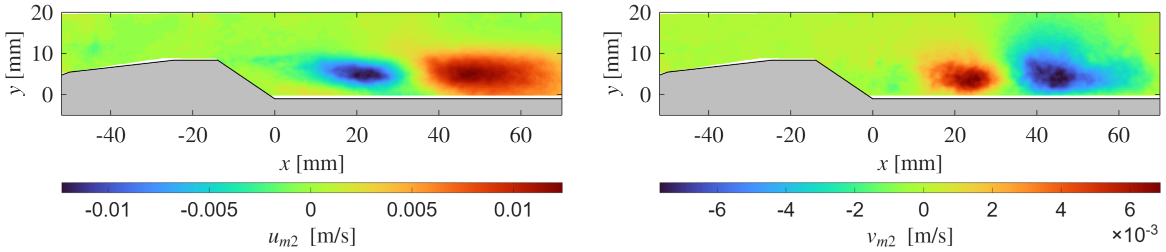

(a) u component

(b) v component

Figure F.2: Shape of the second POD mode at $M = 0.8$ for R0 case.

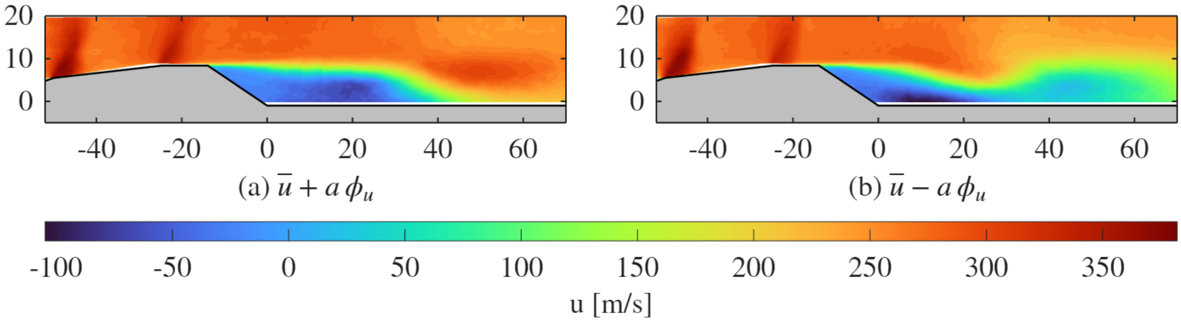

Figure F.3: u component of second POD mode superimposed on the mean flow at $M = 0.8$ for R0 case.

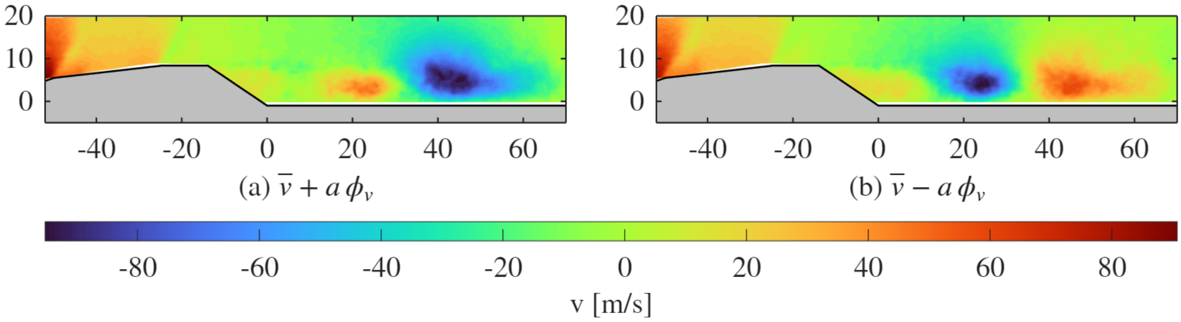

Figure F.4: v component of second POD mode superimposed on the mean flow at $M = 0.8$ for R0 case.

F.2 R10 case at M = 0.7

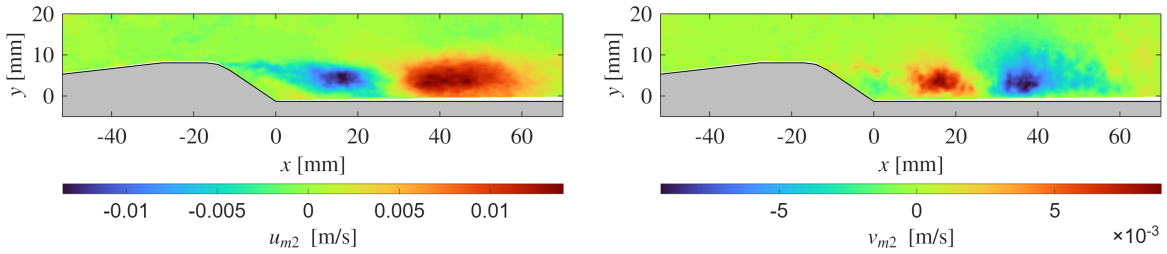

(a) u component

(b) v component

Figure F.5: Shape of the second POD mode at $M = 0.7$ for R10 case.

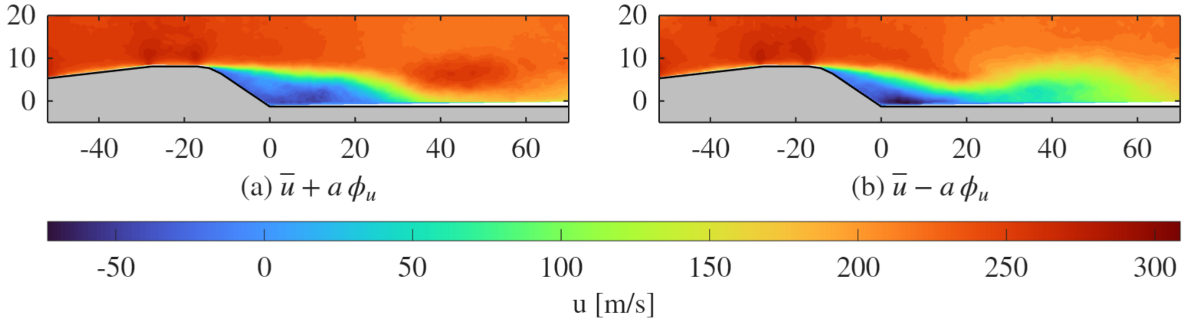
(a) $\overline{u} + a\,\phi_u$ (b) $\overline{u} - a\,\phi_u$

Figure F.6: u component of second POD mode superimposed on the mean flow at $M = 0.7$ for R10 case.

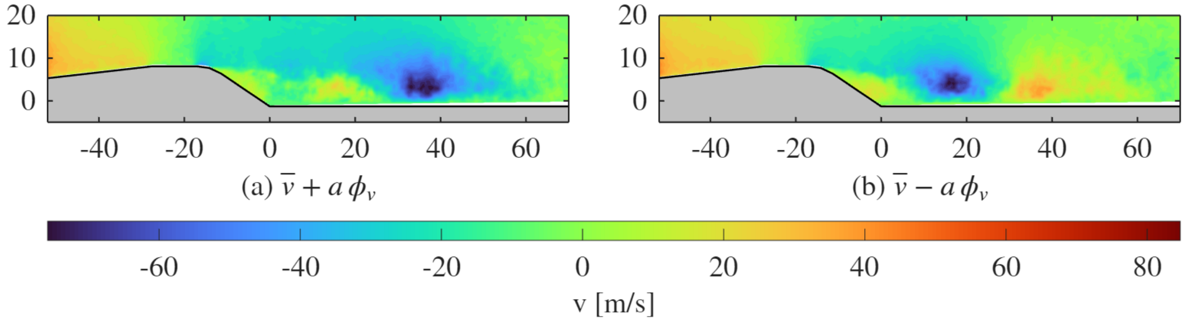
(a) $\overline{v} + a\,\phi_v$ (b) $\overline{v} - a\,\phi_v$

Figure F.7: v component of second POD mode superimposed on the mean flow at $M = 0.7$ for R10 case.

F.3 Third mode at M = 0.7 for R0 case

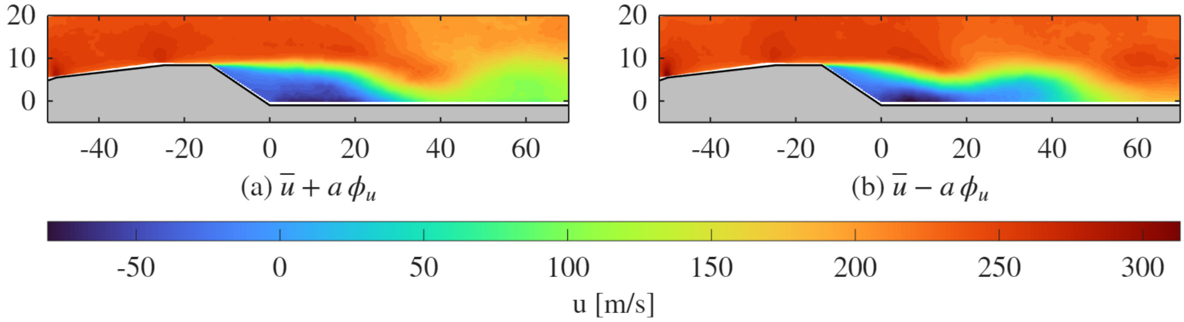
(a) $\overline{u} + a\,\phi_u$ (b) $\overline{u} - a\,\phi_u$

Figure F.8: u component of third POD mode superimposed on the mean flow at $M = 0.8$ for R0 case.

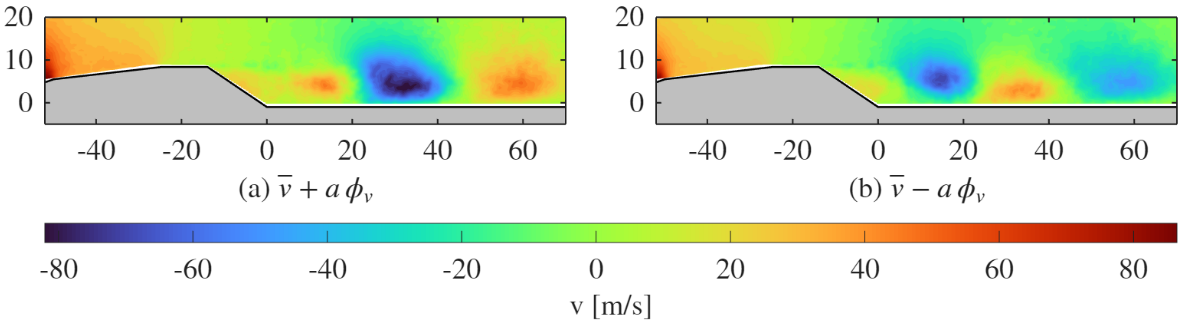

(a) $\overline{v} + a\,\phi_v$

(b) $\overline{v} - a\,\phi_v$

Figure F.9: v component of third POD mode superimposed on the mean flow at $M = 0.8$ for R0 case.

G

Strouhal number Spectra

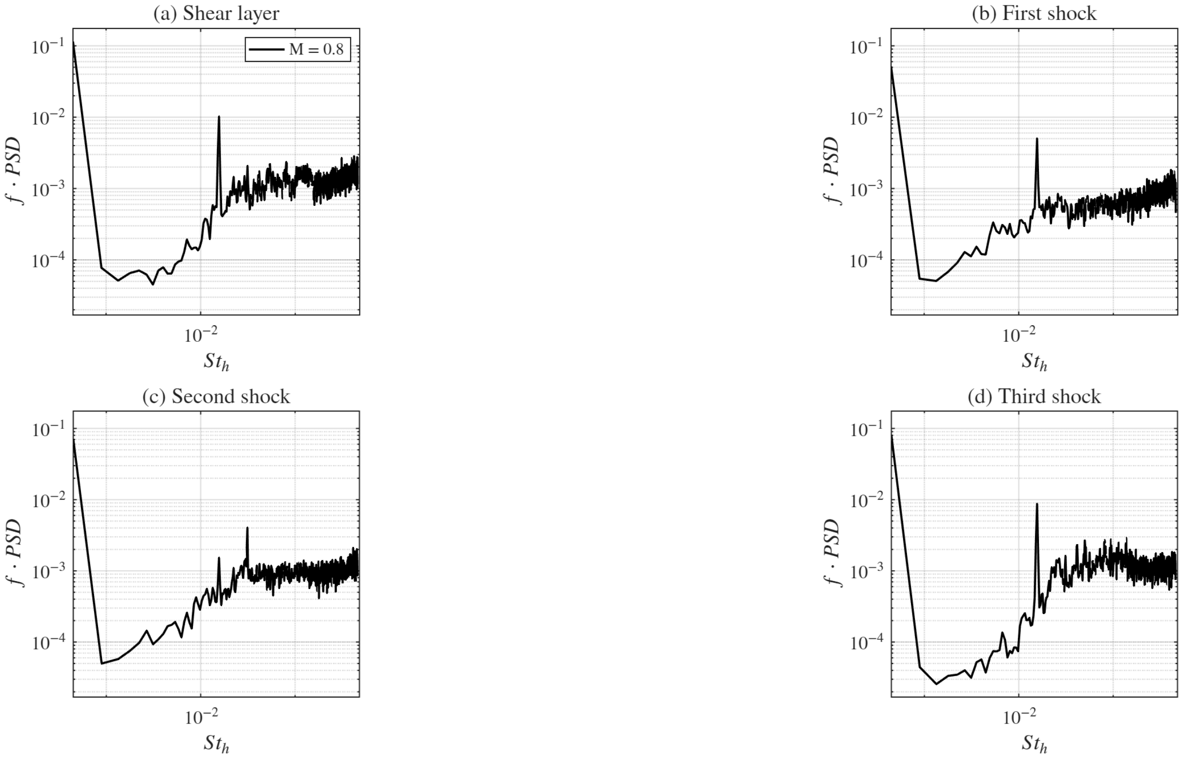

Figure G.1: FFT of pixel intensities at different locations for R10 at M = 0.8

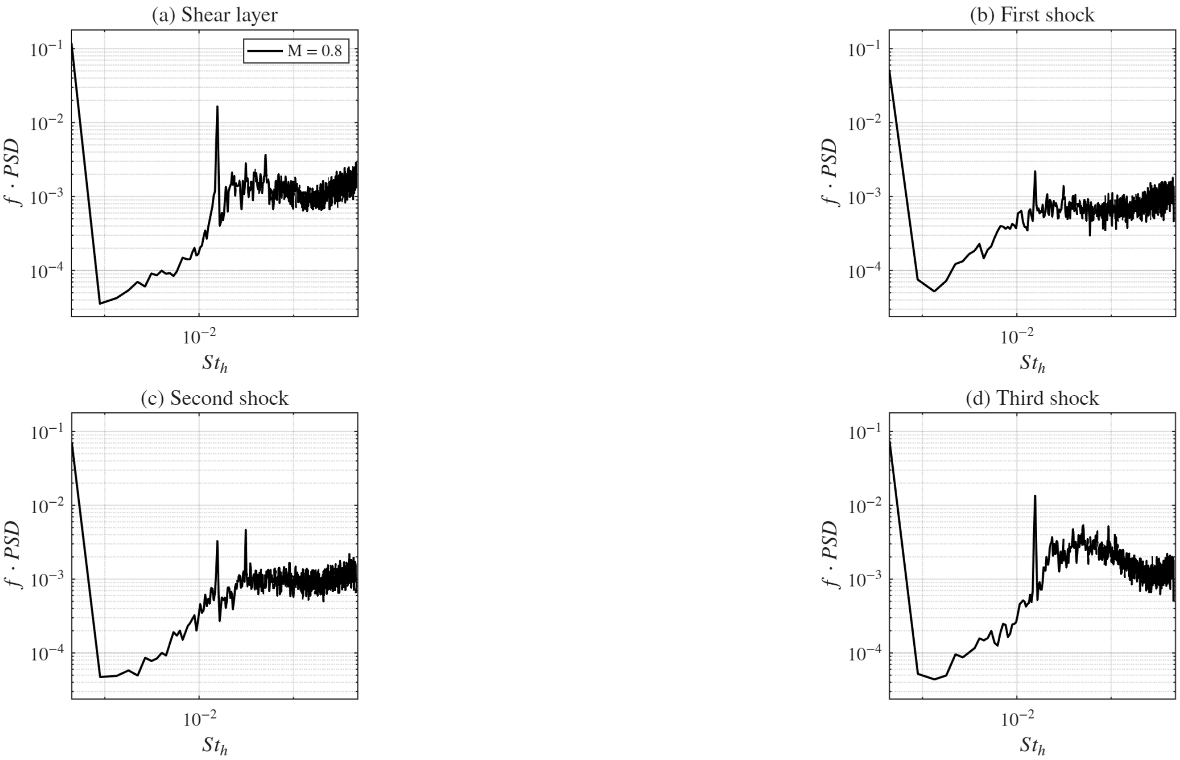

Figure G.2: FFT of pixel intensities at different locations for R20 at M = 0.8

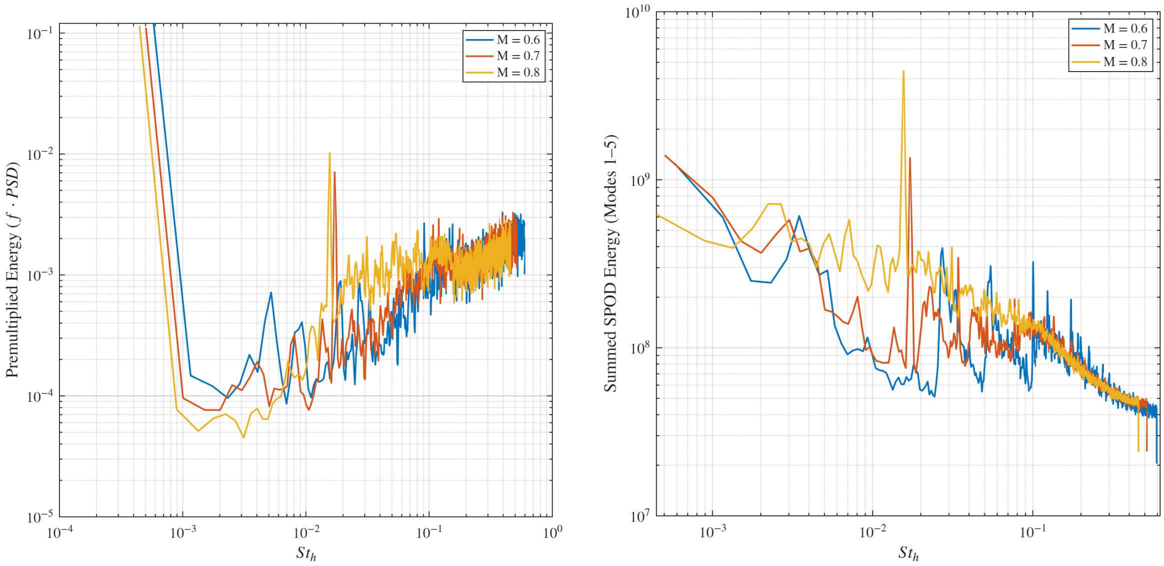

(a) FFT in the shear layer

(b) SPOD spectrum

Figure G.3: Strouhal number spectra for R10 case at different Mach numbers

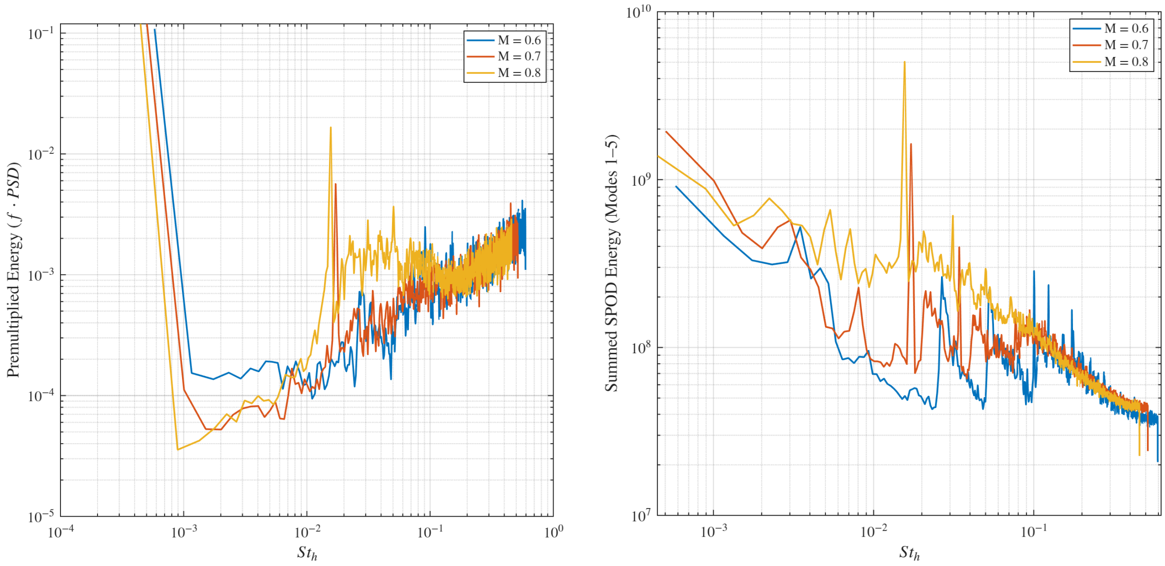

(a) FFT in the shear layer

(b) SPOD spectrum

Figure G.4: Strouhal number spectra for R20 case at different Mach numbers

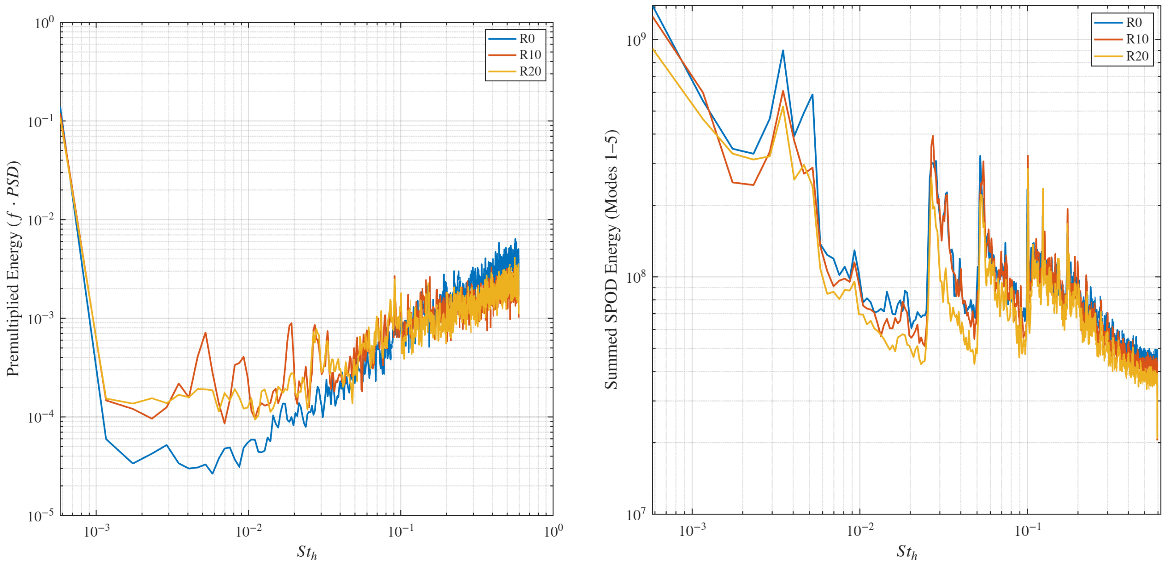

(a) FFT in the shear layer

(b) SPOD spectrum

Figure G.5: Strouhal number spectra for different cases at M = 0.6

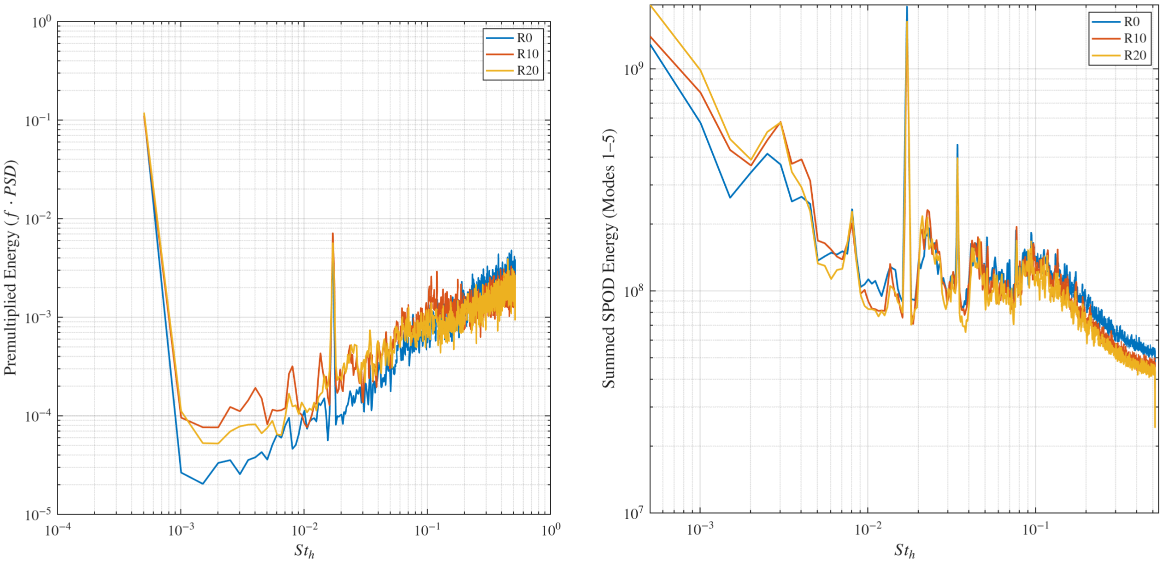

(a) FFT in the shear layer

(b) SPOD spectrum

Figure G.6: Strouhal number spectra for different cases at M = 0.7

H

SPOD results

H.1 Strouhal numbers

Table H.1: Flapping and Undulation Strouhal numbers at different Mach numbers and radii.

Mach	Radius [mm]	Flapping St_h	Undulation St_h
0.6	0	0.027	0.099
	10	0.027	0.100
	20	0.027	0.100
0.7	0	0.017	0.076
	3	0.017	0.069
	6	0.017	0.076
	10	0.017	0.077
	15	0.017	0.077
	20	0.017	0.077
0.8	0	0.0150	0.071
	3	0.0156	0.079
	6	0.0156	0.077
	10	0.0156	0.082
	15	0.0156	0.080
	20	0.0156	0.072

H.2 M = 0.6

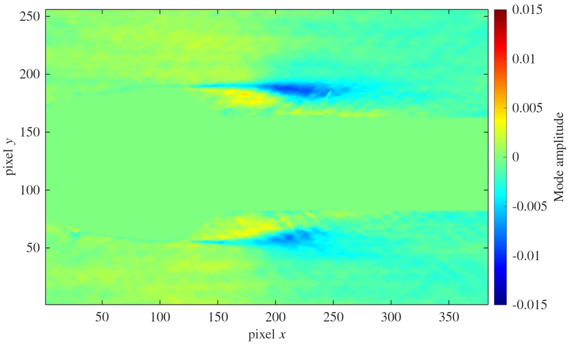

Figure H.1: SPOD mode at $St_h = 0.0331$

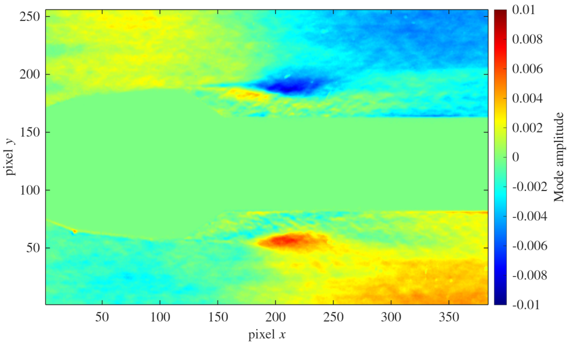

Figure H.2: SPOD mode at $St_h = 0.0545$

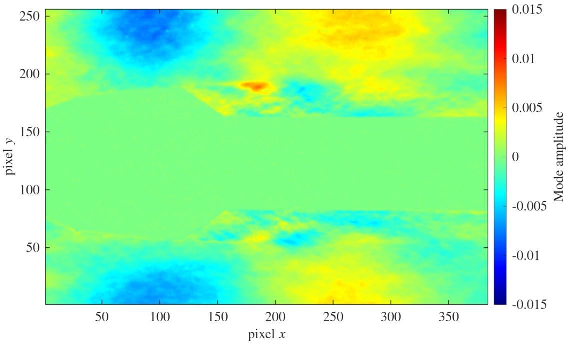

Figure H.3: SPOD mode at $St_h = 0.123$

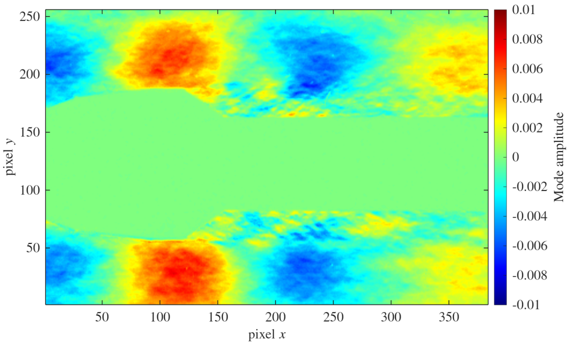

Figure H.4: SPOD mode at $St_h = 0.173$

H.3 Flapping mode

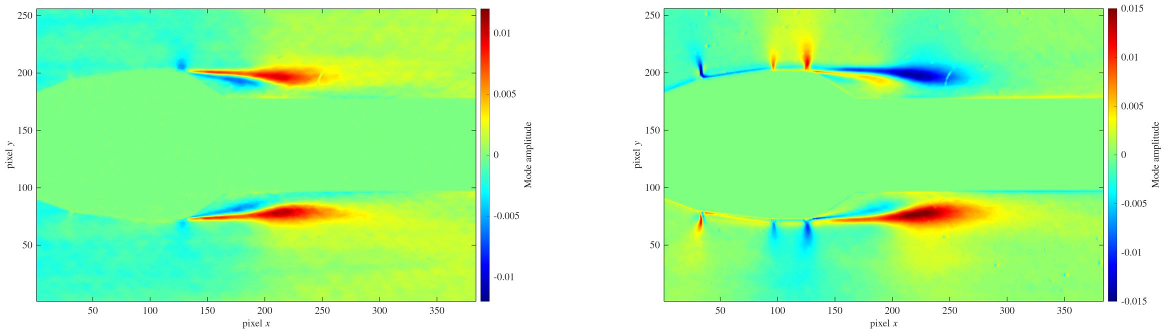

(a) M = 0.6, $St_h = 0.027$

(b) M = 0.7, $St_h = 0.017$

Figure H.5: Flapping mode at different Mach numbers for R10 case

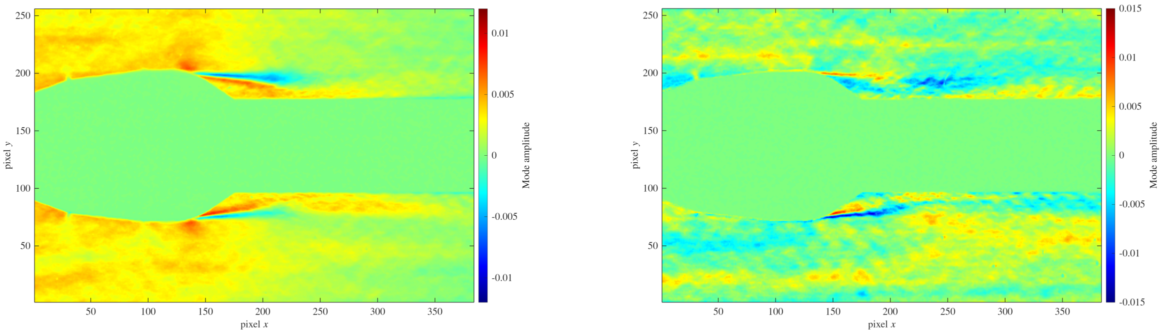

(a) M = 0.6, $St_h = 0.027$

(b) M = 0.7, $St_h = 0.0156$

Figure H.6: Flapping mode at different Mach numbers for R20 case

H.4 Undulation mode

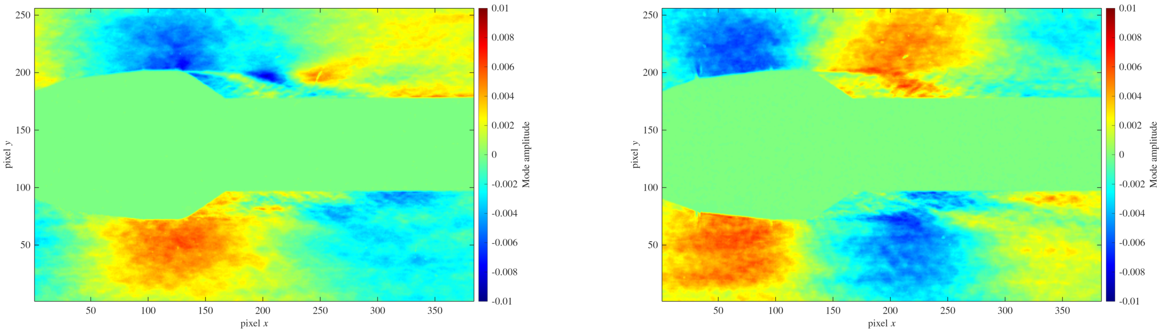

(a) M = 0.6, $St_h = 0.1$

(b) M = 0.7, $St_h = 0.077$

Figure H.7: Undulation mode at different Mach numbers for R10 case

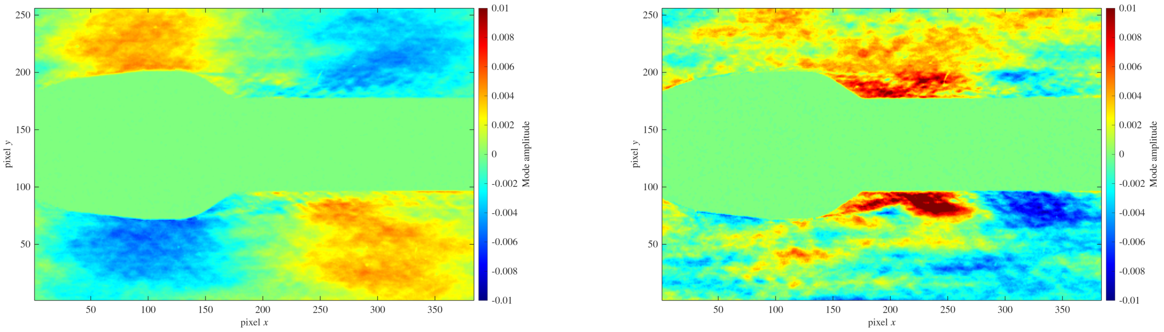

(a) M = 0.6, $St_h = 0.1$

(b) M = 0.7, $St_h = 0.077$

Figure H.8: Undulation mode at different Mach numbers for R20 case